

# FARADAY ROTATION IN MAGNETIC IONIC LIQUIDS FOR LIQUID CORE OPTICAL IN-LINE ISOLATOR APPLICATIONS

By

Devinna Fleming

---

Copyright © Devinna Fleming 2016

A Thesis Submitted to the Faculty of the

COLLEGE OF OPTICAL SCIENCES

In Partial Fulfillment of the Requirements

For the Degree of

MASTER OF SCIENCE

In the Graduate College

THE UNIVERSITY OF ARIZONA

2016

## STATEMENT BY AUTHOR

The thesis titled Faraday Rotation in Magnetic Ionic Liquids for Liquid Core Optical In-Line Isolator Applications prepared by Devinna Danielle Fleming has been submitted in partial fulfillment of requirements for a master's degree at the University of Arizona and is deposited in the University Library to be made available to borrowers under rules of the Library.

Brief quotations from this thesis are allowable without special permission, provided that an accurate acknowledgement of the source is made. Requests for permission for extended quotation from or reproduction of this manuscript in whole or in part may be granted by the head of the major department or the Dean of the Graduate College when in his or her judgment the proposed use of the material is in the interests of scholarship. In all other instances, however, permission must be obtained from the author.

SIGNED: Devinna Danielle Fleming

## APPROVAL BY THESIS DIRECTOR

This thesis has been approved on the date shown below:

\_\_\_\_\_  
*Dr. Robert A. Norwood*  
*(Professor of Optical Sciences)*

12/2/2016  
*Date*

## Acknowledgements

*Dr. Mark Bowers*

*Lockheed martin Aculight 22121 20th Ave SE Bothell, WA 98021*

*Gregory A Cohoon*

*University of Arizona College of Optical Sciences m 1630 E University Blvd, Tucson AZ 85721, USA*

*Dr. Palash Gangopadhyay*

*University of Arizona College of Optical Sciences m 1630 E University Blvd, Tucson AZ 85721, USA*

*Steve Guimond*

*Lockheed martin Aculight 22121 20th Ave SE Bothell, WA 98021*

*Dr. Robert A. Norwood*

*University of Arizona College of Optical Sciences m 1630 E University Blvd, Tucson AZ 85721, USA*

*Dr. Craig Robin*

*Lockheed martin Aculight 22121 20th Ave SE Bothell, WA 98021*

*Arjun Vinze*

*Lockheed martin Aculight 22121 20th Ave SE Bothell, WA 98021*

*\*Corresponding author:*

***Devinna Fleming***

*Optical Engineer and Laser Safety Officer*

*Lockheed Martin Laser & Sensor Systems COE*

*22121 20th Ave SE Bothell, WA 98021*

*Phone: (425) 877-2431*

[\*devinna.d.fleming@lmco.com\*](mailto:devinna.d.fleming@lmco.com)

[\*dfleming@email.arizona.edu\*](mailto:dfleming@email.arizona.edu)

## Table of Contents

A.	<b>List of Figures</b> .....	7
B.	<b>List of Tables</b> .....	9
C.	<b>List of Equations</b> .....	10
D.	<b>Abstract</b> .....	13
I.	<b>Introduction</b> .....	14
II.	<b>Literature review</b> .....	16
a.	<b>Isolators</b> .....	16
i.	Applications and necessity .....	16
ii.	Faraday rotation .....	17
iii.	Isolation .....	19
iv.	Technology available and current limitations .....	21
b.	<b>Fiber</b> .....	22
i.	Fiber background .....	22
ii.	Hollow core fiber chain .....	26
c.	<b>Ionic materials</b> .....	28
i.	Applications and necessity .....	28
ii.	Benefits of ionic liquids for Faraday rotation .....	28
iii.	Technology available and Current Limitations .....	29
d.	<b>Room for Experimentation</b> .....	30
III.	<b>Research Methodology</b> .....	32
a.	<b>Material Synthesis</b> .....	32
b.	<b>Material Verification</b> .....	33
i.	Ionic liquid .....	33
ii.	Waveguide interaction .....	35
c.	<b>Faraday rotation measurement</b> .....	36
i.	Test Set up .....	36
ii.	Polarization through the system .....	38

iii.	Test parameters .....	50
iv.	Verification and validation of test equipment .....	51
d.	<b>LCOF measurement</b> .....	52
i.	Test Set up .....	52
ii.	Test Parameters .....	53
iii.	Polarization through the system .....	54
iv.	Applied Magnetic Field .....	55
v.	Chain Structure .....	57
vi.	Filling the chains .....	59
vii.	Verification/Validation of test equipment .....	60
IV.	<b>Findings and Results</b> .....	62
a.	<b>Material Verification</b> .....	62
i.	UV-Vis Spectrum .....	62
ii.	Absorption spectrum within fiber types .....	66
b.	<b>Faraday rotation measurement</b> .....	68
i.	Creating the sample chamber .....	68
ii.	Temperature dependence .....	69
iii.	Temperature dependence - hot end .....	73
iv.	Temperature dependence - cold end .....	76
v.	Magnetic field dependence .....	76
vi.	Magnetic field dependence- results .....	81
c.	<b>LCOF measurement</b> .....	85
i.	Creating the chains .....	85
ii.	Filling the chains .....	89
iii.	Beam imaging .....	90
iv.	Magnetic field within the solenoid .....	91
v.	LCOF results .....	92
V.	<b>Discussion of future work</b> .....	99
a.	<b>Faraday rotation</b> .....	99
b.	<b>LCOF chains</b> .....	100

c.	<b>Isolation Measurement</b> .....	101
d.	<b>Other material exploration</b> .....	102
i.	NMR .....	102
ii.	FTIR .....	103
VI.	<b>Conclusion</b> .....	106
a.	<b>Significance of this work</b> .....	106
b.	<b>Main Results</b> .....	107
c.	<b>Lessons learned</b> .....	108
d.	<b>Future work and closing remarks</b> .....	110
IX.	<b>References</b> .....	112

## **A. List of Figures**

<b><u>Figure</u></b>	<b><u>Page</u></b>	<b><u>Description</u></b>
2.1	20	Isolator polarization rotation and isolation diagrams
2.2	22	Fiber isolator top level schematic
2.3	24	Single clad waveguide structure
2.4	24	Double clad waveguide structure
2.5	25	Typical structure of a fiber optic cable [Fiberguide]
2.6	26, 111	Detailed layout of the liquid core optical fiber (LCOF) structure
2.7	27	Fiber end face without stress rod blowout
2.8	27	Fiber end face with stress rod blowout
2.9	28	[BMIM][Fe <sup>3+</sup> ] Ionic structure
3.1	32	1BMIM structure (1-butyl-3-methylimidazolium)
3.2	38	Cryostation test schematic
3.3	41	Photo elastic modulator compression oscillation
3.4	43	$E_x$ and $E_y$ field interactions with 0 and $\pi/2$ phase delay
3.5	44	Net electric field amplitude as a function of phase retardation
3.6	48	Setting the $A_0$ parameter on the HINDS controller
3.7	49	Bessel function approximation
3.8	49	Nirvana detector gain factors
3.9	49	Nirvana responsivity
3.10	52	Seed, isolator, and polarization paddle LCOF setup
3.11	53, 92	Liquid core optical fiber test schematic
3.12	55	Rotating analyzer transmission geometry
3.13	56	Amperian loop around a solenoid wound with wire coils
3.14	57	Solenoid optical axis and top down views
3.15	58	Angled fiber splice
3.16	59	LCOF chain structure
3.17	59	New Era syringe pump
4.1	62	Absorption of [BMIM][FeCl <sub>4</sub> ] from 200 to 2000nm Absorption of [BMIM][FeCl <sub>4</sub> ] in the 850 to 1100nm and 1200nm to 1600nm regions
4.2	63	
4.3	64	Absorption of [BMIM][ErCl <sub>6</sub> ] from 200 to 2000nm Absorption of [BMIM][Er <sub>2</sub> Cl <sub>6</sub> ] in the 500 to 800nm and 850nm to 1100nm regions
4.4	65	
4.5	65	Absorption of [BMIM][ErCl <sub>6</sub> ] in the 1200nm to 1600nm and 1900nm to 2000nm regions
4.6	67	Supercontinuum sweep from 500 to 1700nm of SMF and hollow core fiber (LCOF) with different termination
4.7	68	Transmission of SMF and hollow core fiber over 500nm to 1700nm
4.8	69	Liquid cell comprised of 3 microscope slides epoxied together

4.9	70	Detected Faraday rotation signal for a blank fused silica cell vs. temperature
4.10	71	Corrected voltage for a blank fused silica cell vs. temperature
4.11	72	Voltage and phase of the Faraday rotation signal for a fused silica cell with [BMIM][FeCl <sub>4</sub> ] vs. temperature
4.12	73	Phase corrected Faraday rotation signal for a fused silica cell with [BMIM][FeCl <sub>4</sub> ] vs. temperature
4.13	74	Rotation for a blank fused silica cell vs. temperature
4.14	75	Rotation for a fused silica cell filled with [BMIM][FeCl <sub>4</sub> ] vs. temperature
4.15	75	Extracted faraday rotation for [BMIM][FeCl <sub>4</sub> ] vs. temperature
4.16	77	Faraday rotation signal vs. magnetic field for a blank fused silica cell
4.17	77	Phase corrected Faraday rotation signal for a blank fused silica cell vs. magnetic field
4.18	78	Phase and voltage for fused silica cell filled with [BMIM][FeCl <sub>4</sub> ] vs. magnetic field
4.19	79	Corrected voltage for fused silica cell with [BMIM][FeCl <sub>4</sub> ] vs. magnetic field
4.20	82	Faraday rotation for blank fused silica cell vs. Applied magnetic field
4.21	83	Extracted faraday rotation for fused silica cell with [BMIM][FeCl <sub>4</sub> ] vs. magnetic field
4.22	84	Extracted Faraday rotation for [BMIM][FeCl <sub>4</sub> ] vs. magnetic field
4.23	86	Sample splice view from front and back (90° relative to each other)
4.24	87	Fibers before and after splice using a 15.9W electrode arc
4.25	90	Beam images from the LCOF test set up
4.26	91	Magnetic field within the test setup solenoid
4.27	93	Chain sample 1: length 13cm, power and temperature as a function of rotation angle with 0, +/-5 amps through the solenoid
4.28	94	Chain sample 1 scan differences as a function of rotation angle
4.29	94	Chain sample 1 Fourier transform of rotation sweeps
4.30	95	Chain 1 difference in Fourier transform of rotation sweeps
4.31	96	Chain sample 2: length 13.5cm, power and temperature as a function of rotation angle with 0, 3, and 5 amps through the solenoid
4.32	96	Chain sample 2 scan differences as a function of rotation angle
4.33	97	Chain sample 2 Fourier transform of rotation sweeps
4.34	97	Chain sample 2 difference in Fourier transform of rotation sweeps
5.1	101	Fiber schematic for Fresnel reflection loss
5.2	103	Schematic for LCOF Fresnel reflection loss
5.3	104	LCOF measurement schematic change

**B. List of Tables**

<b><u>Table</u></b>	<b><u>Page</u></b>	<b><u>Description</u></b>
2.1	18	Material fused silica constants [Hecht]
2.2	23	Fused silica Sellmeier coefficients
2.3	23-24	Frequency and refractive index for fused silica
3.1	34	Iron ion ( $\text{Fe}^{3+}$ ) electronic transitions
3.2	35	Erbium ion ( $\text{Er}^{3+}$ ) electronic transitions
4.1	63	Absorption measurements of iron BMIM at key wavelengths
4.2	66	Absorption measurement of erbium BMIM at key wavelengths
4.3	88	Testable chains made during testing
4.4	89	Material index for single mode NA and fiber core size

## **C. List of Equations**

<b><u>Equation</u></b>	<b><u>Page</u></b>	<b><u>Description</u></b>
2.1	17	Verdet equation
2.2	17	Rotation from Verdet equation
2.3	17, 88	CONVERSION: Gauss/ Tesla
2.4	17	CONVERSION: Min of arc/radians/degrees
2.5	19	Length needed for 45° rotation in fused silica fiber
2.6	20	Isolator isolation in dB
2.7	20	Isolator insertion loss in dB
2.8	23	Sellmeier equation
2.9	23	Wavelength to frequency
2.10	24, 112	Snell's law
2.11	25	Critical angle from Snell's law
2.12	25	Numerical aperture
3.1	36	Step-index fiber core Helmholtz distribution
3.2	36	Step-index fiber cladding Helmholtz distribution
3.3	36	Waveguide V parameter
3.4	39	Degree of polarization
3.5	39	Polarization Jones matrix: polarizer at alpha
3.6	39	Polarization Jones matrix: polarizer at 45
3.7	40	Polarization Jones matrix: Faraday rotation at beta
3.8	40	Matrix congruence theorem 1
3.9	40	Transpose of Faraday rotation Jones matrix
3.10	40	Matrix congruence theorem 2
3.11	40	Jones matrix: mirror
3.12	41	Polarization Jones matrix: Faraday rotation, two pass through beta
3.13	42	Polarization Jones matrix: photoelastic modulator
3.14	42	Polarization Jones matrix: photoelastic modulator rotated 45° 1
3.15	42	Polarization Jones matrix: photoelastic modulator rotated 45° 2
3.16	42	Polarization Jones matrix: photoelastic modulator rotated 45° 3
3.17	42	Photoelastic modulator driving oscillation
3.18	43	Polarization Jones matrix: polarizer at -45°
3.19	44	Polarization Jones matrix: final system transformation 1
3.20	44	Polarization Jones matrix: final system transformation 2
3.21	45	Polarization Jones matrix: final system transformation 3
3.22	45	Polarization Jones matrix: final system transformation 4
3.23	45	Final system transformation: N
3.24	45	Final system transformation: M

3.25	45	Final electromagnetic field 1
3.26	45	Initial electromagnetic field
3.27	45	Final electromagnetic field 2
3.28	46	Final electromagnetic field 3
3.29	46	Detector intensity 1
3.30	46	Euler's formula
3.31	46	Detector intensity 2
3.32	46	Detector intensity 3
3.33	46	Detector intensity 4
3.34	47	Cosine approximation using Bessel functions
3.35	47	Sine approximation using Bessel functions
3.36	47	Detector intensity 5
3.37	47	Detector intensity 6
3.38	47	Intensity approximation to DC voltage
3.39	47	Intensity approximation to 2f voltage
3.40	48	Ratio of intensities 1
3.41	48	Ratio of intensities 2
3.42	48	Final Faraday rotation
3.43	50	Final Faraday rotation with system gain parameters 1
3.44	50	Final Faraday rotation with system gain parameters 2
3.45	54	Retardation from polarization paddles
3.46	56	Amperes law
3.47	56	Amperes law over closed loop integral
3.48	56	Magnetic field
3.49	57, 92	Magnetic field for test solenoid
4.1	71	Material equation for and optically active medium
4.2	80	Gyration Vector
4.3	80	Gyration Vector
4.4	80	Verdet equation for fused silica 1
4.5	80	Verdet equation for fused silica 2
4.6	81	Fused silica rotation 1
4.7	81	Fused silica rotation 2
4.8	81	Fused silica rotation at 500mT
4.9	84	LCOF length for ionic liquid
4.10	85	LCOF volume for ionic liquid
4.11	88	Single mode NA 1
4.12	89	Single mode NA 2
4.13	89	Single mode index
4.14	90	Hollow core fiber volume
4.15	92	Deviation

4.16	92	Percent deviation
5.1	104	Parallel reflection
5.2	104	Parallel transmission
5.3	104	Ratio of reflection to transmission
5.4	104	Angle conditions

## **D. Abstract**

A suspended ionic solution of 1-butyl-3-methylimidazolium iron tetrachloride [BMIM][FeCl<sub>4</sub>] provides a novel medium for achieving Faraday rotation under small magnetic fields at pump wavelengths of 980nm. As verified with spectrophotometry, transmission at telecommunication wavelengths makes the solution applicable across multiple applications. A cryostation was used to measure the sample up to a 340°K and under field at 600mT, the ionic sample shows the necessary temperature stability and enables compact formats suitable for potential industrial applications. With a rotation of linearly polarized light of 0.04° over a 490μm path length, a full 45° rotation requires only a 50.6cm path length and with only a 0.000175°/K temperature dependence. The observation of polarization effects in real time using lock-in amplifiers, and a photo-elastic modulator demonstrates the scalability, responsiveness, and stability of the ionic liquids for photonic integration. The test set up provides a convenient way to expand the research on ionic liquid Faraday rotation materials and other Faraday liquids ideally leading to a compact in-line isolator solution.

## **I. Introduction**

With a solid base founded through the telecommunications boom that built out the Internet, many fiber optic components today have made great strides in minimizing size, weight, and insertion loss. Optical isolators' current dependence on heavy, high purity magneto-optic (MO) crystals with precision machining create a need for smaller, higher-average power inline isolators particularly in the visible and near infrared spectral region. Spanning many diverse industries, there is a vast need for these devices especially those that achieve low insertion loss and the potential for polarization independence.

Ultimately, the objective of creating an all fiber-coupled or "inline" isolator would supersede the bulky free space devices currently on the market. One potentially simple and attractive approach for a small, low-loss inline isolator is to use magnetic ionic liquids in a fiber core. A viscous liquid with ideal thermal, optical, and mechanical properties within a protective fiber casing acts as the active rotation medium. The liquid material must flow into and fill the fiber during assembly, while maintaining its characteristics over a range of external environments.

This study explores the material properties of liquid ionic materials, in particular  $\text{Yb}^{3+}$  and  $\text{Er}^{3+}$ , and the optical properties needed to achieve optical isolation. Ionic materials, when carefully chosen are ideal because the customizability of the ionic materials base provides key optical transparency and Faraday rotation windows at selected visible/infrared wavelengths.

Polarized light is passed through a short material path length to verify rotation, and a long material path length achieved within a hollow-core fiber demonstrates the material performance over length, magnetic field, and temperature. The Faraday rotation set-up measures the ionic liquid rotation temperature and magnetic field dependence over a  $450\mu\text{m}$  path length. The liquid core optical fiber (LCOF) measurement then expands the light material interaction to 5-30cm in order to achieve enough rotation to create isolation.

Multiple ionic liquids were successfully synthesized by the MO research team. The optical properties of a few select samples were tested for operating wavelength

optimization. Through Faraday rotation testing, the Faraday rotation of the ionic liquid was found to be  $0.28^\circ$  at a field of 600mT, equating to a final LCOF length of 7.232cm for a  $45^\circ$  and requiring 8nL of liquid in a hollow core fiber with a diameter of  $5\mu\text{m}$ . This material was also tested over temperature showing a rotation variation of  $0.35^\circ$  over  $40^\circ\text{K}$  resulting in a change of  $0.00875^\circ/\text{K}$ . Unfortunately, low temperature testing was not possible during the time frame available for this work, but can easily be pursued in the future. A glass blown sample cell is needed to ensure full isolation of the sample from the cryostation environment.

The splicing the LCOF chains together was difficult and would benefit from precision machined tools for streamlining the process and increasing the yield of splices to chains. Finally, when filling the chains with the liquid a better system is needed for visual verification of filling. There is a great potential for an inline isolator. The Faraday rotation was verified but the limited reproducibility of the fiber chains made full insertion and isolation testing impossible to complete.

With fiber standardization providing a robust platform, a fiber optic cable creates a package implementable in various environments while only imparting a small loss when spliced during integration. With low absorption at multiple operating wavelengths,  $45^\circ$  rotation from a small magnetic field, and easy integration, ionic liquids have clear promise for future isolator applications in both high-power lasers and nanophononics, along with providing options for Farady materials at wavelengths not currently available.

## **II. Literature Review**

### **a. Isolators**

#### **i. Applications and necessity**

Optical systems abound in everyday life, and though many distinct fields exist, one platform commercialized in the early 70's was an efficient, compact, robust waveguide system known today as fiber optics. Telecommunications, an industry that saw tremendous growth through fiber optics, has been optimizing components for years. By driving down losses within fiber to theoretical limits and then reducing manufacturing costs, transmitting signals with fiber has become mainstream. Voice, video, and data transmission to nearly anywhere in the globe is now possible with vast under ocean networks of fiber optic cables.

As with most optical systems, the goal is to transfer signals cleanly, yet efficiently, from point A to point B. However, noise, loss, reflections, and unwanted nonlinear effects can affect this transmission. Energy propagating in the wrong direction can affect sensitive components, disturb measurements, or even interfere with a laser amplification stage. There are many causes of these backward propagating signals particularly within a fiber architecture such as the following: a bare fiber connector, dirty fiber end-face, poorly performed splice, or reflections off subsequent optics.

Isolators solve this problem allowing light to pass unimpeded in a single direction, while blocking propagation in the opposing direction, behaving like an optical diode and protecting upstream sensitive components needed to generate and shape the signal. A small subset of these components include diodes, circulators, modulators, filters, and wavelength division multiplexers (WDM) among other power limited or polarization sensitive devices. Each fiber optical application whether it be telecommunications, light amplification, high power lasers, or optical sensor networks, faces its own sources of spikes and reflections but they all rely on one key technology, isolators, to minimize the impact.

## ii. Faraday rotation

Isolation relies on both polarization manipulation, and a key property that all materials possess: Faraday rotation. This special process of nonreciprocal light flow is a unique effect that rotates the polarization of the electromagnetic field in the same direction regardless of the light's direction of travel. This process occurs when applying a static magnetic field to a material with an appreciable Verdet constant, or  $V_B$ , with the field applied along the direction of light propagation. This quantity, with units of *radians/(gauss \* cm)*, or more commonly ( $^{\circ}/T*m$ ), quantifies how much the plane of vibration will rotate over length with a given applied magnetic field as shown in (2.1). This relates the Verdet constant to the amount of rotation achieved,  $\theta$  over the change in magnetic field strength B as a function of length L.

$$V_B = \frac{\theta}{L * B} \quad (2.1)$$

This equation, rearranged in (2.2), yields the degree to which the polarization rotates in units of radians.

$$\theta = V_B BL \quad (2.2)$$

The magnetic-optic medium, or active material in the isolator, is a bulk crystalline lattice structure supporting an active element with suitable Faraday rotation properties. Marketed Faraday materials today are typically high purity TGG (terbium gallium garnet) with Verdet constants as high as  $5000 \text{ rad } / (T * m)$  at 500nm and as low as  $500 \text{ rad } / (T * m)$  at 1.1um [Villora]. Noting two key conversions (2.3) and (2.4) allows variations in the Faraday rotation units.

$$10,000 \text{ Gauss} = 1 \text{ Telsa} \quad (2.3)$$

$$1 \text{ min of arc} = \frac{\pi}{10800} \text{ radians} = \frac{1}{60} \text{ degree} \quad (2.4)$$

Shown below in table 2.1, common Verdet constants of materials, including fused silica, at 578nm and 1atm create a reference for Faraday rotation amongst differing media.

Material	Wavelength	Temperature	Verdet Constant $V$		Index
			$\frac{\text{min of arc}}{\text{gauss} * \text{cm}}$	$\left(\frac{\circ}{T * m}\right)$	
1atm/ 760mmHg	(nm)	(°C)			(n)
Air	578	0	$V = 0.00000627$	$V = .1045$	1.000293
Water	578	20	$V = 0.0131$	$V = 218.33$	1.33
Salt (NaCl)	578	16	$V = 0.0359$	$V = 598.33$	1.544
Light Flint Glass	578	18	$V = 0.0317$	$V = 528.33$	1.6-1.62
Fused Silica	578	20	$V = 0.0166$	$V = 27.667$	1.458

TABLE 2.1 Material fused silica constants [Hecht]

A positive Verdet constant indicates the field rotates counterclockwise when traveling parallel to the applied magnetic field and clockwise when traveling anti-parallel [Hecht]. The rotation applied to the electric field is independent of the traveling wave, or wave vector  $k$ , demonstrating the same rotation direction will apply regardless of the propagation direction. Isolators rely on this very special unidirectional property coupled with polarizing elements to route light in both optical isolators and optical circulators.

A benefit of all fiber isolator would be to provide sufficient rotation (typically  $45^\circ$ ) over a short propagation distance with low optical insertion loss and only a small magnetic field needed. From Table 2.1 fused silica glass has a Faraday constant of  $V = 0.0166$  ( $\text{arcmin} * \text{gauss}^{-1} * \text{cm}^{-1}$ ) providing the needed rotation of  $45^\circ$ , or 2700 min of arc, with a 500mT field in a length of 32.53 cm, or a 600mT field with a 27.108cm length.

$$L = \frac{\theta}{BV} = \frac{2700 \text{ arcmin}}{(0.6 T) \left(1 * 10^4 \frac{\text{gauss}}{T}\right) * 0.0166 \frac{\text{arcmin}}{\text{gauss} * \text{cm}}} = 27.108 \text{ cm} \quad (2.5)$$

This length requires an equal static field but has the potential for improvement by optimizing the material as any increase in the Verdet constant over that of fused silica Verdet constant assists in driving down the total system fiber length from (2.2).

### iii. Isolation

Isolators utilize the Farady property to provide isolation to the proceeding elements. Isolation defines the total percent of transmitted backward power from any polarization state. In classic micro-optic isolators, the first optical isolation element is collimating optics, coupling and collimating the input signal generated from the source into the active Verdet medium. For polarization maintaining isolators the incident polarization axis, selected by a linear polarizer, optimizes isolation and ensures a degree of coherency. Non-PM isolators are achieved by splitting the field based on polarization and deal with each path separately. From the Faraday rotation discussion above, applying a magnetic field to the medium along the direction of light propagation, given by the wave vector  $\mathbf{k}$ , rotates the plane of vibration a controlled amount,  $\theta$ , from the electric field's initial polarization state. With a proper material length and magnetic field strength, an ideal electric field polarization rotation of  $45^\circ$  can be achieved.

A second polarizer, rotated  $45^\circ$  to the incident polarizer rejects and scatters power not aligned with the transmission axis while allowing fully rotated polarized light to pass through unobstructed. Light successfully transmitted sees similar focusing optics to couple light out of the system. Any rejected polarization typically scatters out into the package.

Isolation is a process acting on any backward propagating light travelling in the  $-\mathbf{k}$  direction. Reaching the exit polarizer first, the light adopts a linear  $45^\circ$  polarization state. Any rejected power from this polarizer turns into added rejected light in the package, which could be a substantial amount of heat in high laser power applications. Light traveling in the  $-\mathbf{k}$  direction experiences polarization rotation in the same angular

direction as the forward propagating waves. Rotated yet another  $45^\circ$ , the reflected light makes a total rotation of  $90^\circ$  from the incident light. The initial polarizer, now  $90^\circ$  off axis from the reflected light, eliminates any transmission. Figure 2.1 demonstrates how Faraday rotation resembles an optical diode only allowing light to pass unobstructed in one direction.

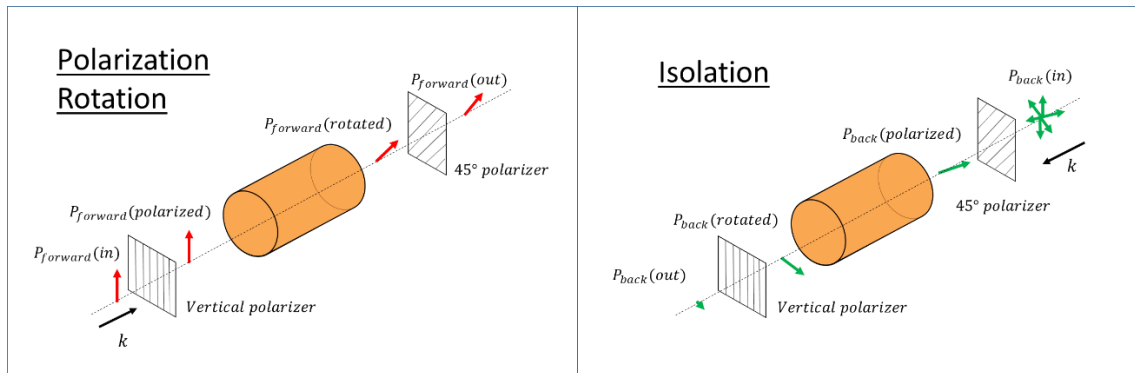


FIGURE 2.1 Isolator polarization rotation and isolation diagrams

Isolation is calculated as a logarithmic power ratio. Comparing the incident backward propagating power, and the power out, through leakage or scatter. Formula (2.6) gives isolation in dB from input and output powers. Ideally, this value exceeds 30 dB but is required to meet standards as high as 50dB for low SNR signals.

$$Isolation[dB] = 10 * \log_{10} \left( \frac{P_{back} (in)}{P_{back} (out)} \right) \quad (2.6)$$

Similarly, the devices insertion loss can be determined from these measurements. Insertion loss (IL) is another log power ratio of the forward propagating signal out, compared to the incident signal power given by (2.7).

$$Insertion Loss[dB] = 10 * \log_{10} \left( \frac{P_{forward} (out)}{P_{forward} (in)} \right) \quad (2.7)$$

A simple combination of polarization selection and an appropriate length of active material is the recipe to create an isolator capable of achieving exactly  $45^\circ$  rotation. The real benefits then come from providing isolation over a large wavelength and temperature range while maintaining low insertion loss and high isolation.

#### iv. Technology available and current limitations

All isolator applications are concerned with optimizing a few key parameters for optical systems at the operating wavelength. Isolator specifications include low insertion loss, small magnetic footprint, small package size, short optical path length, and most importantly, high isolation. Insertion loss and polarization extinction ratio (PER) issues commonly result from reflections, focusing optics, and free space polarizers. Drawbacks of paramagnetic and superparamagnetic crystals used as rotators in bulk isolators include their size, requiring enough bulk matter to support the beam, aligning the optical axis without clipping, and incorporating special cuts to preserve the crystalline structure and control the surface presented to the incident light. Furthermore, large magnets may need to be used to achieve the desired  $45^\circ$  polarization rotation, which further increases the footprint of the component. Ferromagnetic crystals would not require an external applied magnetic field, as they have their own internal field. Typically, specified for their final operating conditions, isolator manufacturers also take account that the heat imparted from power applied to the magnet and from the incident optical field on the crystal influences the quality of the isolation.

There are common tricks within the isolator industry for decreasing package size, including folding the optical path length upon its self so the rotation is accomplished over three path lengths instead of one, with a rotation per pass at  $15^\circ$ . This reduces both the crystal length and subsequently the weight along with magnet size, but requires precise alignment and is less robust.

A key isolator type for this discussion is an all-fiber isolator, which relies on using the fused silica of the fiber core, with a long path length under a large magnetic field owing to its modest Verdet constant. The main system benefit comes from low insertion loss, a direct result of eliminating the free space optics and adopting ultra-low loss splices. Even though the light never leaves from the fiber, drawbacks of staying “inline” include long fiber lengths and large magnets. For packaging these fiber can be wound upon themselves to save space but are bend radius limited for loss and to maintain polarization.

An ideal solution to shorten an inline fiber isolator consists of hollow core fiber and ionic liquid in the core as the rotating material. Utilizing a material with a higher

Verdet constant decreases package size and optical path length. A high-level picture of a the hollow core fiber and ionic liquid device is shown below in Figure 2.2.

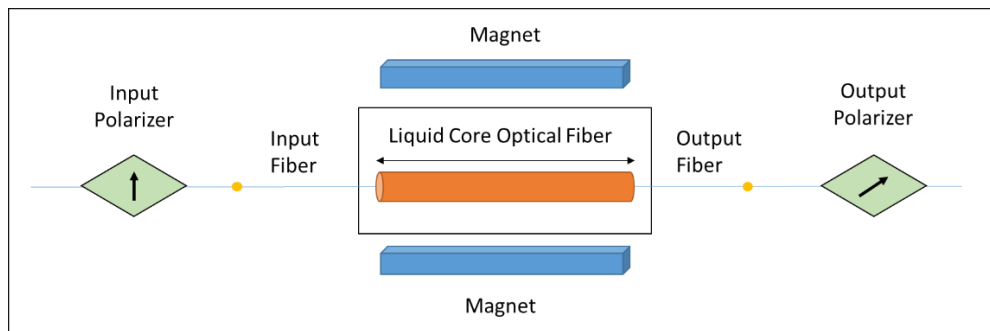


FIGURE 2.2 Fiber isolator top level schematic

The structure, primarily fiber-based, consists of two standard conventional-off-the-shelf (COTS) polarizers. These polarizers bookend a hollow core fiber housing the ionic material. A magnetic field, applied from two external magnets, activate the material contained within the all-fiber system. To make such a device a reality, critical steps include measuring the Verdet constants, getting the liquid into the fiber core, creating a rugged package, and verifying full 45 ° rotation in the final system.

## b. Fiber

### i. Fiber background

A fundamental aspect to an in- fiber isolator is the optical fiber. Fiber, standardized by a billion-dollar industry, is a robust waveguide with parameters fine-tuned through mass commercialization. A crucial aspect of isolator packaging is optimizing coupling of light into and out of the isolator, which amounts to coupling light to fiber in an all-fiber isolator.

Understanding the electromagnetic field interaction in a material starts by examining the refractive index or delay induced in the light propagation from material interactions compared to a field propagating unobstructed in a vacuum. A specific refractive index at an operating signal wavelength given by the Sellmeier equation (2.8) defines the refractive index a sum over M oscillators with oscillator strength  $B_j$  and

resonant frequency  $\omega_j$  for a given incident wavelength or frequency  $\omega$ . The resonant frequencies are oscillations in the refractive index spectrum and provide a more accurate value around the key frequencies.

$$n^2(\omega) = 1 + \sum_{j=1}^M \frac{B_j \omega_j^2}{\omega_j^2 - \omega^2} = 1 + \sum_{j=1}^M \frac{B_j \lambda^2}{\lambda^2 - \lambda_j^2} \quad (2.8)$$

The relation between frequency and wavelength is provided as a quick reference in (2.9).

$$\lambda = \frac{2\pi c}{\omega} \quad (2.9)$$

The Sellmeier parameters for pure silica are given below in lines Table 2.2 for both  $\lambda$  and  $\omega$  domain spaces.

Sellmeier Coefficients	Sellmeier Wavelengths	Sellmeier Frequencies
$B_1 = 0.6961663$	$\lambda_1 = 0.0684043 \mu m$	$\omega_1 = 2.75561 * 10^{16} Hz$
$B_2 = 0.4079426$	$\lambda_2 = 0.1162414 \mu m$	$\omega_2 = 1.62159 * 10^{16} Hz$
$B_3 = 0.8974794$	$\lambda_3 = 9.896161 \mu m$	$\omega_3 = 1.90473 * 10^{14} Hz$

TABLE 2.2 Fused silica Sellmeier coefficients

This calculated index of silica, for common telecommunications wavelengths, is given in the table below. Even though this is a good approximation typical fiber structures contain impurities, potential air bubbles, and dopants, all of which can impact the effective index of any given fiber.

Operating wavelength (nm)	$\omega$ (Hz)	$n(\omega)$
895 nm	$2.1061 * 10^{15}$	1.4518

980 nm	$1.9333 * 10^{15}$	1.4507
1064 nm	$1.7716 * 10^{15}$	1.4496
1310 nm	$1.4389 * 10^{15}$	1.4467
1550 nm	$1.2161 * 10^{15}$	1.4440

TABLE 2.3 Frequency and refractive index for fused silica

Accurate knowledge of the of refractive index and its dispersion allows for the calculation of total internal reflection (TIR) conditions, the acceptance angle  $\theta_c$ , and the more commonly used numerical aperture (NA). Using the Fresnel reflection losses and the precise the  $n_{cladding}$  index it is possible to extract  $n_{core}$  from both the transmitted and reflected power. But performing this measurement is difficult therefore a more suitable option is to submerge the sample end into an epoxy of various precise refractive indices.

A fiber optic cable is a masterfully created, precision manufactured, standardized low-loss compact component, based upon concentric cylindrical waveguides. Defining the index relation with the basic but fundamental Snell's law (2.10) controls the waveguide interface. Fiber optic cables generally consists of multiple concentric waveguides with different refractive indices using (2.10) to create preferred guiding.

$$n_{core} \sin(\theta_{core}) = n_{cladding} \sin(\theta_{cladding}) \quad (2.10)$$

A single clad fiber meets the total internal reflection (TIR) requirements when  $n_{cladding} < n_{core}$  for the central core having a higher index than the waveguide surrounding it. A double clad fiber typically adds a thin polymer film with a lower index around this outer waveguide. TIR again occurs because  $n_{outter\ cladding} < n_{cladding}$ . A single clad fiber construction is demonstrated in Figure 2.3. The addition of the thin polymer coating adds the second guiding layer creating a double clad fiber in Figure 2.4. Finally, this soft structure is encased in a hard-outer coating to protect it from breaking or losing its inner coating.

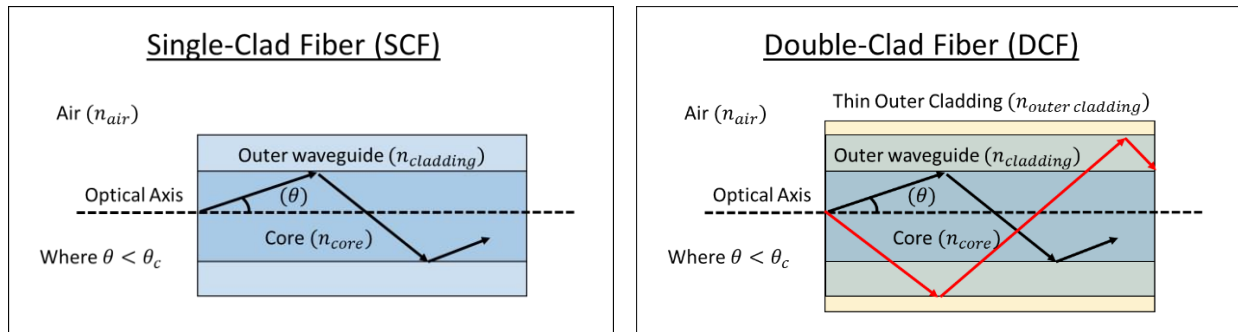


FIGURE 2.3 and 2.4 Single and double clad waveguide structure

Rearranging Snell's law for the total internal reflection condition yields the critical angle required (2.11).

$$\theta_c = \sin^{-1} \left( \frac{n_{cladding}}{n_{core}} \right) \quad (2.11)$$

The limiting acceptance cone defines a certain range of allowed angles that will successfully propagate into the core, also known as the numerical aperture, given by (2.12). Light captured within the NA achieves TIR as it propagates down the fiber. This also relates the physical wavelength that can be guided within the material from the  $V$  parameter, discussed more in section 3.

$$NA = n_{air} \sin(\theta_c) = \sqrt{n_{core}^2 - n_{cladding}^2} \quad (2.12)$$

The core, typically composed of fused silica or quartz, is just an  $SiO_2$  lattice with a refractive index of 1.4384 at 975nm. To provide a rigid outer structure the cladding has a lower refractive index than the core, typically 0.5% below the core, and is vital for total internal reflection and to ensure single-mode operation. The core refractive index for standard SMF-28 fiber is about 1.46 at 1550nm. An additional guiding layer adds structure by coating the surface with a very low index material ( $< 1.4$ ). Covering the cladding are various layers of coating protects the core from breaking and makes the resulting cable more rugged demonstrated in Figure 2.5 showing a cross section of a typical fiber.

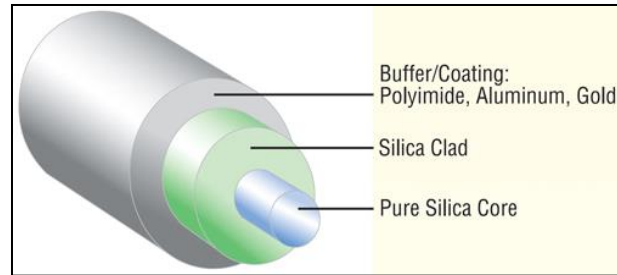


FIGURE 2.5 Typical structure of a fiber optic cable [Fiberguide]

The final consideration is signal attenuation with long transmission distances. Average attenuation per kilometer for the Corning SMF-28 single mode fiber is 0.17dB to 0.18dB while the average attenuation per splice can be as low as is 0.01dB [Corning SMF 28]. Formula (2.7) quantifies the IL for any optical component and how the splice loss is calculated.

## ii. Hollow core fiber chain

The components selected for an ionic liquid isolator start with the hollow core fiber. The key parameters include outer diameter, inner diameter, coating type, and NA set by the index of the filled material. The hollow core selected (from PolyMicro) has “applications throughout the medical and scientific industries including: gas chromatography; capillary electrophoresis, genomics, assemblies for DNA sequencing, and microfluidics.” These fibers are readily available from PolyMicro Technologies and come in multiple core sizes including 2 $\mu$ m, 5 $\mu$ m, and 10 $\mu$ m. A detailed layout of the liquid core optical fiber (LCOF) set up is shown in Figure 2.6.

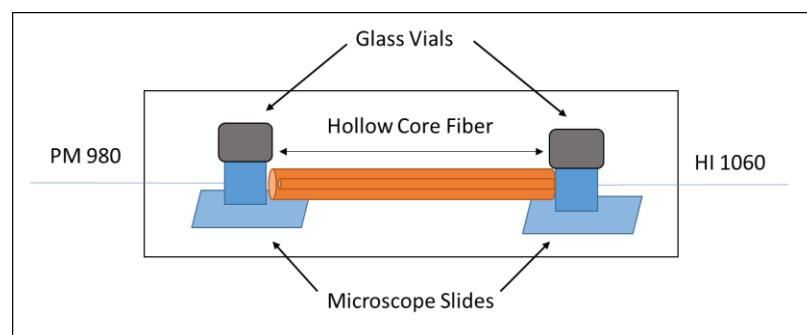


FIGURE 2.6 Detailed layout of the liquid core optical fiber (LCOF) structure

To ensure low loss and polarization maintenance of the incoming light, the input fiber chosen is a standard PM 980 from Nufern. With a core size of  $5.5 \mu\text{m}$  and mode field diameter (MFD) of  $6.6 \pm 0.5 \mu\text{m}$  at 980 nm, this fiber is readily available and inexpensive for guiding wavelengths from 970 nm to 1550 nm [Nufern]. The only factor to consider with this selection is the stress rods present within the fiber that provide birefringence needed to maintain polarization. Due to the refractive index difference of the stress rods more care needs to be placed in cleaving the fiber prior to chain construction. Because the fiber cleaving process relies on fracturing along the lattice face, a difference in crystalline structure can affect this split if not performed properly. To have the best crack propagation the blade must strike the fiber perpendicular to the stress rod axes as in Figure 2.7. If this angle is even slightly off the stress rods will fracture in a “blow out” manner, as shown in Figure 2.8. The cleave direction indicated by a red arrow. Angle cleaved to minimize back reflections; the fracture requires imparting torsion in the taught fiber prior to cleaving. Releasing the torsion during scribing creates a rotation imparting an angle on the fracture as the fiber breaks and pulls apart. Rotating the fiber  $10^\circ$  from clamp to clamp across the blade yields a  $3^\circ$ - $5^\circ$  cleave.

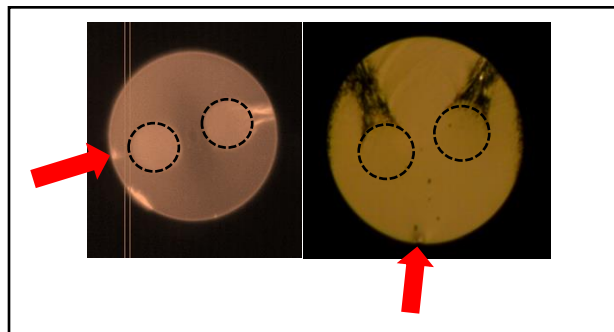


FIGURE 2.7 and 2.8 Fiber end face without and with stressrod blowouts

The angle cleaved PM 980 creates an interface with the hollow core fibers when partially spliced together that resembles a gap. Gluing this splice in a housing for liquid containment makes a chamber necessary for filling the liquid into the gap.

Using Corning's HI 1060 as the output fiber provides a  $10\mu\text{m}$  core with a MFD of  $5.9\mu\text{m} \pm 0.3\mu\text{m}$  @ 980 nm and  $6.2\mu\text{m} \pm 0.3\mu\text{m}$  @ 1060 nm, respectively, guiding any high NA light while not influencing polarization. Readily available and inexpensive HI1060's ideal operating wavelength is between 980nm and 1550nm [Corning HI1060].

### c. Ionic materials

#### i. Applications and necessity

Ionic liquids fall into a unique class of solutions, liquid at room temperature; these molten salts resemble liquefied crystalline structures. Coulombic forces from a large organic structure create a planar grid which can suspend the metal ion within the spaces in this structure. This structure resembles a crystal, but retains fluidity by not having strongly interacting ionic forces. Transparent at certain wavelengths, the molecule's structure and dominant coulombic interactions dictate transmission, absorption, emission, dipole moments, and the most crucial parameter, magnetic moment. Because the structure is very systematic, the magnetic transition levels of the ionic element dictate the rotation characteristics of the electric field's polarization. This makes properties of the ionic liquid tailorable by picking a metallic ionic element with ideal transmission at the desired wavelength to suit any application.

#### ii. Benefits of ionic liquids for Faraday rotation

Ionic liquids are ideal materials to consider for Faraday rotation because they are room temperature molten salts composed of ions with substantial molecule mobility and negligible vapor pressure. In addition to being stable over a range of environments the liquids are non-volatile, non-flammable, magnetic, and free from phase separation [Hamaguchi]. From this, a suspended ionic liquid solution of 1-butyl-3-methyl imidazolium iron tetrachloride [BMIM][FeCl<sub>4</sub>] (Figure 2.9) demonstrates ideal magnetic transitions and optical transmission for operation in the 1 $\mu$ m region [Hayashi].

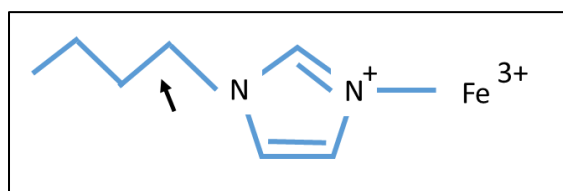


FIGURE 2.9 [BMIM][Fe<sup>3+</sup>] Ionic structure

Raman spectroscopy performed on cooled BMIM Fe:Cl structures validate the presence of trans and gauche conformations at the C7-C8 carbon bond [Hamaguchi] indicated by the black arrow in Figure 2.9.

### iii. Technology available and current limitations

There have been recent strides in the areas of ionic liquid integration into optical fiber applications. Heavy dopant elements, including  $Pb^{2+}$ ,  $Sb^{3+}$ ,  $Te^{4+}$ ,  $Bi^{3+}$  and  $Tl^{+}$ , can be readily incorporated into a glass network like the preforms of photonic crystal fibers (PCF). This integration has been demonstrated to show high Faraday rotation values without large optical attenuation [Schmidt et al]. Introduction of ionic dopants during construction by utilizing the “rod in tube” technique minimizes discontinuity pockets and bubble formation.

Alternatives explored for filling hollow waveguides included filling the microcapillaries with low melting point glass, metals, and semiconductors via pressure assisted melt filtration. Results of these studies form a good basis for exploring the filling of similar hollow waveguides with molten salts. With differing thermal expansion coefficients irrelevant for capillary diameters under  $20\mu m$ , and of limited importance at any rate given the liquid nature of the materials, the focus for the filling material can be on its optical properties, such as the refractive index or Verdet constant [Schmidt et al].

When filling the waveguides through thermal processing, one must be concerned about glass structure variations. These discontinuities can be examined with methods such as scanning electron microscopy, energy dispersive X-ray spectroscopy (cross-section), and micro Raman Scattering, which are all useful techniques to keep in mind for future exploration.

Demonstration of Faraday rotation in micro-structured waveguides established that fibers doped with terbium, silicate, chalcogenide, and tellurium exhibit strong paramagnetic properties and adequate Faraday rotation. Measured over visible and IR wavelengths the Verdet constant  $V_b$  gave rotation values at 950nm of 24, 20, 10, and 1  $rad/m^{-1}T^{-1}$  respectively and as high as 70, 35, 30, and 2  $rad/m^{-1}T^{-1}$  at 650nm [Schmidt

et al]. Photonic crystal fiber integration still faces limitations associated with fragility and high insertion loss, and high manufacturing costs from requiring “compatible combinations of viscosity, temperature dependence, crystallization stability, and thermomechanical properties” [Schmidt et al]. The research lays the framework for an all-fiber isolator but still leaves a few unanswered questions.

#### **d. Room for experimentation**

Recent strides’ validating the Faraday effect within doped PCFs opens the way for alternative ionic integration for an in-line fiber isolator. Replacing the doped preform with an ionic liquid housed within a hollow core creates an all-new fiber isolator. The ideal ionic liquid properties require a Verdet constant significantly greater than  $27.7^\circ/m^{-1}T^{-1}$  at 975nm to surpass fused silica fibers.

Focusing in on a few key ions, this experimentation starts by examining and confirming the material properties such as absorption, chemical structure, and the material interactions with the hollow optical fiber’s inner surface. Although we only explore a few liquids here, a vast variety of dopants are available and leave potential for future exploration. Many metal and transition metals exists for testing and in theory a solution is available for every wavelength.

The main measurement characterizes the amount of Faraday rotation achieved through a small path length measurement. The amount of rotation achieved can be used to extract the Verdet constant from the electromagnetic field polarization rotation. Testing this system over the magnetic field range from +/-500 mT proves the Verdet constant as a function of field. Take this can then a step further to determine how the rotation changes with temperature. Measurements are taken over the relevant temperature range for operation. A compact cryogenic chamber can test the temperature to as low as 2°K for full material characterization.

Extrapolating this constant for rotation over a longer path length is the next step in achieving the 45° rotation necessary for an isolator. The final liquid core optical fiber (LCOF) measurement attempts to vet this optical isolator approach. Once this length is

verified from the LCOF testing, then optical isolation can be measured by retro-reflecting the transmitted light back through the ionic liquid filled fiber.

### III. Research Methodology

#### a. Material synthesis

The ionic liquid starts with a base structure of 1-butyl-3-methylimidazolium iron, an iron ion supported within the aromatic heterocyclic structure of BMIM. Comprising the bulk of the BMIM material is a specific diazole called imidazole with nitrogen's in the 1 and 3 positions in addition to the carbonyl structure on the ring leads a sizeable molar mass of 139.218 g/mol. Diazole has an aromatic structure with two nitrogen's and three carbons.

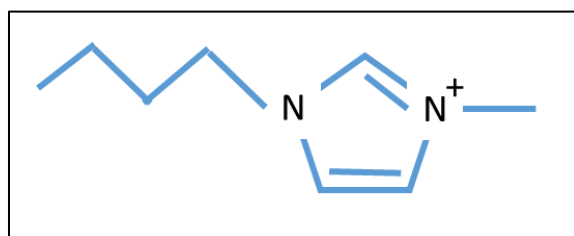


FIGURE 3.1 BMIM structure (1-butyl-3-methylimidazolium)

Creating the metal salt solution 1-butyl-3-methylimidazolium, requires careful monitoring of equi-molar concentrations of each BMIM and  $M^{3+}Cl_3 \cdot 6H_2O$  purified by filtration through an aluminum column.  $M$  is a place holder for an optical active metal or transition metal. To facilitate this reaction a heated solvent mixture of ethanol/methanol enabled the two reactants to rearrange and transfer protons.

Heating the solvent to reflux ensures sufficient activation energy for the formation of new bonds, minimizing solvent loss from evaporation, in addition to providing uniform controlled heat over the solution. Driving the reaction fully to completion required the solution to reflux for up to 12 hours. After the completed reaction, a methanol wash filtered the product from residual reactants plus heating the dry crystallized structure under reduced pressure removed any extraneous water. Verification of water removal becomes apparent when measuring wavelength dependent absorption. An advantage of this reaction is that both BMIM and the metal ion are stable.

Imidazole has 4 obvious  $\pi$  electrons from the double bonds but gains 2  $\pi$  electrons from the lone pair on the unconjugated nitrogen, while the NH lone pair resides in the  $p$

orbital and isn't included in the  $\pi$  orbital count. A final tally of 6  $\pi$  electrons satisfies Hückel's rule of  $4n+2e$  for aromaticity. In addition to being aromatic, the planar nature of BMIM increases its stability. Even the metal ion interactions with the nitrogens stabilize the planar orientation, resulting in easily formed crystals. Additionally, the stacked molecules undergo van der Waals interactions, which, coupled with imidazole's affinity for itself, give a crystal structure that forms readily, with the solvent easily evaporating.

## **b. Material verification**

### **i. Ionic liquid**

Material verification is important not only for the ionic liquids under test but also for the fiber structure that houses it. A broadband source of relatively constant amplitude across the ultraviolet, visible, and infrared regions probes the material and fiber over an applicable wavelength range. A supercontinuum source is an excellent choice, and can readily illuminate the ionic material within the fiber channel. The specific ionic material absorption can be measured through a UV-Vis test utilizing a spectrometer and a broadband source. Typically, an UV-VIS spectrophotometer scans a solution of the target material in a suitable solvent. Since here we work with a liquid that is ionic or a "neat liquid," there is no solvent within the material, it is just the ion suspended within the BMIM structure. Because of this high concentration, a short path length sample suffices as the reference. With well-calibrated path lengths, the reference scan compared to a longer path length sample enables extraction of the absorption coefficient.

A simple iron atom, element number 26, with molar mass 55.845 g/mole has electronic transitions given in Table 3.1 below. While the iron atom has an electron configuration of  $1s^2 2s^2 2p^6 3s^2 3p^6 4s^2 3d^6$ , the more electromagnetically interesting ion of iron ( $\text{Fe}^{3+}$ ) yields a configuration of  $1s^2 2s^2 2p^6 3s^2 3p^6 3d^5$  leaving its outer orbital  $d$  orbital exactly half-filled with electrons having the same spin and no shielding electrons in the  $4d$  orbital. As these valence electrons are free to move about they are subject to not only Coulomb interactions but also interactions with the rest of the material. Coupled

with intermolecular forces, the stable iron configuration has room for electron mobility centered around transition levels primarily in the visible region from 400nm to 730nm [R.H. Gargstang].

Transition	Lower $\lambda$ (nm)	Upper $\lambda$ (nm)
${}^4G - {}^2_5D$	592.0	593.0
${}^4P - {}^2_5D$	697.8	713.8
${}^4G - {}^2_3F$	508.9	527.0
${}^4P - {}^2_3F$	596.3	
${}^4D - {}^2_3F$	783.1	773.2
${}^4G - {}^4F$	490.5	495.9
${}^4D - {}^4F$	703.9	708.8
${}^4G - {}^2H$	421.7	413.5
${}^4P - {}^2S$	329.7	
${}^2_5D - {}^2_3D$	423.9	414.4
${}^2_5F - {}^2_3D$	774.2	775.7
${}^2_5F - {}^2_3G$	457.1	457.5

Table 3.1 Iron ion ( $\text{Fe}^{3+}$ ) electronic transistions [R.H. Gargstang]

When it comes to the rare earth ion  $\text{Er}^{3+}$ , element number 68, the molar mass is higher at 167.27 g/mol, and the absorbance and emittance spectra are quite distinct. With an electron configuration of  $[\text{Xe}]4f^{12} 6s^2$ , orbital electrons are further away from the nucleus, inducing longer wavelength transitions than for iron. Commonly utilized in the

telecommunications industry for amplification using its 1.55 $\mu\text{m}$  transition, erbium is a common dopant for fused silica fibers. The primary transitions for  $\text{Er}^{3+}$  given below in Table 3.2 points to wavelengths potentially ideal for transmission and high Faraday rotation.

Transition	Lower $\lambda$ (nm)	Upper $\lambda$ (nm)
${}^4I_{13/2}$	1541.8	1522.8
${}^4I_{11/2}$	987.8	986.2
${}^4I_{9/2}$	810.0	813.4
${}^4F_{9/2}$	658.6	657.8
${}^4S_{8/2}$	546.5	542.2
${}^2H_{11/2} - {}^4G_{11/2}$	526.0	523.7
${}^2G_{9/2} - {}^4F_{9/2}$	408.6	410.4
${}^2P_{3/2} - {}^2D_{3/2}$	318.3	317.5
${}^2H_{9/2} - {}^2G_{9/2}$	274.1	275.3

Table 3.2 Erbium ion ( $\text{Er}^{3+}$ ) electronic transitions [W.T. Carnall]

What's interesting about the erbium transition is the active electrons resides on the inner shell. Shielding them more from thermal variations.

## ii. Waveguide interaction

Finally, we discuss the electric field solutions for classic step-index optical fiber. The differential equations below describe a step-index fiber core and cladding, which

yield solutions given by the Bessel functions of the first kind and modified Bessel functions of the second kind, respectively [Hecht].

$$\frac{l\delta^2 u}{\delta r^2} + \frac{1}{r} \frac{\delta u}{\delta r} + \left( k_T^2 - \frac{l^2}{r^2} \right) u = 0 \quad r < a \text{ (core)} \quad (3.1)$$

$$\frac{\delta^2 u}{\delta r^2} + \frac{1}{r} \frac{\delta u}{\delta r} - \left( \gamma^2 - \frac{l^2}{r^2} \right) u = 0 \quad r < a \text{ (cladding)} \quad (3.2)$$

Bessel functions of the first kind,  $J_n(X)$ , defines the field supported within the core waveguide, where  $X = k_T a = a\sqrt{n_1^2 k_0^2 - \beta^2}$  and the propagation constant  $\beta$  is greater than  $n_2 k_0$  and less than  $n_1 k_0$ . For this relation  $n_1$  is the refractive index of the core and  $n_2$  is the refractive index of the cladding at wavelength  $\lambda$ . Similarly, a modified Bessel function of the second kind describes the evanescent tail field shape with solutions  $K_n(Y)$  with  $Y = \gamma a = a\sqrt{\beta^2 - n_2^2 k_0^2}$ , where  $\gamma$  an indicator of the fields' penetration into the cladding.

The Bessel functions are a family of solutions to a differential equation for the radial field distribution in cylindrical coordinates,  $r$ , and comprise the radial dependence of the complex amplitude of either the electric or magnetic field  $U(r, \phi, z) = u(r)e^{-jl\phi}e^{-j\beta z}$ .

This distribution defines electromagnetic field confinement in a fiber so it naturally leads to the requirement for guiding a single mode. The V parameter of the optical fiber indicates how many modes can physically be present within the optical fiber, and is defined in (3.3).

$$V = 2\pi \frac{a}{\lambda_0} NA \quad (3.3)$$

If the V parameter is less than the first zero in the  $J_0$  Bessel function, or 2.405, it means there will be only one successfully guided mode. At higher values of the V-parameter, the fiber is able to support additional higher-order modes. The Bessel function zeros take the values, 0, 2.405, 3.832, 5.520, and 7.016, continuing for increasingly larger waveguide diameters and higher order mode containment.

## c. Faraday Rotation Measurement

### i. Test Set up

Measuring the Faraday rotation properties of ionic liquids is one of the overall objectives of the project. A schematic of the experimental setup is shown in Figure 3.2. Measurements performed with the “Faraday rotation” test setup starts with a super luminescent diode (SLD) at a common 975nm wavelength, with an output power of around 100mW. Splicing the non-polarization maintaining (PM) SLD output fiber on to a flat cleaved (FC) pigtail simplifies beam-alignment through a keyed connector mounted with a fiber collimator. The correct collimator NA allows for easy transition between multiple sources. A chopper wheel modulating at 1 kHz frequency decreases the signal intensity by half, but benefits power and phase information at the detector with low shot-noise [Nirvana].

The electric field orientation, set with a rotatable polarizer, gives linearly polarized light. A subsequent 90/10 splitter propagates half the signal towards the detector as a reference with the other half continuing on the beam path. This path, when properly aligned, passes through a cryostation, a compact chamber housing the material under test with variable magnetic sources and the ability to reach cryogenic temperatures. With a closed helium and nitrogen coolant loop, the cryostation requires no filling or wasting of liquid, while stabilizing temperatures anywhere from 350°K down to 2°K. In addition to the broad thermal range, the cryostation enables testing small-scale rotation over large magnetic fields up to 700mT while precisely controlling the environment over pressures from one atm to full vacuum.

The material, exposed to various magnetic and thermal conditions, rotates the signal  $\theta^\circ$  to the reference, according to the magnetic field applied. This signal reflects off a mirror and returns back through the material under test making the total rotation  $2\theta$  from the Faraday effect. If this effect were not present, no rotation would be observed, as upon back reflection the initial rotation would be undone (i.e. reciprocal).

The rotated signal reaches the beam splitter and reflects down the measurement path through an iris, for alignment, and reaches a variable wave plate in the form of a photoelastic modulator, PEM. A final polarizer and focusing optic couples the light into a

Nirvana two-aperture detector. The Nirvana detector extracts data from the signal by removing noise from the reference beam baseline and measuring the phase and power in the material-under-test beam path.

Lock-in amplifiers set to the PEM's frequency and subsequent harmonics recorded the amplitude of the key peaks from the spectral information obtained by the detector; a pictorial representation of the full set up, Figure 3.2, gives a visual layout to work from when walking through the systems' polarization states.

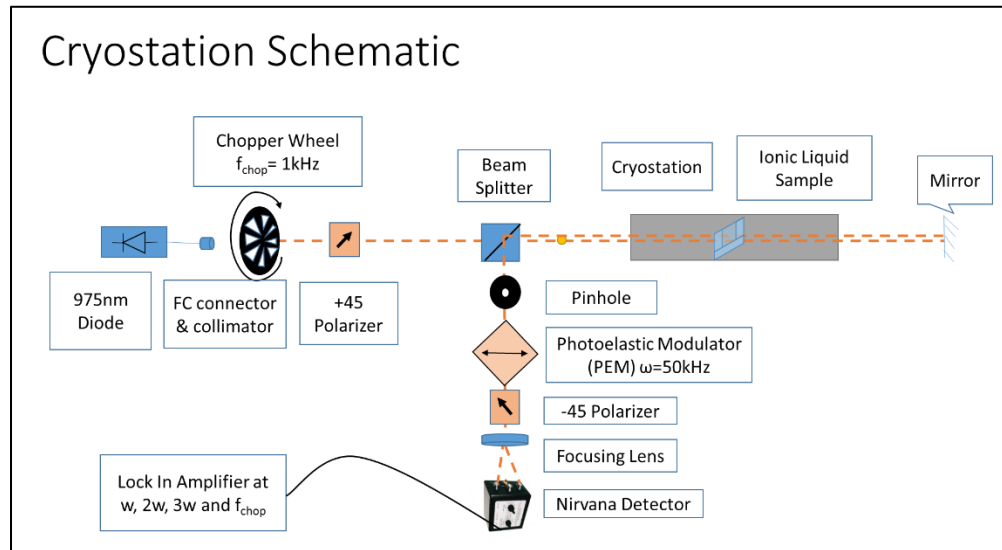


FIGURE 3.2 Cryostation test schematic

## ii. Polarization through the system

Understanding polarization within the optical setup helps reveal how the Faraday rotation influences the signal at the detector. Analyzing the contributions of all the polarizing components' interaction through Jones calculus yields a final polarization transformation matrix. Applying this final polarization matrix to an initial electromagnetic field reveals a final equation describing the final signal. The more expansive Mueller matrices ( $4 \times 4$ ) could be utilized but since the degree of polarization is set to 1 from the initial linear polarizer, and is coherent, the more compact  $2 \times 2$  Jones matrices retain all the phase and amplitude information and simplify calculations.

The DOP formula, (3.4), compares the total power  $S_0$  to the power in the Stokes polarization values including: linear horizontal/vertical  $S_1$ , linear  $+135^\circ/45^\circ$   $S_2$  and

circular,  $S_3$ . Because the signal is 100% linear, the power in  $S_2$  equates to  $S_0$  making (3.4) reduce to one verifying the Jones matrices can be used for the polarization derivation.

$$DOP = \frac{\sqrt{S_1^2 + S_2^2 + S_3^2}}{S_0} \quad (3.4)$$

The following derivation picks a coordinate system where propagation is along  $\mathbf{z}$  and the polarization is in the  $\mathbf{x-y}$  plane, where the polarizers are rotated  $+45^\circ$  and  $-45^\circ$  with respect to the  $\mathbf{z}$  axis. Because this is most representative of the physical system, the derivation will follow these axes but the matrix multiplication simplifies if the coordinate system is rotated  $45^\circ$  to match the polarizers although will yield the same result.

With the chopper modulating the power at a base frequency of 1 kHz, the first optical element the incident beam reaches is a polarizer initially rotated to  $+45^\circ$  a linear polarization state. A polarizer set to an arbitrary angle  $\alpha$  has a Jones matrix in the form given by (3.5). Represented in complex form, (3.6) represents an electromagnetic field set by a linear polarizer to  $45^\circ$ . Indicated by the superscript  $P$  this transformation matrix applies to the polarization state of the incident field. All the matrices called out below were derived from William A. Shurcliff's *Polarized Light: Production and Use* [Shurcliff].

$$M_p^P(\alpha) = \begin{bmatrix} \cos^2(\alpha) & \cos(\alpha)\sin(\alpha) \\ \cos(\alpha)\sin(\alpha) & \sin^2(\alpha) \end{bmatrix} \quad (3.5)$$

Simplifying the equation above for  $\alpha = 45^\circ$  leads to the normalized Jones matrix below. An interesting fact to note is the determinate of this matrix is zero.

$$M_p^P M_p^P(45^\circ) = \frac{1}{2} \begin{bmatrix} 1 & 1 \\ 1 & 1 \end{bmatrix} \quad (3.6)$$

The following beam splitter allows a fraction of the beam to continue to the material under test while directing the other towards the detector for an invariant reference beam, but the beam splitter imparts no polarization transformation on the system.

The experimental beam passing through the splitter next interacts with the cryostation. Seeing the chamber window first, which imparts no polarization change, the key interaction from this system comes from the Faraday material under test. Applying a magnetic field to this material under test induces a rotation of the electromagnetic field. (3.7) gives the rotation matrix  $M_{FR}^P(\beta)$  that rotates the fields polarization by an angle  $\beta$  around the  $\mathbf{z}$ -axis.

$$M_{FR}^P(\beta) = \begin{bmatrix} \cos(\beta) & \sin(\beta) \\ -\sin(\beta) & \cos(\beta) \end{bmatrix} \quad (3.7)$$

One useful application of the matrix formulation is that rotation of  $E_x$  and  $E_y$  with respect to the optical axis by an angle  $\theta$  is synonymous to a change of basis. From the matrix congruence theorem: a congruent space exists for the Hermitian field using an invertible matrix. A generic version of matrix congruence for mapping a field A to a new field B rotated by  $\beta$  is shown below in (3.8) [Gram].

$$B = M^T(\beta) * A * M(\beta) \quad (3.8)$$

Using the Jones matrix for Faraday rotation or  $M_{FR}^P$  from (3.7), the transpose of the matrix is just the negative of the rotation shown in (3.9).

$$(M_{FR}^P)^T(\beta) = M_{FR}^P(-\beta) \quad (3.9)$$

The final transformation equation for rotation takes the form (3.10).

$$B = M_{FR}^P(-\beta) * A * M_{FR}^P(\beta) \quad (3.10)$$

The opposing side of the cryostation contains additional windows and outputs the beam to a mirror. With the no phase transformation, the mirror represented by  $m$  flips the  $\mathbf{y}$  direction of the field but also changes the  $\mathbf{z}$  direction of travel but is not included in the polarization summation.

$$m = \begin{bmatrix} r_x & 0 \\ 0 & r_y \end{bmatrix} \quad (3.11)$$

Returning through the cryostation these two effects the field sees a  $2\beta$  rotation when it passes through the Faraday material for the second time. The second phase rotation result transforms the final Faraday matrix to (3.12).

$$M_{2FR}^P(\beta) = \begin{bmatrix} \cos(2\beta) & \sin(2\beta) \\ -\sin(2\beta) & \cos(2\beta) \end{bmatrix} \quad (3.12)$$

After the cryostation, the beam splitter directs the rotated signal down the measurement path. This path relies heavily on the PEM, a special acoustic crystal that undergoes index variations in a single axis from mechanical compression. This compression, oscillated at an optimized frequency  $\omega_0$ , imparts a phase delay along one component of the electric field from 0 to  $2\pi$  radians or from  $-\pi$  to  $\pi$  for a given signal wavelength, pictorially demonstrated below in Figure 3.3.

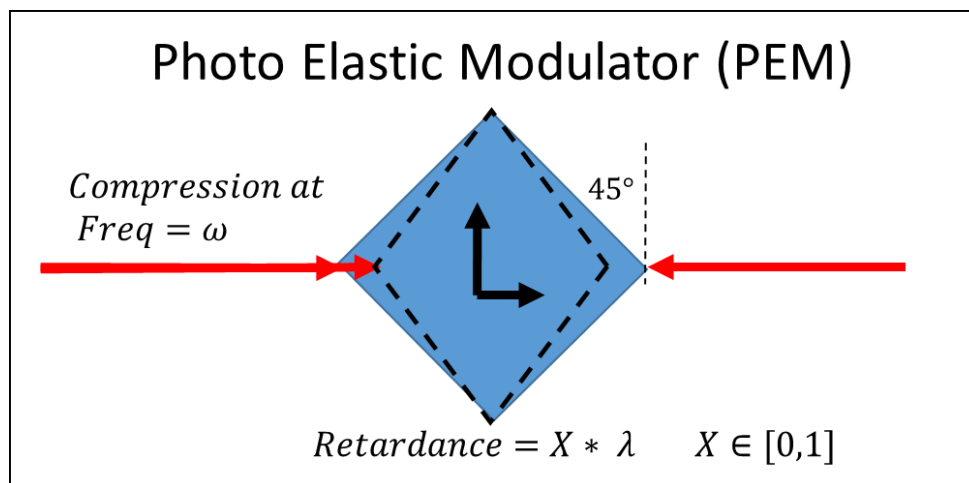


FIGURE 3.3 Photoelastic modulator compression oscillation

With incident linearly polarized light, containing proportional fields in both  $\mathbf{x}$  and  $\mathbf{y}$  directions, and an initial phase delay between  $\mathbf{x}$  and  $\mathbf{y}$  of 0 or  $2\pi$ , equal proportions of  $E_x$  and  $E_y$  interact to create the net electric field vector  $\vec{E}$  oscillating at  $45^\circ$  to the axis. As the two powers oscillate in time  $\vec{E}$  also oscillates along the  $45^\circ$  axis, as expected for linearly polarized light. Altering the phase of one axis, while maintaining the phase of the orthogonal state, results in  $\vec{E}$  no longer oscillating linearly but with some ellipticity. The Jones matrix representation of a phase retarder plate imparting a phase change of  $A$  is

shown in (3.13) This is the offset imparted by the phase difference between  $E_x$  and  $E_y$  [optical retarder].

$$M_{PEM}^P(A) = \begin{bmatrix} 1 & 0 \\ 0 & \exp\left(-i * \frac{A}{2}\right) \end{bmatrix} \quad (3.13)$$

Also, considering the frame of reference, the PEM matrix needs to be rotated using matrix congruence. Using (3.14) the PEM matrix is rotated 45 degrees to compensate for the frame of reference resulting in the rotated matrix below.

$$M_{PEM-Rotated}^P(A) = M_{FR}^P(-45) * M_{PEM}^P(A) * M_{FR}^P(45) \quad (3.14)$$

$$M_{PEM-Rotated}^P(A) = \begin{bmatrix} \cos(-45) & \sin(-45) \\ -\sin(-45) & \cos(-45) \end{bmatrix} * \begin{bmatrix} 1 & 0 \\ 0 & \exp\left(-i * \frac{A}{2}\right) \end{bmatrix} \quad (3.15)$$

$$* \begin{bmatrix} \cos(45) & \sin(45) \\ -\sin(45) & \cos(45) \end{bmatrix}$$

$$M_{PEM-Rotated}^P(A) = \begin{bmatrix} \left(\frac{\exp -i \frac{A}{2}}{2} + \frac{1}{2}\right) \left(\frac{1}{2} - \frac{\exp -i \frac{A}{2}}{2}\right) \\ \left(\frac{1}{2} - \frac{\exp -i \frac{A}{2}}{2}\right) \left(\frac{\exp -i \frac{A}{2}}{2} + \frac{1}{2}\right) \end{bmatrix} \quad (3.16)$$

Driven by a sinusoidal compression, the PEM gives a phase shift that oscillates in time at the driving frequency  $\omega_1$ , causing a net phase shift  $\Delta\Phi$  in time at 50 kHz. The frequency is given below as  $\omega_n$  where  $n$  indicates the  $n$ th harmonic of the signal.

$$A = A_0 \cos(\omega_n t) \quad (3.17)$$

Understanding how the PEM oscillations effect polarization as a function of time comes from observing the phase change along one axis through a full  $2\pi$ -phase shift, starting with horizontally polarized light. The first diagram in Figure 3.4 represents the interaction of  $E_x$  and  $E_y$  when separated by 0 phase delay. The net vector oscillates

linearly in time at  $45^\circ$  to the optical axis. Adding a  $\pi/2$  delay in the second diagram results in the final E vector rotating evenly around the axis creating right circularly polarized light (RCP).

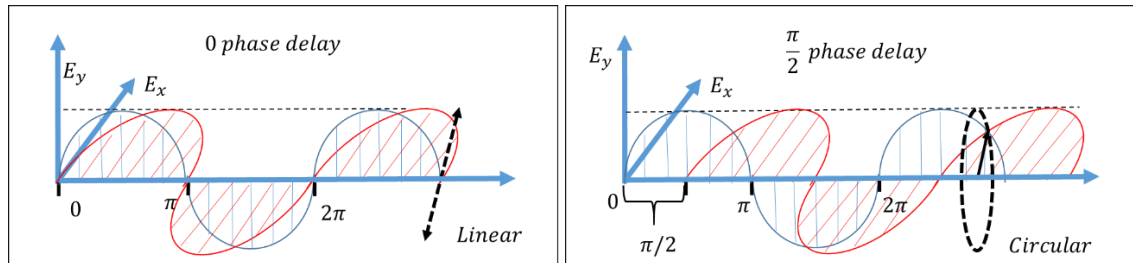


FIGURE 3.4  $E_x$  and  $E_y$  field interactions with 0 and  $\pi/2$  phase delay

Extrapolating this pattern over the full period shows how the PEM acts as a variable wave plate sweeping through all the polarization states, twice.

$$H \rightarrow RCP \rightarrow V \rightarrow RCP \rightarrow H \rightarrow LCP \rightarrow V \rightarrow LCP \rightarrow H$$

Immediately following the PEM is a linear polarizer oriented at  $\alpha = -45^\circ$ . This filter takes the polarization data imparted from the PEM and turns it into a measurable quantity. Projecting the beam under test on the final polarizer oriented at  $-45^\circ$  is represented by (3.18) below.

$$M_P^P(-45^\circ) = \frac{1}{2} \begin{bmatrix} 1 & -1 \\ -1 & 1 \end{bmatrix} \quad (3.18)$$

With no imparted phase shift, the linearly polarized light passes through the PEM and polarizer unobstructed giving an amplitude of 1. As the phase delay between the two states reaches  $\pi/2$ , the light becomes circularly polarized resulting in an amplitude less than 1 but greater than 0. A  $\pi$  delay gives linearly polarized light in the original orientation but with a flipped phase resulting in an amplitude of 0 at the detector. The amplitude returns to its original orientation at  $2\pi$  with a full intensity of 1. Passing through the entire  $2\pi$  phase shift occurs at frequency  $\omega$ , represented by the blue line cosine function in Figure 3.5.

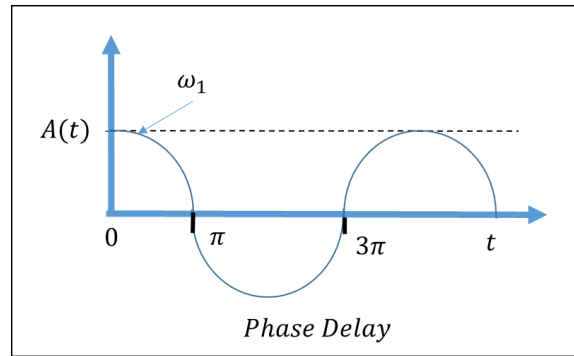


FIGURE 3.5 Net electric field amplitude as a function of phase retardation

Now understating all the transforms in the system, linear algebra allows for proper combination of these matrixes to yield a final transformation matrix. Because each element acts on the field successively, multiplying the matrices in reverse order applies each element to the beam chronologically. The final transformation matrix takes the form below in (3.19).

$$M_{Final}^P(A, \beta) = [M_P^P(-45^\circ)] * [M_{PEM}^P(A)] * [M_{2FR}^P(\beta)] * [M_P^P(45^\circ)] \quad (3.19)$$

$$M_{Final}^P(A, \beta) = \frac{1}{2} \begin{bmatrix} 1 & -1 \\ -1 & 1 \end{bmatrix} * \begin{bmatrix} \left( \frac{\exp -i \frac{A}{2}}{2} + \frac{1}{2} \right) \left( \frac{1}{2} - \frac{\exp -i \frac{A}{2}}{2} \right) \\ \left( \frac{1}{2} - \frac{\exp -i \frac{A}{2}}{2} \right) \left( \frac{\exp -i \frac{A}{2}}{2} + \frac{1}{2} \right) \end{bmatrix} \quad (3.20)$$

$$* \begin{bmatrix} \cos(2\beta) & \sin(2\beta) \\ -\sin(2\beta) & \cos(2\beta) \end{bmatrix} * \frac{1}{2} \begin{bmatrix} 1 & 1 \\ 1 & 1 \end{bmatrix}$$

The nice thing about linear algebra and order of operation is that matrix multiplication is associative but not commutative. Therefore, the matrices can be multiplied in any order as long as they are not rearranged which will follow for the rest of the derivation. This is also where it becomes apparent that shifting coordinates effects the ease of the calculation.

$$M_{Final}^P(A, \beta) = \frac{1}{2} \begin{bmatrix} e^{-i\frac{A}{2}} & -e^{-i\frac{A}{2}} \\ -e^{-i\frac{A}{2}} & e^{-i\frac{A}{2}} \end{bmatrix} \quad (3.21)$$

$$* \frac{1}{2} \begin{bmatrix} \cos(2\beta) + \sin(2\beta) & \cos(2\beta) + \sin(2\beta) \\ \cos(2\beta) - \sin(2\beta) & \cos(2\beta) - \sin(2\beta) \end{bmatrix}$$

For ease of calculation the shape of the final matrix takes the form below in (3.22) with the constants  $n$  and  $m$  described in (3.23) and (3.24) respectively.

$$M_{Final}^P(A, \beta) = \begin{bmatrix} n & n \\ m & m \end{bmatrix} \quad (3.22)$$

$$n = \frac{1}{4} \sin(2\beta) \exp\left(-i\frac{A}{2}\right) \quad (3.23)$$

$$m = -\frac{1}{4} \sin(2\beta) \exp\left(-i\frac{A}{2}\right) \quad (3.24)$$

This final transformation gives polarization manipulation needed to extract the final beam at the Nirvana detector. (3.25) demonstrates that the final electric fields dependence on the polarization transform and initial field.

$$E_f = M_{Final}^P(A, \beta) * E_i \quad (3.25)$$

The initial coordinate system chosen to solve the problem dictates how to define the incoming light. For a pure linearly polarized  $45^\circ$  signal, the initial field will take the form in (3.26).

$$E_i = \begin{bmatrix} E_x \\ E_y \end{bmatrix} = \left(\frac{1}{\sqrt{2}}\right) * \begin{bmatrix} A_x e^{i(\phi_x + 2\pi\nu t)} \\ A_y e^{i(\phi_y + 2\pi\nu t)} \end{bmatrix} = \left(\frac{1}{\sqrt{2}}\right) \begin{bmatrix} 1 \\ 1 \end{bmatrix} \quad (3.26)$$

Starting with this field and symbolically multiplying out (3.27) reveals an interesting property about the final field, (3.28), seen at the detector.

$$E_f = \begin{bmatrix} n & n \\ m & m \end{bmatrix} * \left(\frac{1}{\sqrt{2}}\right) \begin{bmatrix} 1 \\ 1 \end{bmatrix} = \left(\frac{1}{\sqrt{2}}\right) \begin{bmatrix} 2n \\ 2m \end{bmatrix} \quad (3.27)$$

$$E_f = \left(\frac{1}{\sqrt{2}}\right) \begin{bmatrix} \frac{1}{2} \sin(2\beta) \exp\left(-i\frac{A}{2}\right) \\ -\frac{1}{2} \sin(2\beta) \exp\left(-i\frac{A}{2}\right) \end{bmatrix} \quad (3.28)$$

Squaring the field at the detector and taking the real part yields the final intensity measured at the DC power.

$$I = \text{real}[(E_f)^2] = \text{real}\left(\sqrt{|E_x|^2 + |E_y|^2}\right)^2 = \text{real}\left(|E_x|^2 + |E_y|^2\right) \quad (3.29)$$

Euler's formula proves crucial for transforming the exponential sums and differences into trigonometric identities shown in (3.30).

$$e^{ix} = \cos(x) + i * \sin(x) \quad (3.30)$$

$$I = \text{real}\left(2 * \frac{(\exp(-iA) \sin^2(2\beta))}{4}\right) = \frac{1}{2} \cos(A) \sin^2(2\beta) \quad (3.31)$$

One important thing to note is that there will be noise and a DC offset in the signal that needs to be factored in at this point. A placeholder of C will represent this constant term.

$$I = \frac{1}{2} (\cos(A) \sin^2(2\beta) + C) \quad (3.32)$$

The constant C is assumed to be 1. This makes sense physically because the E field is oscillating from 0 to 1 with an average value of 1/2. The variable A is the rate of oscillation set by the photoelastic modulator, (3.17), and can be inserted at this point to yield (3.33).

$$I = \frac{1}{2} \cos(A_0 \cos(\omega_x t)) \sin^2(2\beta) + \frac{1}{2} \quad (3.33)$$

A series expansion exists where cosines of sines can be represented as a summation of Bessel functions. This relation pulled from *Table of Integrals, Series, and Products* book by Gradshteyn provides a much-needed expression to convert the sinusoid functions

into quantities related to products of Bessel functions and sinusoids at the second harmonic frequency.

$$\cos(z * \sin(\omega)) = J_0(z) + 2 \sum_{n=1}^{\infty} J_{2n}(z) * \cos(2n\omega) \quad (3.34)$$

$$\sin(z * \sin(\omega)) = 2 \sum_{n=0}^{\infty} J_{2n+1}(z) \sin((2n + 1)\omega) \quad (3.35)$$

Plugging in this Bessel function for the cosine starts the transition to the final rotation measurement, (3.36) includes the expansion for the cos (A) term.

$$I = \frac{1}{2} \left( J_0(A_0) + 2J_2(A_0) \sin(2\omega_x t) + \text{higher order terms (HOT)} \right) \sin^2(2\beta) + \frac{1}{2} \quad (3.36)$$

The higher order terms are negligible ( $\ll 1$ ) and can be ignored leaving the final approximation of I below.

$$I = \frac{1}{2} + \frac{1}{2} J_0(A_0) \sin^2(2\beta) + J_2(A_0) \sin(2\omega_x t) \sin^2(2\beta) \quad (3.37)$$

It is now easy to see that the total intensity measured at the detector is comprised of a DC frequency component and a second harmonic component. This leads to the two voltage relations below.

$$V_{DC} = \frac{1}{2} + \frac{1}{2} J_0(A_0) \sin^2(2\beta) \quad (3.38)$$

$$V_{2f} = J_2(A_0) \sin^2(2\beta) \quad (3.39)$$

Since these voltages are both measurable quantities it is possible to extract the rotation caused by the sample from the ratio of the two voltages

$$\frac{V_{2f}}{V_{DC}} = \frac{J_2(A_0) \sin^2(2\beta)}{\frac{1}{2} + \frac{1}{2}J_0(A_0) \sin^2(2\beta)} \quad (3.40)$$

Controlling the  $A$  value delivered to the PEM enables the use of the  $J_0(A_0)$  parameter to elicit certain responses for verification of the system performance [HINDS]. By adjusting  $A_0 = 2.405 \text{ rads}$  using the HINDS controller, the value  $J_0(A_0) = 0$ , making it drop out of the rotation equation.



Figure 3.6 Setting the  $A_0$  parameter on the HINDS controller

$$\frac{V_{2f}}{V_{DC}} = \frac{J_2(A_0) \sin^2(2\beta)}{\frac{1}{2}} = 2 J_2(A_0) \sin^2(2\beta) \quad (3.41)$$

Rearranging this equation gives the imparted Faraday rotation  $\beta$  in (3.42).

$$\beta = \frac{1}{2} \sin^{-1} \left( \sqrt{\frac{V_{2f}}{2 * J_2(A_0) * V_{DC}}} \right) \quad (3.42)$$

Figure 3.7 shows how the  $J_0$  function reaches zero and how it relates to the remaining  $J_2$  value in the rotation equation.

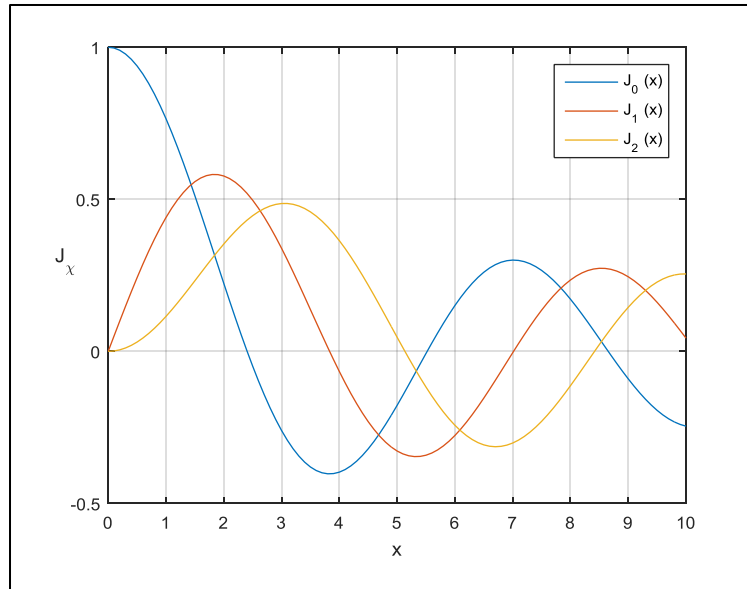


FIGURE 3.7 Bessel functions for  $\chi = 0, 1,$  and  $2$

Finally considering the Nirvana New Focus detector response at key frequencies the gain can be included for the two different measured responses. The vendor-provided data sheets of the responsivity and gain factors indicate how to scale signals when operating in “balanced” mode. Detecting above 50 kHz requires a 100X response increase and at DC only a 20x increase. Additionally,  $R(\lambda)$  influences each single but divides out in the final rotation equation. The 2017 curve is used for the responsivity measurements

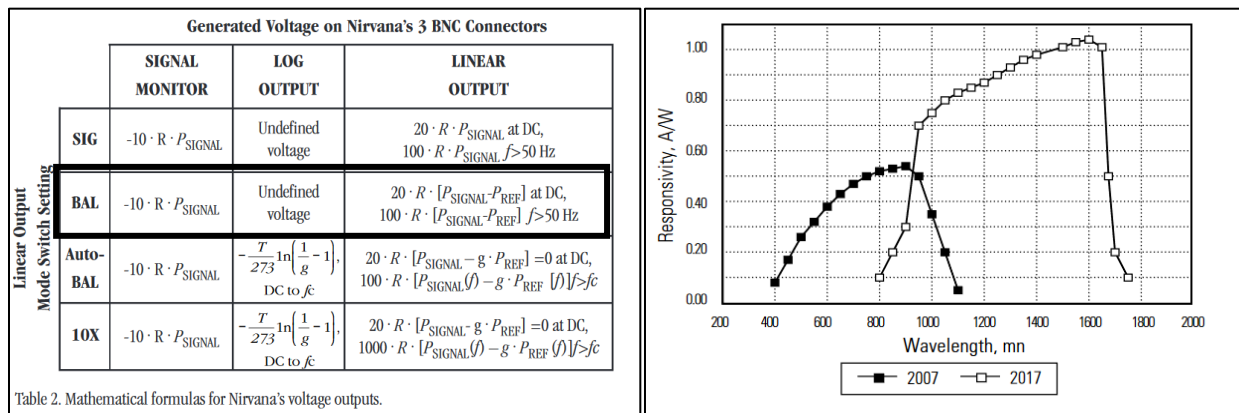


FIGURE 3.8 and 3. 9 Nirvana gain factors and responsivity [Nirvana]

From Figure 3.8 we get the gain factors associated with the detector at the given frequencies, which can be plugged into the above equation. Because arc sin is a relation

of two lengths, it gives the angle in radians in terms of the unit circle. To change the units of radians of arc sine to degrees an additional 180 over pi is included in (3.43).

$$\beta = \frac{1}{2} \left( \frac{180}{\pi} \right) \sin^{-1} \left( \sqrt{\frac{R(\lambda) * \left( \frac{V_{2f}(M)}{100} \right)}{2 * J_2(A_0) * R(\lambda) * \left( \frac{V_{DC}(M)}{20} \right)}} \right) \quad (3.43)$$

The final thing to consider is that the second harmonic measured voltage is the RMS voltage and therefore needs to be scaled by  $\sqrt{2}$ .

$$\beta = \frac{1}{2} \left( \frac{180}{\pi} \right) \sin^{-1} \left( \sqrt{\frac{20 * V_{2f}(M)}{2 * \sqrt{2} * J_2(A_0) * 100 * V_{DC}(M)}} \right) \quad (3.44)$$

(3.44) will be utilized for transforming the measured data from the test set up into a rotation quantity for the material under test.

### iii. Test parameters

In the Faraday rotation test procedure a small optical path length sample is placed in a concentrated magnetic field and the amount of polarization rotation is measured while mapping a trade space of various environmental parameters.

Exploring warm temperatures from 295°K to 340°K at a fixed magnetic field of +600mT enables the rotation per field as a function of temperature to be determined. Owing to the cooling method and physical size of the cryostation, certain test values are dictated. Utilizing a magnetic field over a range from +600mT down to -600mT gives over 1 Tesla dynamic range within the confined space.

In order to perform cold temperature testing, or below a room temperature of 295°K, the cryostation evacuates the chamber before cooling. The closed system liquid nitrogen and helium loops plus to a vacuum help reach and maintain the chamber temperature down to 5°K. Liquid nitrogen boils at 77°K and freezes at 63°K, cooling the sample to the point where liquid helium cooling kicks in and stays liquid down to 4°K. To test as low as 2°K the station pulls an additional high-pressure vacuum. This removes any

extraneous particles reducing the momentary energy within the small volume and making it much easier to cool. To reach any temperature between 29°K and 2°K, the cryostation evacuates the chamber down to 5°K before warming up to the temperature under test.

One area of research that has not been fully explored is the interaction of these ionic liquids at cold temperatures, particularly below 79°K. Because most materials have freezing points well above 5°K, the Faraday properties around this transition point can be explored. This property also leads to two different cooling options. In one case no magnetic field is applied during cooling, solidifying the liquid in an unaligned state. In the second case, a magnetic field is applied during cooling, freezing the liquid in the rotated orientation. This testing reveals information about the response of the material to cryogenic testing conditions in such environments as extreme pressure or vacuum. This opens up the possibly for applications in space or deep under water.

#### iv. Verification and validation of test equipment

Sweeping the empty chamber through the environmental conditions verify system performance while also providing a background noise baseline. Characterizing the Faraday rotation of a blank glass cell under an applied field at various temperatures provided the fused silica interaction needed, which is subtracted from the sample rotation.

Both references were measured with a magnetic field sweep of -600mT to 600mT and over temperature sweeping from 295°K to 340°K and 2°K to 295°K. The extracted window rotation data can be compared to the known published values for fused silica to validate the rotation measurement. The operation of the Nirvana detector is verified by examining the DC power and phase at the chopper frequency, which should be  $\sim 1/2$  the input power, from the chopper wheel, with unchanging polarization from the polarizer. Polarization is confirmed by minimizing the power at the first harmonic which represents the DC offset between the magnitudes of  $E_x$  and  $E_y$ .

To ensure polarizer alignment, we note that if the polarizers are truly cross-polarized the power out becomes 0 at the DC frequency. Therefore, rotating the initial polarizer until the power reaches a minimum for the 100 kHz frequency yields the best

extinction expected from the system. The third harmonic of 150 kHz gives the degree of ellipticity.

#### d. LCOF Measurement

##### i. Test Set Up

The liquid core optical fiber (LCOF) test set up measures rotation due to a length of Faraday rotating material enclosed within fiber. Similar to the free-space Faraday rotation set up described above, we start with a common pump wavelength of 980nm, where the source for testing the isolator was a laser diode with 110mW of output power. A non-PM output fiber spliced on to an additional section of HI 1060 gave a length long enough to loop through a 3cm diameter, 3 paddle polarization controller to optimize the polarization state launched into an In-Line Fiber Polarizer from ThorLabs (part number ILP980PM-FC). This polarizer operates at  $980 \pm 10$  nm and has a PM to PM pigtail along with a flat cleaved /physical contact connector [980Polarizer].



FIGURE 3.10 Seed, isolator, and polarization paddle LCOF setup

The polarization of the initial electric field is aligned to match the fast axis of the polarizer through manipulation of the polarization paddles, which maximized throughput into the LCOF. We used a model 2001-FS-M silicon photoreceiver from Newport, a free space silicon detector that is responsive from 300-1050 nm at a 200 kHz rate and has M4 mounting [LCOF Detector].

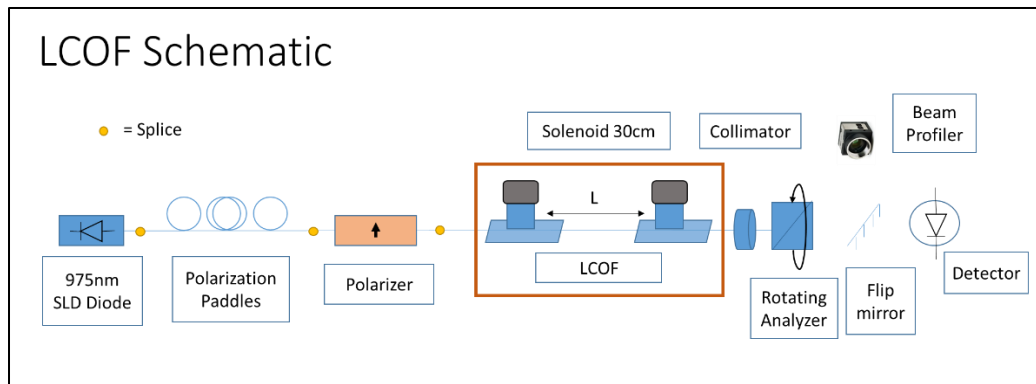


FIGURE 3.11 Liquid core optical fiber test schematic

Results from the ionic liquid measurement can be used to determine the chain length of hollow core fiber. However, premade fiber chain lengths are tested and utilized for vetting the performance of the system. Splicing the polarizer onto the LCOF input using a standard PM980 to PM980 splice maintains polarization into the liquid. The output HI1060 is cleaved  $>5\text{mm}$  from the end of the chain support by utilizing a standard fiber cleaver. A  $\mu\text{Eye}$  camera from Thorlabs then images the fiber end face using a flip mirror in the beam path, turning it  $90^\circ$ .

To keep the beam from diverging, a collimating lens is placed a focal length away from the fiber end and sends the light down the diagnostics path. A linear polarizer mounted on a rotation stage from Newport sweeps the field from  $0^\circ$  to  $360^\circ$  using a DC servo motor [Newport Rotation]. A LabVIEW code talking to the polarizer and photoreceiver relates intensity as a voltage to the polarizer's position. The photoreceiver operates in multiple modes with gain up to 40dB and output powers on a scale of 4V. The output voltage of the detector was read on an oscilloscope, allowing for manual alignment and adjustment of the polarization.

Once the fiber is integrated into the system, it is strategically placed in the center of a 30cm long solenoid wound in wire connected to a power supply. Electrical current running through this wire creates a quantifiable magnetic field around the liquid acting as a source for rotating the polarization of the light traversing the ionic liquid.

## ii. Test Parameters

Once the fiber chain sample is in place, the solenoid will be turned on to N amps for a duration  $T_{on}$ . The rotating analyzer will step through a rotation from 0 to 360, at intervals of  $5^\circ$ - $15^\circ$ . Each time the solenoid ramps on, the detector will take a power measurement (read out as a voltage), and correlate it to the analyzer angle, then when the solenoid turns off for a duration  $T_{off}$  for the solenoid temperature to stabilize the rotation analyzer moves to the next location. The sample spacing and time durations are optimized based on the thermal effects of the solenoid under current. A thermocouple is positioned inside the cylinder to monitor temperature at each scan interval. The “ramp on time” or time it takes the solenoid to reach full voltage is calculated with an oscilloscope and factored into the sample durations.

Sweeping the polarizer across the full rotation relates power to a physical angle corresponding to how much power is contained in the  $E_x$  and  $E_y$  states, respectively. Measuring this power with and without a field quantifies the power shift between these two states as a function of the field strength.

### iii. Polarization through the system

To ensure proper polarization manipulation when exiting the source, the polarization paddles must be of the correct diameter. Replicating a quarter wave plate, half wave plate, quarter wave plate system, one loop in the paddle must be enough to rotate the seed wavelength  $\phi = 0.25$  waves. A standard 3 paddle set from Thorlabs having a diameter  $D$  of 27mm works well for the 125um diameter  $d$  of the HI1060 fiber at an operating wavelength  $\lambda$  of 980nm. Then utilizing the constant  $a = 0.133$  for silica fiber a total rotation of 0.2468 times the number of loops, N, emerged from (3.45) making it a suitable system.

$$\phi(\text{waves}) = \frac{\pi a N d^2}{\lambda D} = \frac{\pi (.133) N (125\mu\text{m})^2}{(980\text{nm})(72\text{mm})} \cong .2468N \quad (3.45)$$

Power optimization confirms that polarization paddles are in the proper configuration before splicing through to the isolator. Maximizing power through the

isolator ensures maximum power delivered to the sample under test. The PM output and PM input aligned with a splicer maintains the fast axis of light and thus power transmission between these two components.

The diagnostics path first needs to confirm alignment of the cleaved fiber through the collimator before addressing collimation. First collimation is addressed by adjusting the path length between the fiber and lens then the centroid is stabilized, using tip tilt pitch and yaw. With a properly collimated beam, a polarizing element such as the rotating analyzer in the beam path proves sufficient to decompose the beam. Figure 3.12 depicts how linearly polarized light with an initial transmission axis  $\beta$  results in a cosine function intensity after passing through the analyzer sweeping with transmission angle  $\alpha$ .

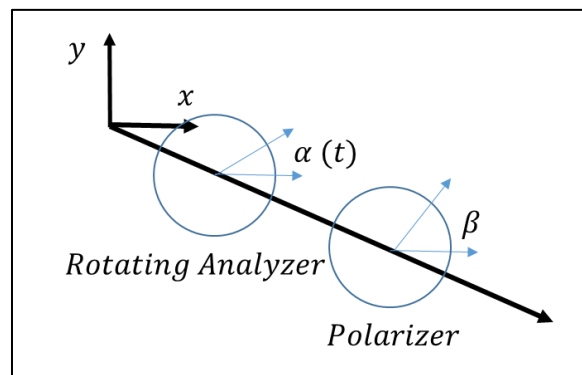


FIGURE 3.12 Rotating analyzer transmission geometry

When  $\alpha$  is aligned with  $\beta$  the transmission voltage observed by the detector is maximum and any extraneous light that is not linearly polarized shows up in a non-zero voltage at the minimum. Naturally, this includes subtracting for background noise by taking a reference scan of the ambient light.

#### iv. Applied magnetic field (Solenoid)

Utilizing an ideal solenoid, one in which “the turns are closely spaced and the length is much greater than the radius of the turns” [Serway], enables a derivation of the ideal magnetic field within the solenoid simply from one of the fundamental Maxwell’s equations. Taking a cross section of the solenoid and applying Ampere’s law to the closed

loop section drawn around the coils depicted in Figure 3.13 determines the magnetic field found in the center of the coil. This “Amperian loop” is used parallel to the body of the solenoid and represents the magnetic field seen by the fiber under test in the center of the solenoid.

$$\text{Ampere's Law: } \nabla \times B = \mu_0 J \quad (3.46)$$

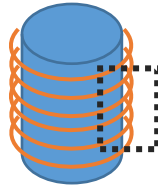


FIGURE 3.13 Amperian loop around a solenoid wound with wire coils

Contributions along the top of the rectangle are zero because the B field is propagating perpendicular to the length differential. Therefore, the B-field equation reduces to a line integral over the length parallel to the solenoids axis as given below in (3.47).

$$\int_{-\frac{L_c}{2}}^{\frac{L_c}{2}} \vec{B} \cdot d\vec{l} = BL = \mu_0 N I_{enclosed} \quad (3.47)$$

$$B = \frac{\mu_0 N I_0}{L} \quad (3.48)$$

To compensate for not being an infinitely long system, centering the sample within the coil helps the sample see the same average magnetic field. Figure 3.14 shows the test set up coil straight on and top down profile. Note the thermocouple attached to the solenoid before the testing began. During this testing, the temperature probe is centered within the solenoid length for accurate temperature readings.

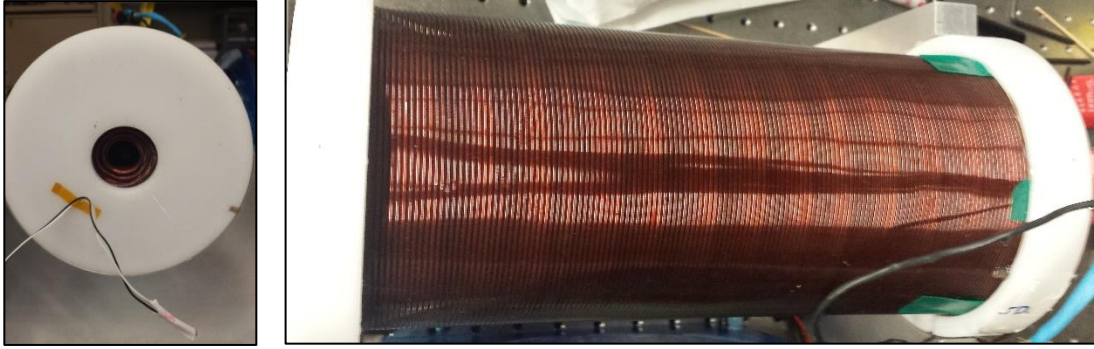


FIGURE 3.14 Solenoid optical axis and top down views

A 30cm length coil made of 12 A.W.G. wire with approximately 138 loops along the top of the coil, and a depth of 6cm or  $\sim 29$ , with an assumed average wire diameter of 2.1mm and staggered stacking gives a total of  $N \cong 4002$  coils. Using (3.48) with constants for magnetic susceptibility  $\mu_0 = 4\pi * 10^{-7} N/A^2$  and a conversion of  $T=N/(Am)$  yield a B field strength as a function of current  $I_0$  in units of mT.

$$B = 4\pi * 10^{-7} (Tm/A)(4002)I_0/(0.3m) = 16.764 * I_0 \text{ mT/A} \quad (3.49)$$

(3.49) gives the theoretical value of the field within the solenoid. Measuring the field using a gauss meter verifies the actual field imparted to the sample. Ideally, the current will need to be  $\sim 5A$  to achieve approximately an 83.8mT field but as high as 7A to achieve a 117.4mT field.

#### v. Chain structure

The most challenging aspect of sample fabrication came down to creating the delicate splices. Preparing each fiber by removing the protective acrylate or polyamide buffer exposes enough of the glass waveguide for splicing. Coatings, if not properly removed, will interfere with the blade in the cleaving process. The hollow core polyamide buffer was removed by manual stripping with a razor blade while the PM 980 and HI1060 fluoro-acrylate buffer has a lower melting point and can be stripped with a thermal stripper. After buffer removal, cleaning with methanol and acetone removes any large debris, oil, or dirt. A special angle cleaver is used for the PM 980 fiber along with the HI

1060; this cleaver clamps down on the fiber in two locations and rotates the input fiber clamp imparting torsion while providing tension to the fiber. Once the blade strikes the fiber it will create a crack that is propagated in an angular motion as the fiber is relieved of its torsion creating a slight angle in the fracture plane. This angle is evident in Figure 3.15 in the left-hand fiber.

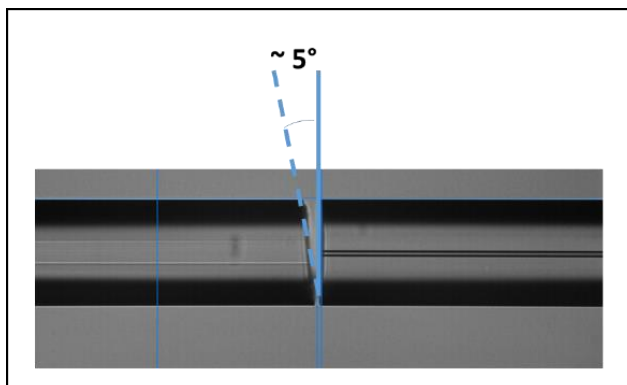


FIGURE 3.15 Angled fiber splice

An all-in-one Vytran FFS-200 model capable of cleaning, cleaving, inspecting, splicing, and recoating, this system performs the splice from start to finish, with a mount that transfers between all stages. Utilizing only the splicer, the stage benefits include end-face viewing for inspection of fiber cleave quality or cleanliness before splicing. The software included an easy graphical user interface (GUI), two camera positions, and two mirrors for full fiber inspection. Manual splice setting customization included: preheat temperature, preheat time, arc temperature, and hot push time. Standard splice parameters for the 6 $\mu$ m core were modified to achieve the appropriate amount of fiber melting and fusing to maintain the hollow core opening and create a secure enough bond to be transported. Optimized for use from research to repetitive manufacturing, this splicer discharges a direct current across carbon filaments to “arc” fuse glass fiber together creating a low-loss glass interface. The arc reaches temperatures of 1500°C, hot enough to melt glass and create a bond.

Once spliced the fragile fiber interface is epoxied onto a microscope slide using tape for initial stabilization. The top half of a clean glass vial with fiber tunnels or key holes is placed on top of the fiber, which passes safely underneath without contact. To

permanently protect the splice and contain the filling liquid, the vial is glued on top of the slide and the key holes are sealed up with non-light stripping epoxy.

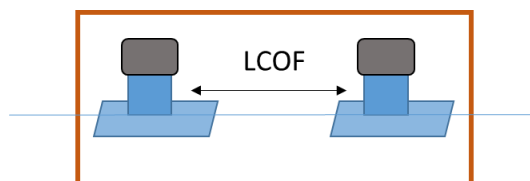


FIGURE 3.16 LCOF chain structure

Additional Norland 81 epoxy applied on either end of the chain helps to affix the fiber to the chain structure, a long wooden stick in this case. This low absorption epoxy proved malleable enough to control the fiber location before a quick UV cure [Norland 81].

#### vi. Filling the chains

Filling the liquid into the hollow core fiber is dependent on small-scale capillary action and therefore can be a time intensive process. A syringe pump speeds up this process; filling the chains to a specified amount by slowly depressing a syringe plunger with a fine step motor injects the ionic liquid into a plastic tube. Poly(tetrafluoroethylene) (PTFE) tubing connects the syringe to the vial cap protecting the chain opening. The NE-1000 programmable model shown below in Figure 3.17 from New Era Pump Syringe Inc. has a programmable interface including ramp up, step speed, and time [New Era]. The mount holding the syringe and plunger resides on top of the device in spring-loaded holders.



FIGURE 3.17 New Era syringe pump

Most of the liquids chosen have high visible attenuation, one indicator of this being the dark brown hue apparent in the iron liquid material. Although potentially dim due to absorption, a red LED was coupled into a keyed SM fiber patch cable spliced into the input of the chain under test during the filling process. By observation, verification of a “filled” chain comes from following the liquid filling meniscus and air interface scattering down the length of fiber. Additionally, a resistive heater in the form of a long strip, expedites the filling process when wrapped around the syringe, by elevating material temperature viscosity is decreased.

#### vii. Verification and validation of test equipment

Beam alignment is performed by maximizing the power on the detector. Aligned first without the rotating analyzer, the collimator following the fiber output provides all of the beam manipulation power. The power is maximized by adjusting the focus onto the detector and confirming with the  $\mu$ eye camera. The rotating analyzer put in the optical path then gives a method of measuring polarization. However, because the fiber had limited movement capabilities the collimating lens additionally had linear translation and rotation to steer the beam.

Verification of the linear polarization required placing a polarizer in front of the rotating analyzer. This polarizer was aligned with the polarization axis of the collimated beam, thereby passing a single polarization to the analyzer. When the rotating analyzer rotates, it will have a sinusoidal intensity output as a function of the rotation angle due to Malus’s Law. This verifies the alignment of the set up and that the light is polarized, coming to extinction every time the polarizers are  $\pi$  phase shifted. The polarizer can then be rotated  $90^\circ$  to fully block the signal and another sweep taken. This scan should have a null output intensity as a function of  $\theta$ . Any residual power is nonlinear polarization or background noise.

Calibration of the thermocouple in the solenoid provides a calibration scale for the thermocouple output to an actual temperature. Taking a calibrated thermometer and

measuring the temperature while simultaneously recording the thermocouple output provides for conversion of the measured arbitrary units into Kelvin.

This calibration is similarly done to verify the field within the solenoid as a function of the current applied by the power supply. This result is compared to the theoretical prediction of the solenoid field. The current is driven from -7amps to +7amps and the magnetic field is measured at each current with a gauss meter in units of Gauss.

## IV. Findings and Results

### a. Material verification

#### i. UV-Vis spectrum

The first key result is the measurement of material absorption across a wide spectral range. Examining the absorbance as a function of wavelength, we find that the maximum transmission wavelength for iron BMIM, or below 0.1 dB/cm absorption included 900-1100nm, 1200-1250nm, and 1300-1350nm. Diazole consists of an aromatic structure with two nitrogens and three carbons. In particular, the imidazole (or 1,3-diazole) gives some strong spectral absorptions in the UV and far IR region. An amine between two functional groups approximately yields a resonance at 1490-1580  $\text{cm}^{-1}$  wave numbers or 6.7- 6.4 $\mu\text{m}$ .

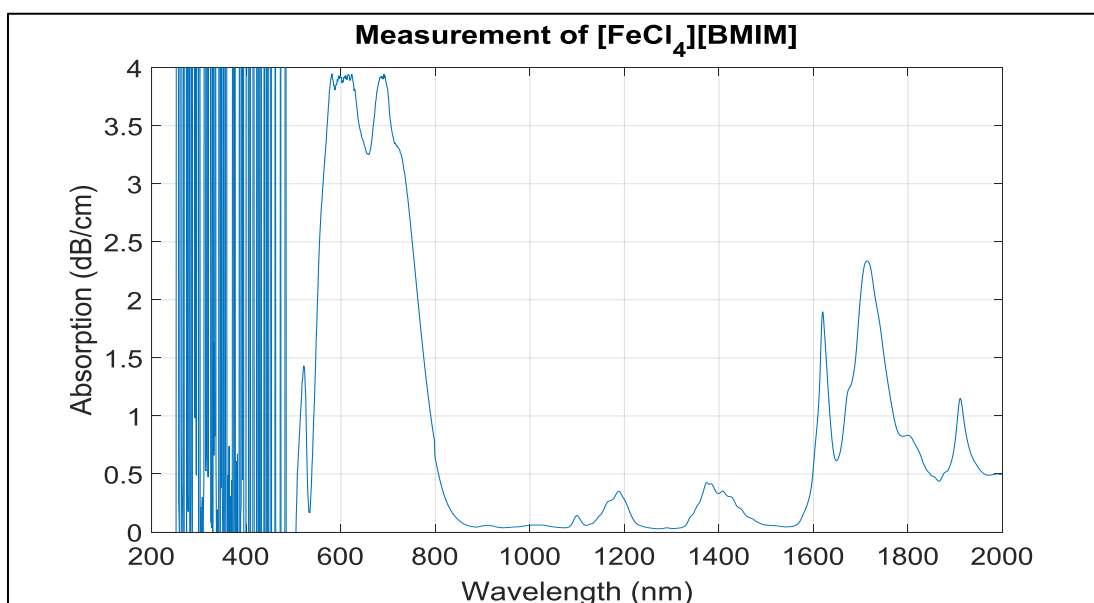


FIGURE 4.1 Absorption of [BMIM][FeCl<sub>4</sub>] from 200 to 2000nm

The addition of  $Fe^{3+}$  metal ion affects the spectrum predominately from the electronic transitions states. With transitions starting at 300nm the lack of detailed information below 500 nm is attributed to multiple high frequency transition states, organic absorption, and scattering. A sharp peak appears at 520nm with a broader absorption over 582nm to 626nm most likely attributed to the  ${}^4G - {}^2D$  ( $\sim 593\text{nm}$ )  ${}^4P -$

${}^2_3F$  ( $\sim 596\text{nm}$ ) transitions. Finally, the 687-695nm peak and 710nm roll off comes from the  ${}^4P - {}^2_5D$  (689nm-713nm),  ${}^4D - {}^2_3F$ ,  ${}^4D - {}^4F$ , and  ${}^2_5D - {}^2_3D$  (703-710nm) transitions.

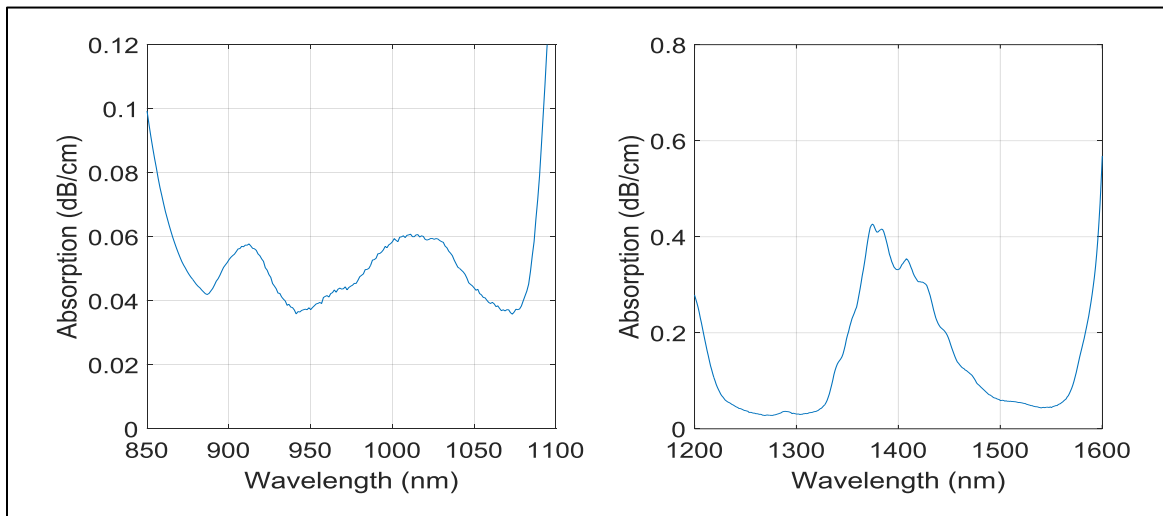


FIGURE 4. 2 Absorption of [BMIM][FeCl<sub>4</sub>] in the 850 to 1100nm and 1200nm to 1600nm regions

The key telecommunications wavelengths we are concerned with particularly include 980 nm, 1 um, 1310 nm, and 1550 nm. A close up of the spectrum above shows the absorption from 850 nm to 1100 nm and 1200 nm to 1600 nm for coverage of these key regions. Table 4.1 below gives the absorption per length of material per wavelength.

Operating wavelength (nm)	Absorption per length (dB/cm)
895nm	0.0529
980nm	0.0475
1064nm	0.0418
1310nm	0.0315
1550nm	0.0471

TABLE 4.1 Absorption measurements of iron BMIM at key wavelengths

From this spectrum, at the key wavelengths to consider for the test set up, 980nm and 1310nm, have absorption losses of 0.0475dB/cm and 0.0315dB/cm, respectively. This equates to approximately a total loss of 0.4dB over a 10cm length from material at these key wavelengths.

The second material tested had of a light pink hue and contained the erbium ion, with more favorable transmission in the 1.3um region and potential visible transmission. The UV Vis spectrum in Figure 4.3 indicates the ideal testing wavelengths for this ionic material.

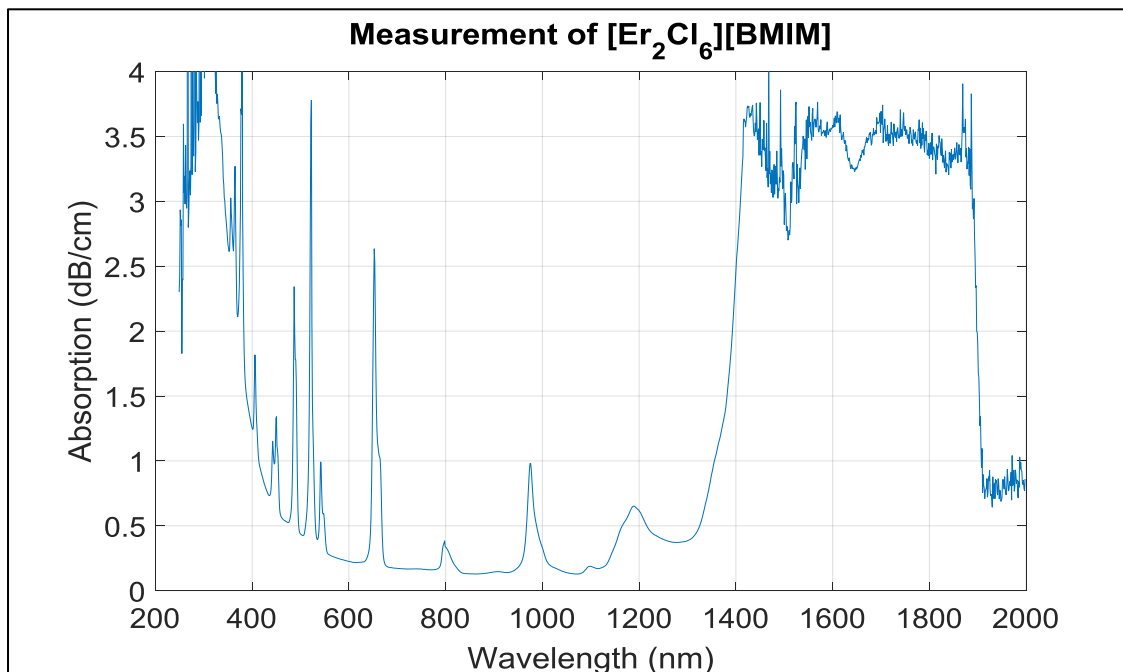


FIGURE 4.3 Absorption of [BMIM][ErCl<sub>6</sub>] from 200 to 2000nm

The spectral absorption of [BMIM][ErCl<sub>6</sub>] differs from the iron spectrum due to the different ion interactions, size, and ionic resonance levels. The discrete, atomic line peaks better demonstrate the allowed energy levels of the ion's electrons and are typical of a rare-earth ion. At these levels, electrons have an increased probability of rotating around the nucleus causing high interaction with incoming light and thus high absorption. The peak transmission for the erbium BMIM, or areas below 0.2 dB/cm included 500-800nm, 850nm to 1.1μm, 1.2μm to 1.4μm, and 1.9μm to 2μm demonstrated in Figures 4.4 through 4.5.

The key transitions mentioned in Table 3.2 appear as strong absorption peaks in the graphs from interaction with the electron transition levels. High absorption in the visible proves consistent with the  ${}^2H_{11/2} - {}^4G_{11/2}$ ,  ${}^2G_{9/2} - {}^4F_{9/2}$ ,  ${}^2P_{3/2} - {}^2D_{3/2}$ , and  ${}^2H_{9/2} - {}^2G_{9/2}$  transitions (~274-526nm).

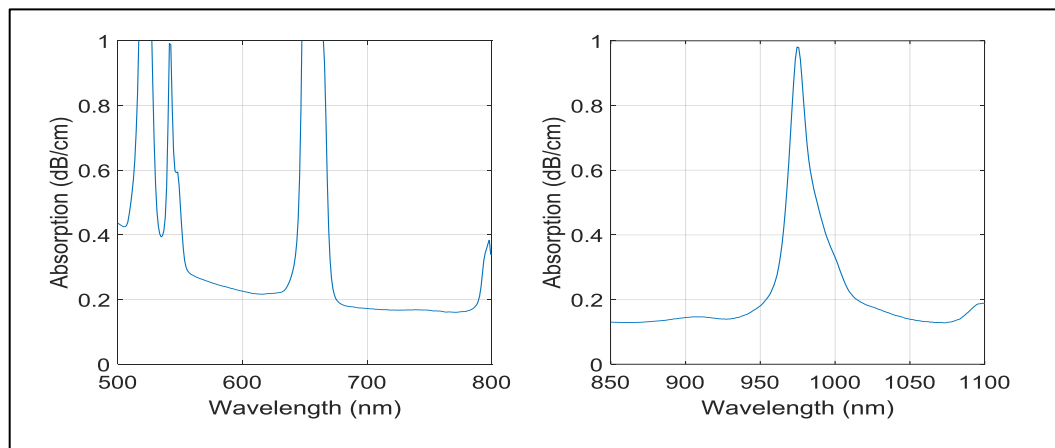


FIGURE 4.4 Absorption of [BMIM][Er<sub>2</sub>Cl<sub>6</sub>] in the 500 to 800nm and 850nm to 1100nm regions

The  ${}^4F_{9/2}$  band around 657nm and the  ${}^4I_{9/2}$  band from 810-815nm both make an appearance in the left-hand graph, each being slightly blue shifted. The higher electronic band absorption of  ${}^4I_{11/2}$  appears at 987nm in the right hand-graph.

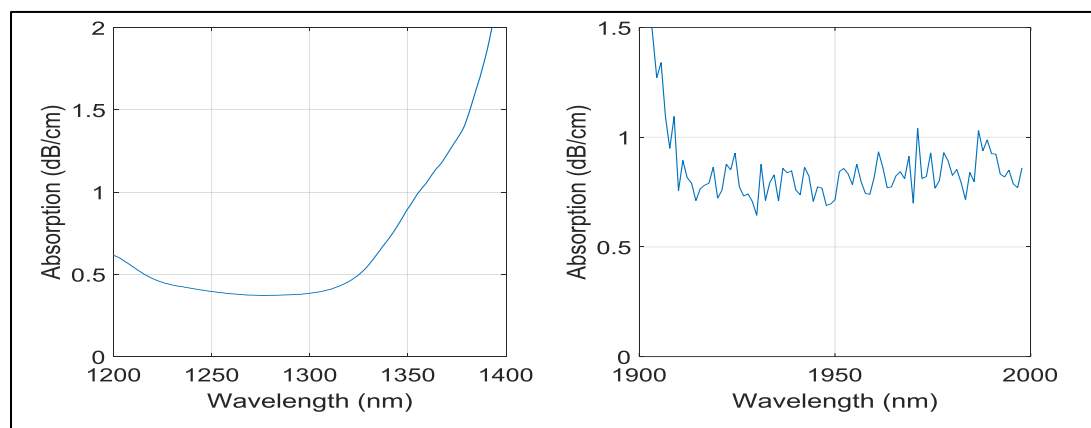


FIGURE 4.5 Absorption of [BMIM][ErCl<sub>6</sub>] in the 1200nm to 1600nm and 1900nm to 2000nm regions

The  ${}^4I_{13/2}$  band from 1520-1540nm does not appear in the transmission close ups above. The windows above show potential low loss at key wavelengths such as 1310nm

and  $2\mu\text{m}$ . The transmission also slightly differs at the key wavelengths with  $0.742\text{dB/cm}$  absorption at  $980\text{nm}$  and  $0.407\text{dB/cm}$  absorption at  $1310\text{nm}$ ; the  $\text{Er}^{3+}$  atom is more favorable to operation at  $1310\text{nm}$ , the lowest dispersion wavelength for standard optical fiber.  $\text{Er}^{3+}$  is often combined with  $\text{Yb}^{3+}$  to get better absorption of pump light at  $980\text{nm}$  proving an example of absorption in the near IR. Table 4.2 details the absorption at the same key wavelengths.

Operating wavelength (nm)	Absorption per length (dB/cm)
895nm	0.142
980nm	0.742
1064nm	0.131
1310nm	0.408
1550nm	3.493

TABLE 4.2 Absorption measurements of erbium BMIM at key wavelengths

One option for measuring the material refractive index is the Abbe refractometer, however both the source and the detector operate only at the Abbe wavelengths. This means that the index measured only goes up to  $800\text{nm}$ , so with the high visible absorption present in this liquid there is no real option to use an Abbe refractometer for a refractive index measurement.

## ii. Absorption spectrum within fiber types

The fibers within the system introduce additional transmission losses. Samples of the same lengths are compared in Figure 4.6, showing power transmitted in dBm versus wavelength. Taken utilizing a super-continuum source from  $500\text{nm}$  to  $1600\text{nm}$  the top red line in Figure 4.6 shows input power per wavelength. A background test of pure SMF

28 fiber, in purple, shows the least attenuation. For this fiber the reduction in transmission from the reference is primarily caused by coupling losses in and out of the fiber.

The addition of the liquid core optical fiber (LCOF) into the chain shows an in situ measurement of absorption. Two of the fiber layouts tested have the SC source spliced into the LCOF directly with varying termination by angle polished connector (APC) and face connector (FC). Additionally, this SC source was coupled in with SMF and then spliced to the LCOF filled with a different viscosity  $[\text{ErCl}_6][\text{BMIM}]$ .

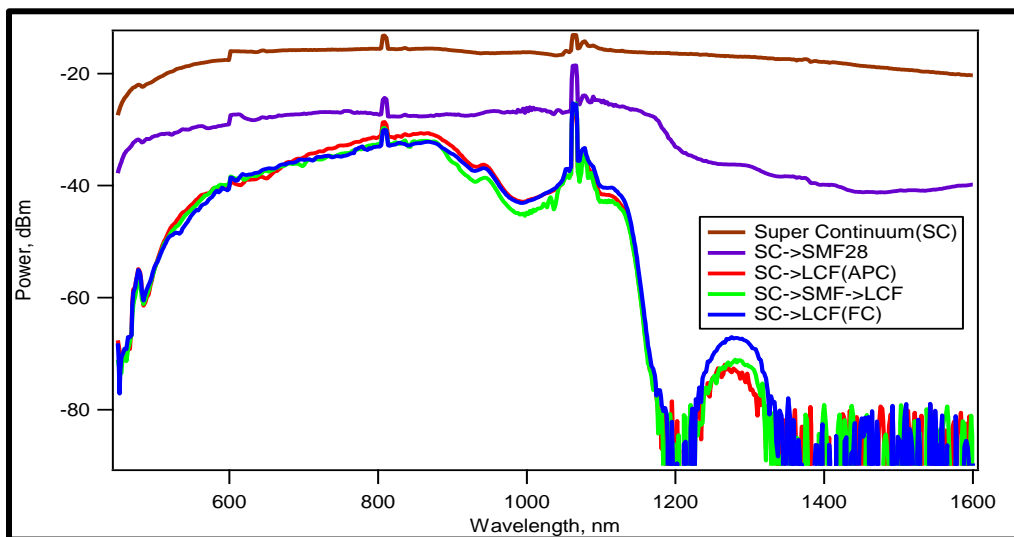


FIGURE 4.6 Supercontinuum sweep from 500 to 1700nm of SMF and LCOF filled with  $[\text{ErCl}_6][\text{BMIM}]$  with different termination

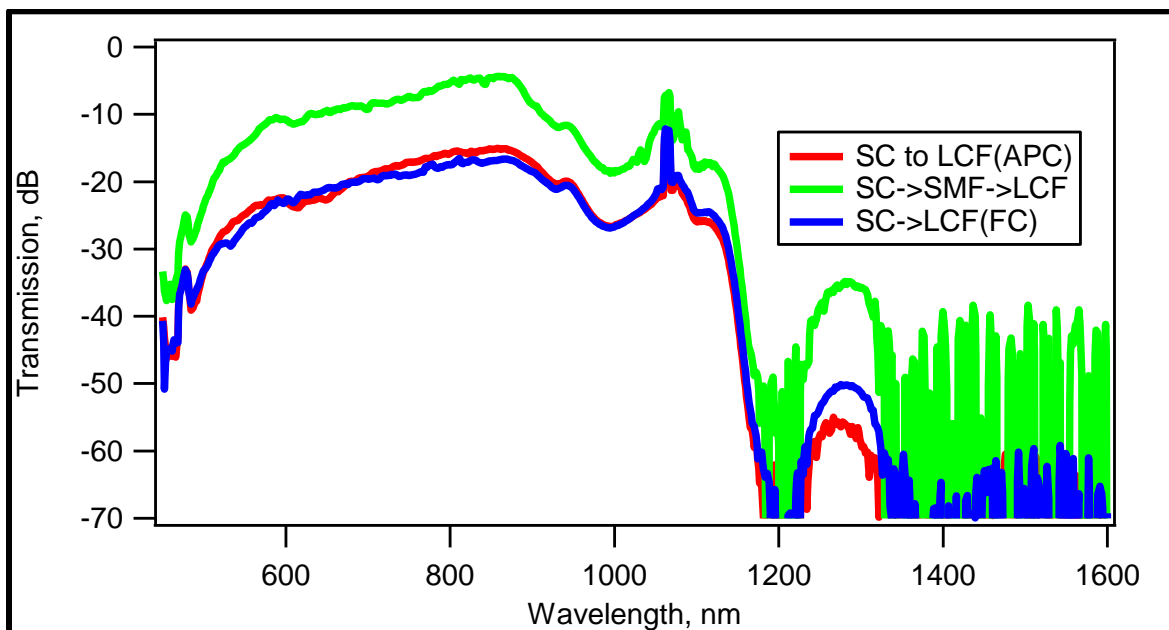


FIGURE 4.7 Transmission of LCOF filled with  $[\text{ErCl}_6][\text{BMIM}]$  over 500nm to 1700nm

Subtracting the 3 LCOF samples from the supercontinuum source yields the total transmission in dB of the chains in Figure 4.7. The best result was achieved using an SMF fiber between the SC source and LC fiber. This better coupled light into the core resulting in the lowest loss. Then, when comparing termination a slight benefit is observed in the visible with the angle polished connector (APC) reducing the loss from the fiber interface to the detector, while the flat connector had a slight edge around 1300nm. Inspection of the main operating wavelength of 980nm reveals up to 17 to 26 dB loss depending on coupling scheme.

## b. Faraday rotation measurement

### i. Creating the sample chamber

To house the material under test a glass chamber constructed from microscope slide cells covers created a U shape channel. This chamber when sealed contains the liquid in a secure enough method for environmental and vacuum testing. A single cell measures 245 $\mu\text{m}$  thick with dimensions of 1in x 1in. One full slide comprised either side of the chamber's main windows. Cutting a third microscope slide into three strips using a

diamond edged glass cutting blade created a bottom barrier and two side barriers measuring  $\sim 0.25\text{in} \times 1\text{in}$  and  $0.25\text{in} \times 0.75\text{in}$ , respectively, to create the sample cell shown below.

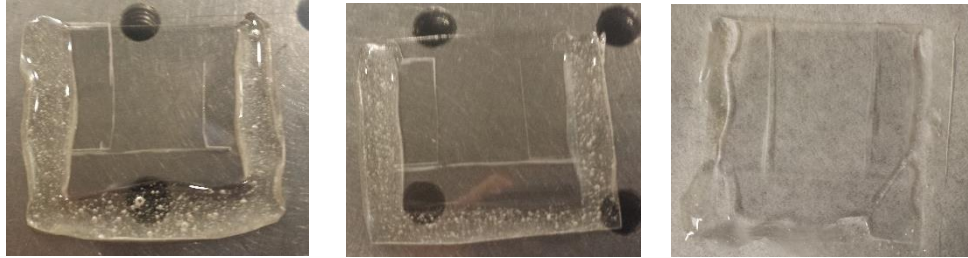


FIGURE 4.8 Liquid cell comprised of 3 microscope slides epoxied together

For a liquid tight barrier, thermal epoxy was deposited to seal in the edges. Norland Epoxy 81[Norland 81] was used since it can withstand various solvents, extreme environmental ranges, and a strong vacuum. Since the sample window is only  $245\mu\text{m}$  in width, capillary action fills in the space between the slides by applying only a few drops of the liquid at the top of the chamber. “The liquid under test is isolated from the internal chamber by sealing the top opening with the same epoxy. Finally, the sample is thermally isolated from the chamber walls by holding it in place with a low coefficient of thermal expansion (CTE) stand.

## ii. Temperature dependence

Operating the super luminescent diode at  $110.5\text{mW}$  gave enough optical power to detect at the two Nirvana sensors. Losing half the power from the spinning chopper wheel and then splitting power again at the beam splitter (excluding other optic losses) leaves  $\sim 27.6\text{ mW}$  total or  $13\text{mW}$  at each detector.

The three lock-in amplifiers connected to the Nirvana detector record the phase and amplitude of the detected power at several different frequencies. The plots below show the four key frequencies measured for each test. The DC power at the chopper frequency of  $\omega_{DC} = 1\text{ kHz}$  resides in the upper left plot while the upper right hand graph plots the photoelastic modulator oscillation  $\omega_1 = 50\text{ kHz}$ . The lower two plots are harmonics of the PEM with the key frequency of  $\omega_2 = 100\text{ kHz}$  used to extract polarization

rotation in the lower left, and the third harmonic  $\omega_3 = 150$  kHz in the lower right. From this voltage, the phase information can be extracted and separated from the amplitude.

Running a scan of the cryostation with the fused silica cell provides a baseline measurement which is subtracted from the sample measurement. This enables extraction of the rotation from the ionic liquid alone when comparing the filled sample chamber to an empty one.

A carefully seated blank fused silica cell was tested in the chamber to provide a sample reference over the 300°K to 340°K temperature range. This measurement should correlate to the expected variation of fused silica Verdet constant with temperature. The detected voltages at the key frequencies pulled directly from the set up are plotted in Figure 4.9. This scan relates temperature in Kelvin to rotation in degrees at a steady magnetic field of 600mT.

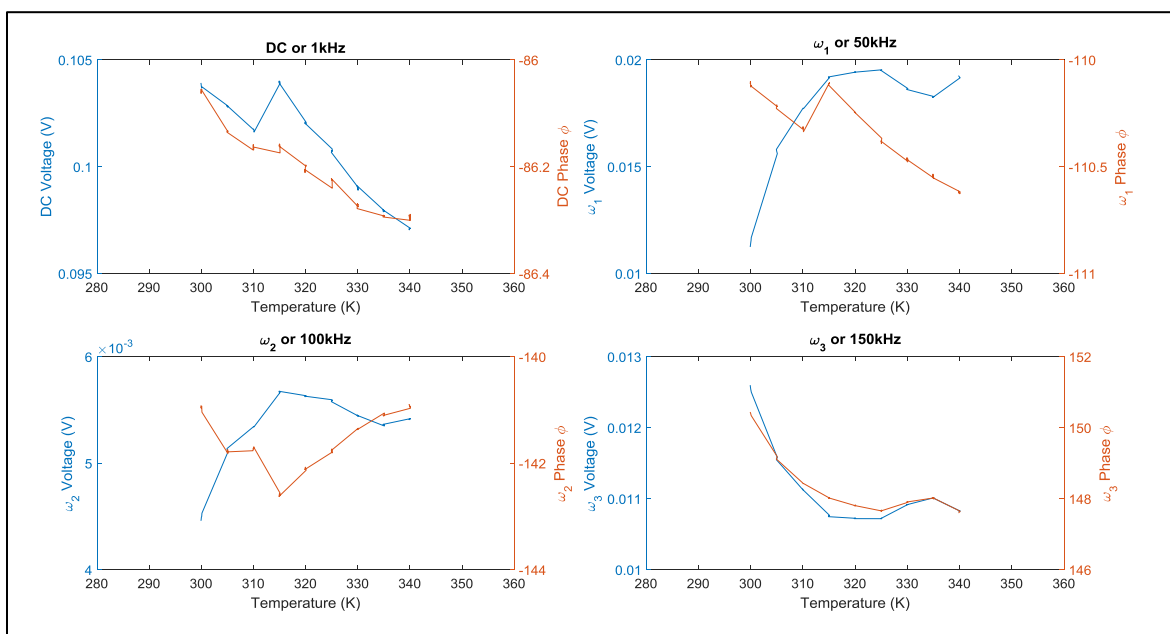


FIGURE 4.9 Detected Faraday rotation signal for a blank fused silica cell vs. temperature

Each frequency plot contains the raw voltage data reading and a phase in degrees, plotted in blue and orange respectively. The second harmonic voltage passes through each polarization twice because of the PEM. Taking the sign of the phase and multiplying by

the voltage yields the corrected amplitude data. Including this phase correction, Figure 4.9 becomes the corrected Figure 4.10 which better demonstrates the values necessary for describing the fused silica cell Faraday rotation.

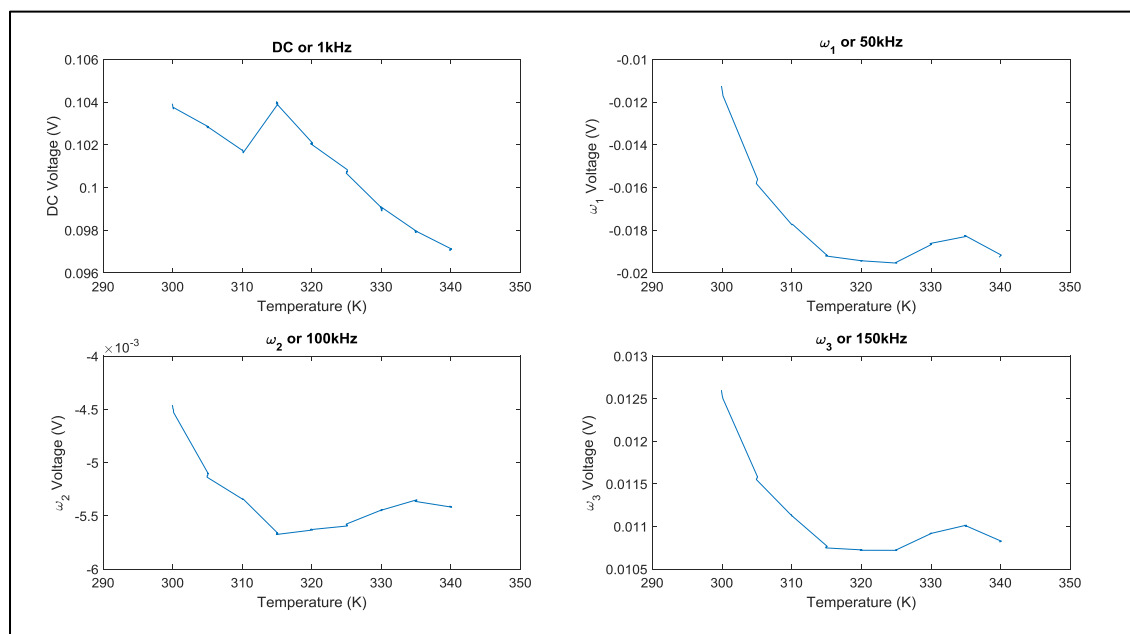


FIGURE 4.10 Corrected voltage for a blank fused silica cell vs. temperature

The three harmonics of the PEM have similar shapes, although the third harmonic has opposing sign, while the DC voltage decreases with increasing temperature. The decreasing DC voltage has a slight jump around 315°K and seems to be a transition point for the PEM harmonics.

Carefully filling the cell using a pipet constrains the sample for testing over the same temperature ranges. Utilizing the [BMIM][FeCl<sub>4</sub>] sample, with a dark brown hue, produced Figure 4.11 pulled from the lock-in amplifier voltage and phase readings.

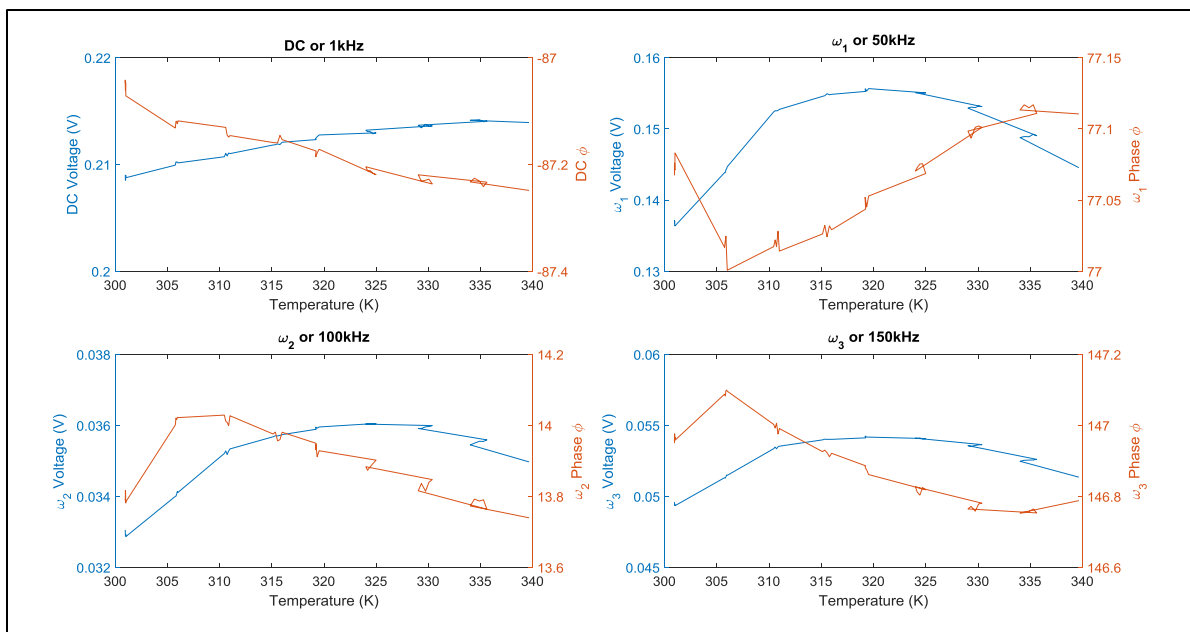


FIGURE 4.11 Voltage and phase of the Faraday rotation signal for a fused silica cell with [BMIM][FeCl<sub>4</sub>] vs. temperature

Once again, phase plays an important part in decoding rotation information and has minimal structure compared to the blank cell. The PEM frequencies again have a similar shape. Applying the sine function of the phase to the magnitude of the voltage unfolds Figure 4.11 to Figure 4.12.

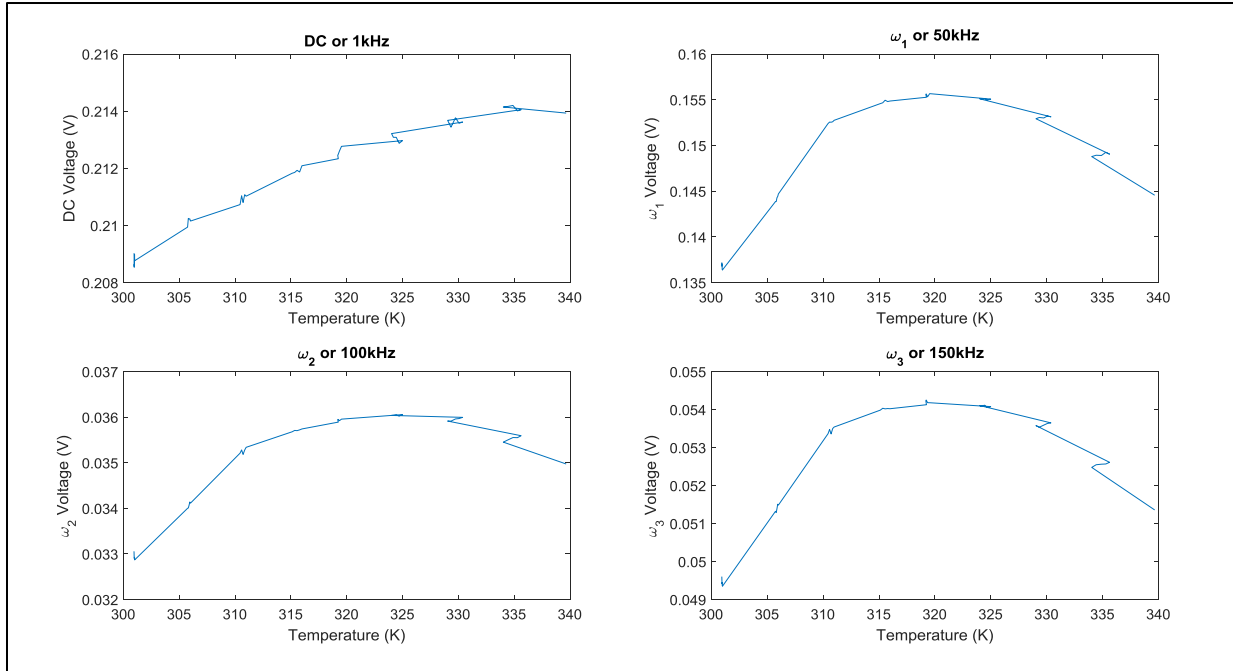


FIGURE 4.12 Phase corrected Faraday rotation signal for a fused silica cell with  $[\text{BMIM}][\text{FeCl}_4]$  vs. temperature

The above graph shows a slight power swing in the DC voltage opposite the direction observed in the blank cell scan. The slightly discontinuous graphs simplify to reveal constant rotation values for an applied 600mT field.

These graphs definitely indicate there is active properties of the material at the 600 mT field and the temperature swing has a slight impact on polarization. The full quantification of this impact comes when pulling out the rotation amount from each scan and taking a difference between the two. The difference in the two graphs should also be able to reveal the Verdet constant within the material.

### iii. Temperature dependence - hot end

The first scan of a blank cell shows how the fused silica glass sample behaves over temperature. Applying (3.43) derived in the methodology section with the above plot utilizing the DC voltage reading and second harmonic voltage gives the signal rotation in terms of  $\beta$ . The rotation graphs are Figures 4.13 and 4.14.

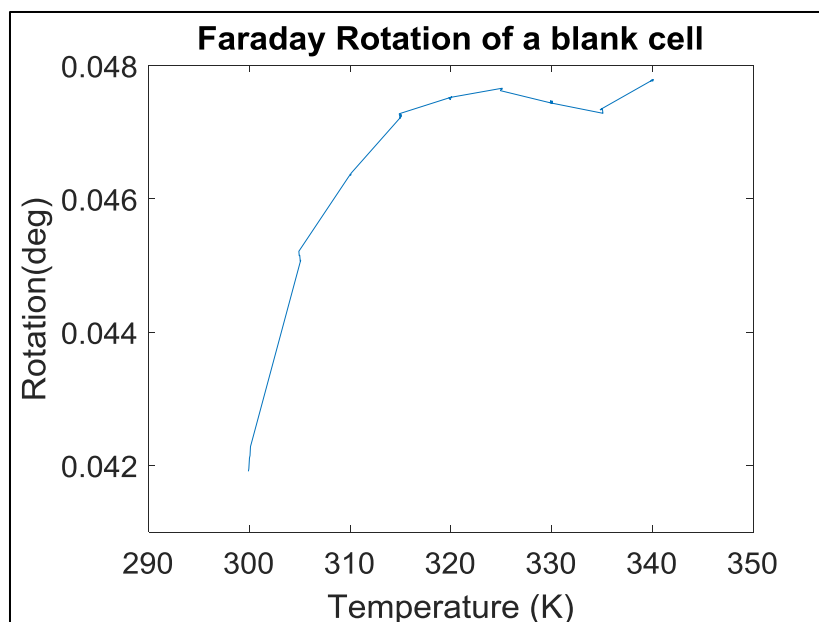


FIGURE 4.13 Rotation for a blank fused silica cell vs. temperature

After reaching temperature, the fused silica provided a total change in rotation of  $0.06^\circ$  over the  $40^\circ\text{K}$  temperature range. The magnitude of the rotation, measured to be  $0.042^\circ$ , which is slightly lower than the expected  $1.2^\circ$  calculated in the methodology section, although this was for a wavelength of  $578\text{nm}$ . This means the rotation extraction procedure and the test set up produce reasonable rotation numbers. Although for full validation additional tests need to be performed at different wavelengths to measure the Verdet constant variation over wavelength to properly scale the quoted constant to the measured one.

The next data to undergo the rotation calculation is the cell containing  $[\text{BMIM}][\text{FeCl}_4]$ . This measurement had higher noise, which becomes apparent at the higher temperatures. The deviation in rotation over the  $40^\circ\text{K}$  temperature range goes from  $0.0805^\circ$  to  $0.083^\circ$  rotation or a delta of  $0.002^\circ$ .

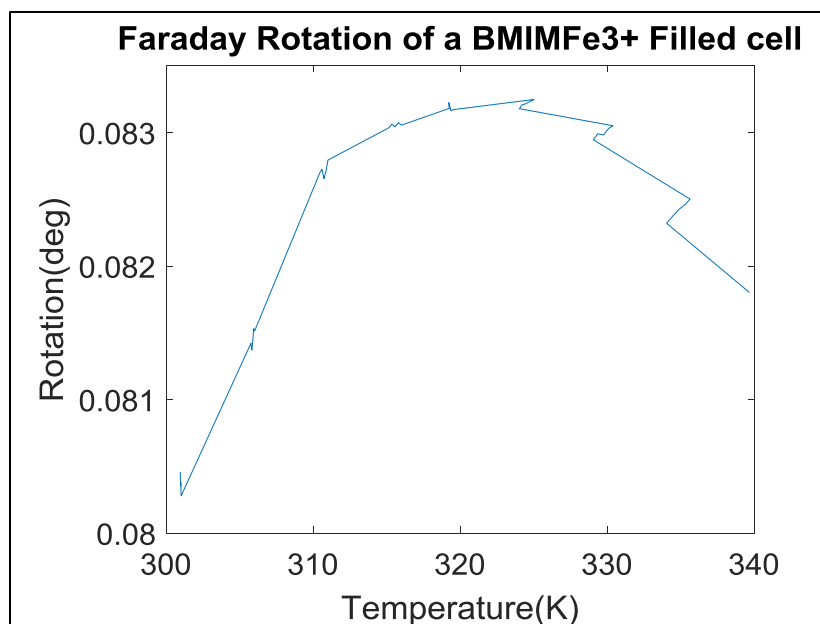


FIGURE 4.14 Rotation for a fused silica cell filled with [BMIM][FeCl<sub>4</sub>] vs. temperature

Taking the difference between these two sweeps yields the total rotation induced in the electric field polarization as a function of temperature. The average of the rotation was taken at each temperature and the resulting different was fitted to a 6-degree polynomial. Figure 4.15 is key result. This graph demonstrates how the ionic liquid magneto-optic material interacted with the signal light.

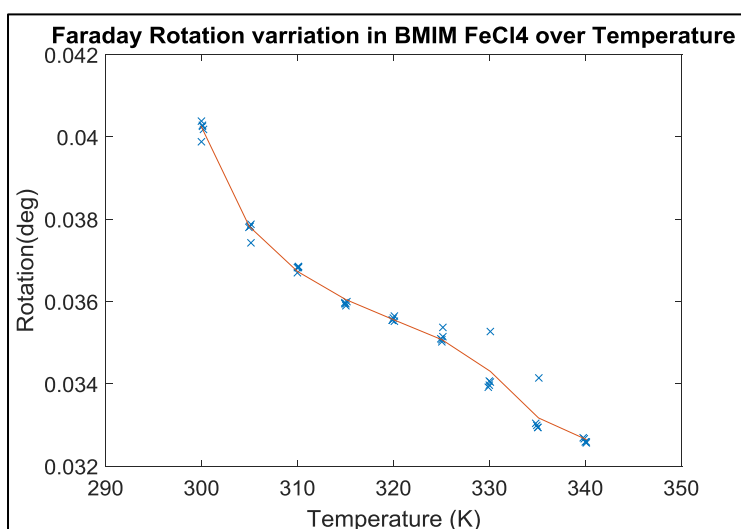


FIGURE 4.15 Extracted Faraday rotation for [BMIM][FeCl<sub>4</sub>] vs. temperature

Figure 4.15 indicates that the rotation of the material at a 600mT field is  $0.04^\circ$  at slightly higher than room temperature. Additional time should have been allotted for each temperature to stabilize the measurements, but with only one extraneous measurement per temperature the average of the data is fairly linear with a negative slope. The total temperature variation of the sample material over a 40K temperature range equates to  $0.007^\circ$  or  $0.000175^\circ/\text{K}$ , or approximately a 18% change.

#### iv. Temperature dependence - cold end

Complementary measurements were performed with temperature sweeps over a colder range of  $295^\circ\text{K}$  to  $5^\circ\text{K}$ . Performing these measurements required that a strong vacuum be pulled and that the chamber stage reach the desired temperature independently. A few test runs through this temperature range evidenced thermocouple issues, and it was necessary to spend an exponentially longer time at each temperature step resulting in only  $2^\circ\text{K}$  to  $135^\circ\text{K}$  being measured over a 3-day test.

Unfortunately, it was not possible to take meaningful data due to our inability to isolate the cell from the stage. This also was a result of the cells having to withstand high vacuum and tight temperature tolerances. Future work to improve this measurement procedure would be enabled by purchasing a stage designed for this environmental range and stage mount size.

#### v. Magnetic field dependence

The key measurement from this experiment comes from sweeping the magnetic field over  $-600\text{mT}$  to  $600\text{mT}$  to characterize the material response as a function of magnetic field strength. Figure 4.16 shows the baseline measurements for 1 kHz, 50 kHz, 100 kHz, and 150 kHz from left to right top to bottom.

A scan was first performed for the blank cell, verifying the background. The voltage as a function of magnetic field for a fused silica window is shown in Figure 4.16 and for the same four main frequencies as for the blank glass cell.

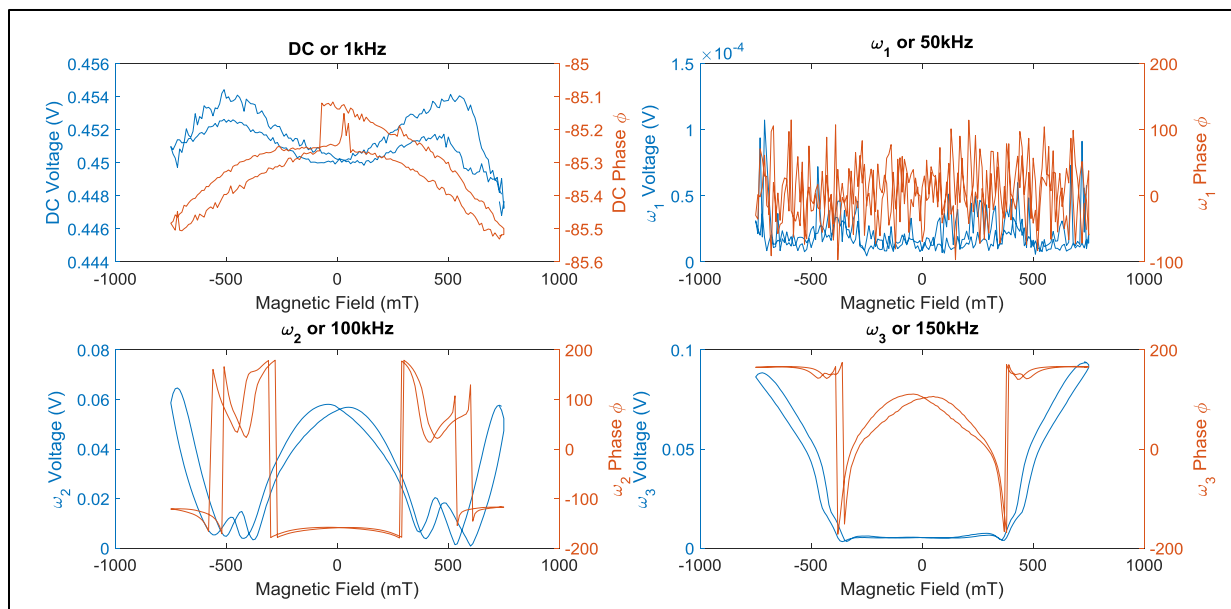


FIGURE 4.16 Faraday rotation signal vs. magnetic field for a blank fused silica cell

Again, the detected voltage is corrected using the phase information. The phase changes much more in this scan, as the phase goes negative so does the voltage and is strongly dependent on the change in magnetic field. Figure 4.17 shows the final corrected voltage plotted in blue, which is the detector voltage multiplied by the sign of the phase, plotted in orange.

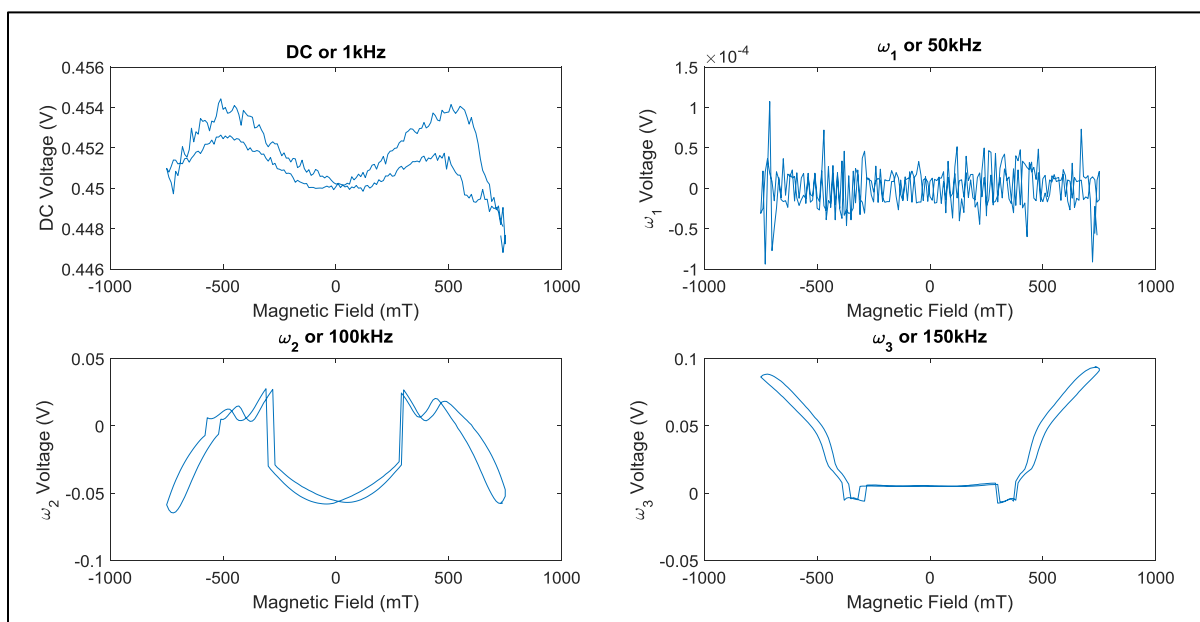


FIGURE 4.17 Phase corrected Faraday rotation signal for a blank fused silica cell vs. magnetic field

What immediately pops out about this graph compared to the uncorrected blank scan is the discontinuity in voltage for the 100kHz and 150kHz scans at 475mT. The voltage amplitude definitely changes as a result of the magnetic field directly correlating to rotation.

Next the material under test, [BMIM][FeCl<sub>4</sub>], is filled and sealed within the fused silica chamber. Raw voltage readings for the same frequencies in blue along with phase information in orange given below in Figure 4.18 demonstrates the Faraday rotation as a function of magnetic field.

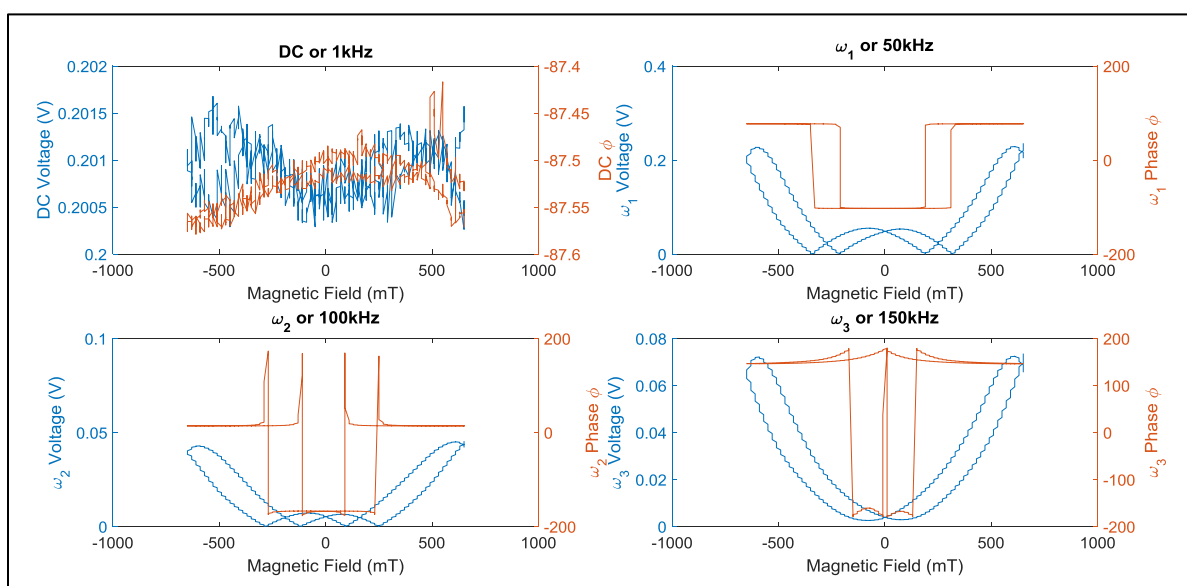


FIGURE 4.18 Phase and voltage for fused silica cell filled with [BMIM][FeCl<sub>4</sub>] vs. magnetic field

Corrected for the unwrapping of the phase, Figure 4.19 incorporates the signal information into a final amplitude.

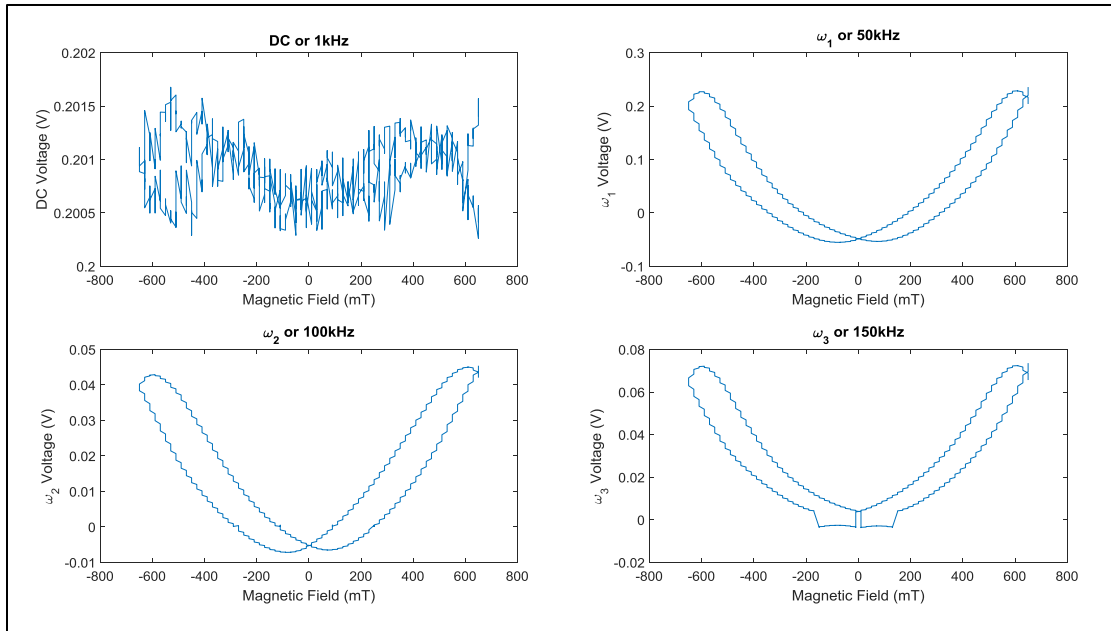


FIGURE 4.19 Corrected voltage for fused silica cell filled with  $[\text{BMIM}][\text{FeCl}_4]$  vs. magnetic field

Taking the baseline scan and subtracting the DC power and additionally removing the fused silica rotation will clean up the material rotation data. The signs are opposite in the two figures above showing that the material rotations are in opposing directions; i.e. their Verdet constants are opposite in sign. From the magnetic field sweep results, a few preliminary observations are extracted. The rotation is continuous based on the phase of the signal and amplitude of the magnetic field in addition to an offset in either direction of the rotation.

This hysteresis in the data is a function of the gyration vector. In regards to magneto-optic material equations with a static magnetic field the main concern is the electric field [Photonics]. Shown below in (4.1) is the material equation for the electric displacement  $D$  for an optically active medium.

$$D = \epsilon E + j\epsilon_0 G \times E \quad (4.1)$$

Where  $E$  is the optical electric field,  $\epsilon$  the permittivity, and  $G$  the gyration vector. This gyration vector is expanded below in (4.2).

$$G = \gamma B \quad (4.2)$$

The magneto-gyration coefficient is given by  $\gamma$  and  $B$  is the magnetic field density. (Photonics). From a quantum mechanical standpoint, the magnetic field applies a torque to the electron around the ion. The quantum spin of an electron is  $\bar{h}$ , where  $\bar{h}$  is Planck's constant. Therefore, the magnetic dipole moment becomes  $\frac{e\bar{h}}{2m}$  in units of  $A * m^2$  and is called the Bohr magneton, where  $m$  is the mass, and  $e$  is the electron charge. [Griffiths]. The Hamiltonian,  $H$ , of the spinning electron takes a scaled form of the spin matrices  $S$ , shown in (4.3) below.

$$H = -\gamma B \cdot S = \frac{\gamma B_0 \bar{h}}{2} \begin{pmatrix} 1 & 0 \\ 0 & -1 \end{pmatrix} \quad (4.3)$$

Since the Hamiltonian resembles the spin matrices, the eigenstates of the Hamiltonian yield up and down spin eigenstates. (4.3) indicates that the torque applied to the charged particles will depend on the field direction and the spin orientation. When the field is increasing, it acts on the electrons to increase the frequency of rotation, while when the field changes direction the rotation does as well, creating an offset through these transitions. [Griffiths]

#### vi. Magnetic field dependence - results

As mentioned above, a measurement on a blank cell provides the background information and fused silica characteristics over the measured magnetic field range. Understanding the glass contribution starts with knowing the Verdet constant for fused silica, a value given in Table 2.1. Shown below, a unit conversion of arc min to degree, (2.4), yields the constant in terms of the performed measurement.

$$V = 0.0166 \text{ (arcmin} * \text{gauss}^{-1} * \text{cm}^{-1}) \quad (4.4)$$

$$V = \frac{0.0166 \text{ arc min}}{\text{gauss} * \text{cm}} * \frac{1^\circ}{60 \text{ arc min}} = \frac{0.000277^\circ}{\text{gauss} * \text{cm}} \quad (4.5)$$

The anticipated rotation for a double pass through a 450 $\mu$ m path length for the two glass slides is given in (4.6)

$$Rotation = \frac{0.000277^\circ}{\text{gauss} * \text{cm}} * 2 * .0450\text{cm} = \frac{0.00002484^\circ}{\text{gauss}} \quad (4.6)$$

Using a conversion from earlier (2.3) helps transform the rotation into units applicable to the measured values in (4.7).

$$10,000 \text{ Gauss} = 1 \text{ Telsa} \quad (2.3)$$

$$Rotation = \frac{0.00002484}{\text{gauss}} * \frac{10000\text{gauss}}{1T} = \frac{0.2484}{T} = \frac{0.0002484}{mT} \quad (4.7)$$

Now solving the rotation for the tested magnetic field of 500mT yields the final rotation below in (4.8).

$$Rotation(500mT) = .1245deg \quad (4.8)$$

This is the expected measured fused silica contribution. The measured fused silica contribution is shown below in Figure 4.20 and the results can be compared to the measured values.

Now knowing what the expected fused silica contribution is, (3.48) used with each scans'  $\omega_{DC}$  and  $\omega_2$  voltage information yields the total rotation in degrees as a function of the applied magnetic field. Figure 4.20 demonstrates the total system Faraday rotation from both the fused silica cell and any background effects.

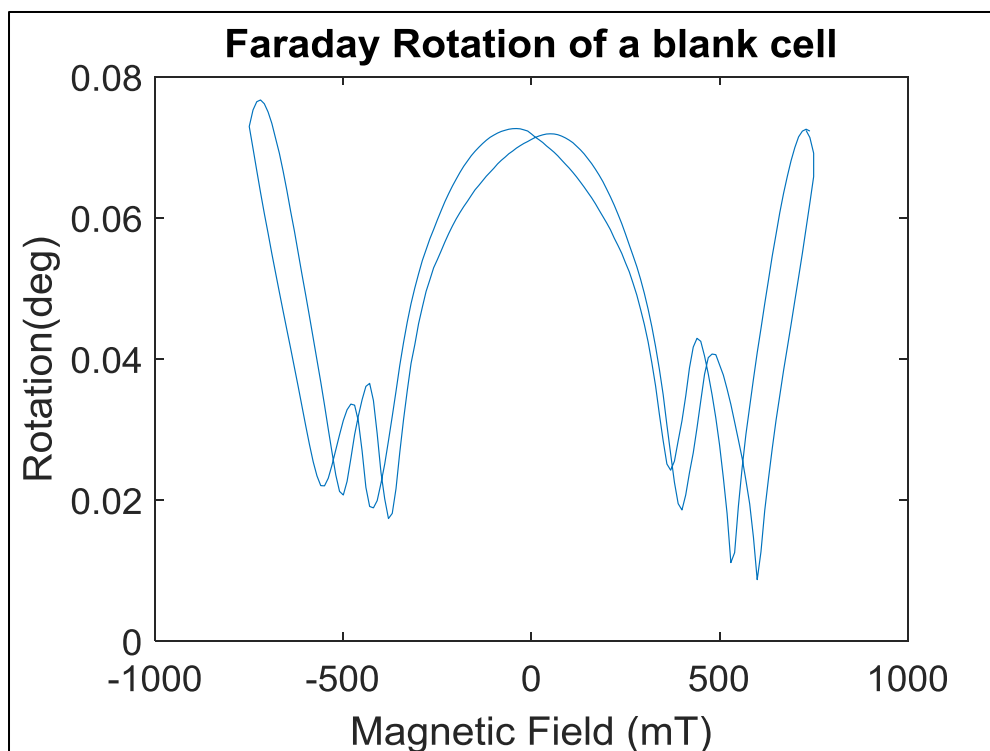


FIGURE 4.20 Faraday rotation for blank fused silica cell vs. applied magnetic field

The Faraday rotation has a clear dependence on magnetic field with its parabolic shape, although we were anticipating a linear dependence on magnetic field. Some offset occurred with no field being significant and nearly 0 at 500 mT. This data was not a pure measurement of the fused silica cell but more of a measurement of the background noise of the test set up and the cryostation. After the applying enough energy to excite the material the blank system reaches a total of 0.08 degrees rotation at +/-750mT. These numbers values must be subtracted from those measured for the sample under test.

Applying the same conversion from (3.48) the total rotation for a filled cell with [BMIM][FeCl<sub>4</sub>] is plotted in Figure 4.21. This shows the total system response, including contributions from the ionic liquid, the cell, and other effects.

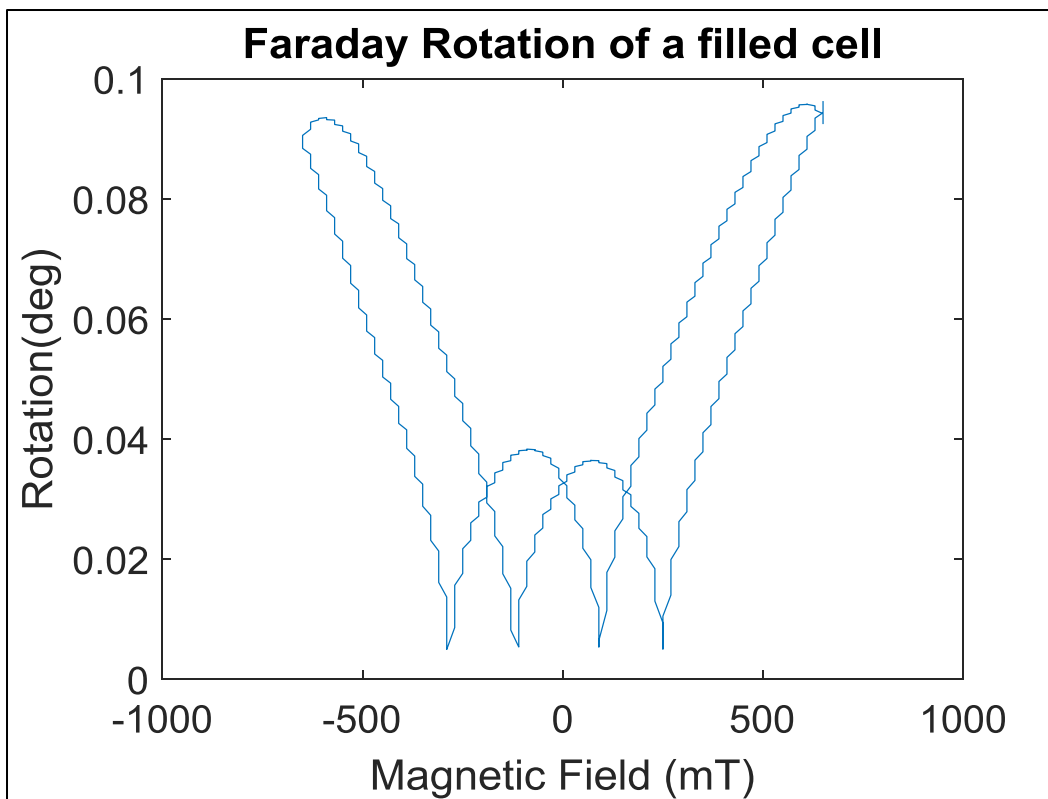


FIGURE 4.21 Extracted Faraday rotation for fused silica cell and [BMIM][FeCl<sub>4</sub>] vs. magnetic field

The shape is similar to the blank cell sweep but the magnetic field impact is more clear in the voltage increase with increase of magnetic field. A slight offset between the curves occurs as they circle back and forth and that is due to the magnetic spin of the electrons being rotated with the magnetic field. This specific event is attributed to the gyration vector explained in section 4. The rotation trend within the graph shows a direct correlation between the magnetic field and increase in rotation confirming the Faraday rotation within the system.

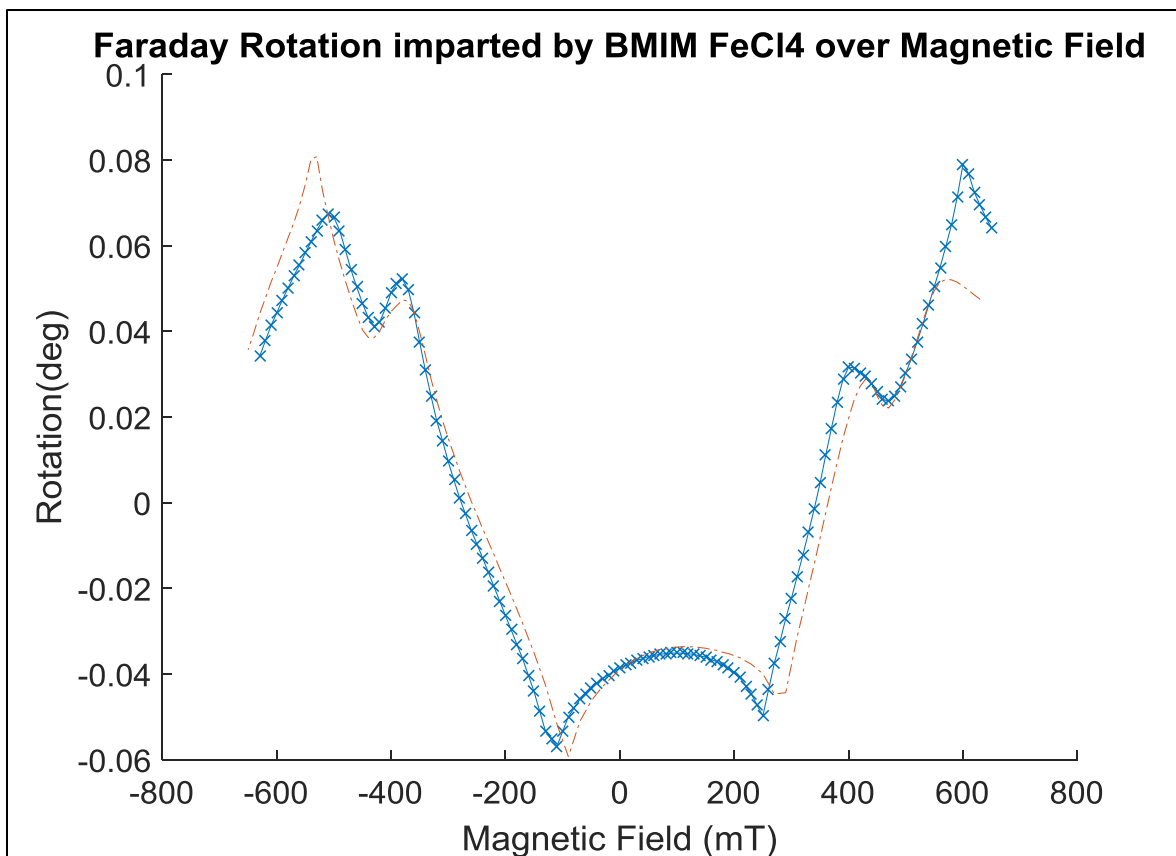


FIGURE 4.22 Extracted Faraday rotation for [BMIM][FeCl<sub>4</sub>] vs. magnetic field

Figure 4.22 demonstrates the difference between the background sample and the filled fused silica cell. Although slightly convoluted with the folding of the background sample graph, the Faraday rotation within the ionic liquid is significantly stronger than just the fused silica contribution. The magnitude of the rotation is much larger than expected with  $0.04^\circ$  rotation at 600mT. Extrapolating this to the LCOF length needed for a full  $45^\circ$  rotation at 600mT gives (4.9)

$$LCOF \text{ length} = 45^\circ * \frac{450\mu m}{0.04^\circ} = 50.6cm \quad (4.9)$$

There is still some noise present within these measurements. Now that the test set up has been characterized additional tests can be performed to test the reproducibility of these results.

Extrapolating this length to a hollow core fiber that is 10 $\mu$ m in diameter will reveal how much total ionic liquid volume is needed for each isolator in (4.10).

$$V = \pi r^2 * l = \pi * (5\mu m)^2 * 50.6cm \left( \frac{mL}{cm^3} \right) = 3.974 * 10^{-5} mL = 40nL \quad (4.10)$$

This total volume of material is incredibly small and is much less than the total amount needed to get the chain filled including all the losses. This miniscule volume demonstrates the manufacturing potential for this approach when the design is optimized.

### **c. LCOF Measurement**

#### **i. Creating the chains**

Creating the chains started by prepping the fibers for fusion splicing. Fusion splicing is a process that fuses together separate optical fibers to create one seamless interface with very low optical loss. Since the polymer coating on the fiber typically has a low decomposition point, it cannot withstand the electrode temperatures and therefore must be removed. Removing this material also create a clean surface for the cleave to strike and break the fiber lattice.

The hollow core fiber has a polyamide coating, a rigid structure with a dark brown hue. Because of the strong adhesion of this material to the fiber, manual removal of this coating must be done with a razor blade. Solvents cannot be used because using a strong enough solvent such as hydrofluoric acid or sulfuric acid would exposed the end of the fiber to the solvent for an extended time, and fused silica will dissolve in various acids.

After buffer removal, a small amount of methanol was used to clean off residual debris. This was a controlled amount of liquid used on a Kimwipe, but was necessary for protecting the cleaver blade from damage caused by particulates. Any amount of fiber potentially incurring solvent capillary action can be destroyed during the splicing process. Although a concern, the hollow core waveguide at the splice interfaces receives visual inspection on the splicer before splicing.

Some hollow core fiber loss occurred when removing the polyamide coating; this was due to the razor blade nicking the fiber causing it to break. For small-scale testing this was not a problem but for manufacturing becomes an issue to consider. This can be greatly minimized by utilizing a hot jacket stripper with a controlled blade diameter so as not to nick the fiber but successfully scrape the buffer off.

The standard fibers, PM 980 and HI1060 were cleaved with an ATF Power Cleave hand operated angle cleaver. Rotating the mount 10 degrees achieved a  $\sim 3\text{-}4^\circ$  angle on the fiber end face. Loading the fibers into the splicer manually, the onscreen image served as reference to adjust the fiber until both fiber ends were in view. Once the fibers were secured, a  $45^\circ$  mirror moved up between the fiber ends to image the surface of the cleave. Figure 4.23 shows the splice camera's view of the end face. Inspection is performed at this step to look at the potential for stress rod blowouts, cleaver indentation, and surface quality. Once verified to be acceptable, the mirror motor recedes and the fiber ends are moved together until they were  $\sim 3\text{-}5\ \mu\text{m}$  apart. To verify fiber spacing the fiber was stepped in  $1\ \mu\text{m}$  steps at a time, and as soon as the fibers touched, they were stepped back  $1\ \mu\text{m}$ . To account for the hysteresis within the stepping mechanism ( $\sim 2\ \mu\text{m}$ ), two additional reverse steps were included. The rotation was adjusted so the fibers were parallel to each other and in the same alignment when looking from both the front and back. Figure 4.23 shows the front and back view of a sample splice where the back-view stress rods align with the camera. The angle in PM 980 on the left is evident.



FIGURE 4.23 Sample splice viewed from front and back ( $90^\circ$  relative to each other)

Putting care into the splices, the delicate architecture required manual interaction in the splicing process. All the splice parameters were set manually depending on the fiber

position and electrode stability. The electrode stability and power were tailored for the temperature and humidity in the room from repeated calibration.

The power used for the arc electrodes varied from 14W up to 17 W and depended on the amount of curing and melt depth seen at the edge of the fiber. The electrodes were heated up over the fiber ends before moving the fibers together. Moving the fibers together is called the hot push and was controlled by time and distance. The total electrode time influenced the curvature of the fiber edge and the final silica temperature.

An image of the two fibers before and after the fusion arc is shown below (Figure 4.24) with a sample splice-using an electrode power of 15.9W on for 750 milliseconds and moving 4 $\mu$ m in the last 460 milliseconds.

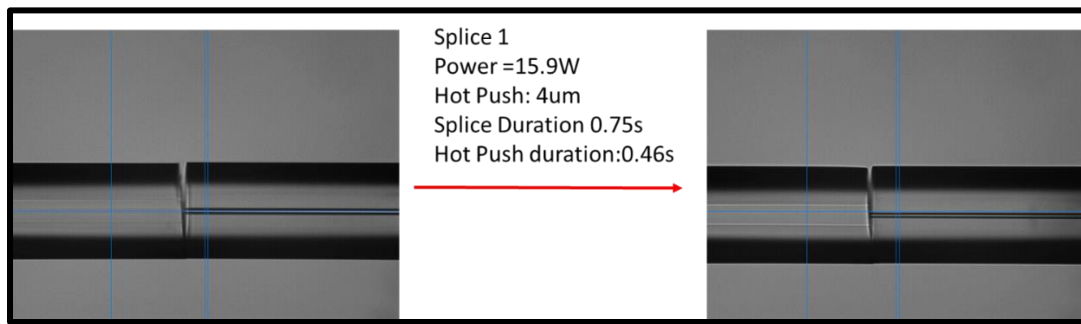


FIGURE 4.24 Fibers before and after splicing using a 15.9W electrode arc

The difficult part of the process was not the splice however, it was what came after the splice. The process of cleaving a fiber is based off the intermolecular forces that keep the lattice structure of the fiber together. Releasing this energy by breaking the bonds supporting this structure creates a fracture propagating along the crystalline plane. Since these splices were designed to only fuse 50-60% of the total diameter for filling purposes, a clear fracture line remained after the splice making the joint very fragile. The fragility resulted in only a handful of chains being created. A table of LCOF chain inventory below records the testing parameters and logs tested chains. It should be noted that due to physical size constraints of the solenoid, some of the vial caps necessary to house the liquid did not fit within the solenoid opening. Other primary issues included damage to the end face cleave of the HI1060 potentially distorting the signal propagation.

Chain Number	Chain Length	Hollow Core diameter (um)	Filled with	Notes
1	13	5	Fe	
2	13.5	5	Fe	
3	18.5	5	Fe	Broke at PM980 splice
4	9.5	5	Fe	Broke at HI1060 splice
5	30	5	Fe	Too big to fit in solenoid
6	30	5	Fe	
7	30	2	Not filled	

TABLE 4.3 Testable chains made during testing

It should be noted that only a handful of chains were made; the fiber parameter trade space needs to be fully mapped, but only after improving the build process which will be explained in more depth in the future work Section 5.

An interesting calculation examines the material index required to achieve a single mode beam at the test wavelengths. Single mode fiber has a V parameter value of 2.406 or less. Taking this and solving for the subsequent NA, a relationship for lambda emerges in (4.11).

$$NA = \frac{V \lambda_0}{2\pi r} = \frac{2.406}{2\pi} \frac{\lambda_0}{(2.5\mu m)} = 0.153171 * \lambda_0(\mu m) \quad (4.11)$$

Plugging in the NA from (4.11) into (4.12) and solving for required core index  $n_2$  in terms of the fused silica fiber index gives a formula to determine ideal index for single mode operation. (4.11) determines index needed for single mode found for various diameters and wavelengths potentially utilized in the set up. Starting with (2.12) the numerical aperture is expanded below in (4.12) to be put in terms of refractive index.

$$NA = n \sin(\theta_c) = \sqrt{n_1^2 - n_2^2} \cong n_1 \sqrt{\frac{2(n_1 - n_2)}{n_1}} \quad (4.12)$$

$$n_1 = \sqrt{n_2^2 + (NA)^2} = \sqrt{(n_{FusedSilica}(\lambda_0))^2 + (NA(\lambda_0))^2} \quad (4.13)$$

Using the wavelength specific fused silica indices determined in Table 2.3 and (4.12) the maximum index for single mode operation is given in Table 4.4. Also as a sanity check, the NA of the fibers for the various core size can be compared to the input and output fibers standard NA.

$\lambda$ (nm)	SM NA(2 $\mu$ m)	$n_2$ (2 $\mu$ m)	SM NA(5 $\mu$ m)	$n_2$ (5 $\mu$ m)	SM NA(10 $\mu$ m)	$n_2$ (10 $\mu$ m)
980	0.3753	1.4985	0.1502	1.4585	0.0751	1.4526
1060	0.4059	1.5053	0.1623	1.4587	0.0812	1.4519
1310	0.5016	1.5312	0.2006	1.4605	0.1003	1.4502
1550	0.5935	1.5612	0.2374	1.4634	0.1187	1.4489

TABLE 4.4 Material index for single mode NA and fiber core size

Keeping in mind the following fibers NA and how it matches to the hollow core fiber influences the single mode quality of the beam. Also, if  $n_2$  is larger than the fused silica then the light will not guide. Considering a 2 $\mu$ m core which allows for the highest refractive index achieves single mode quality for a large acceptance angle or NA of up to 0.37 or 21.5° at 2 $\mu$ m. This specification cannot be met by the HI 1060 fiber causing attenuation in the final signal. Optimally for integration with a telecom standard fiber the 5 $\mu$ m core will be the best option with an NA of 0.09 to 0.12.

A measure of the material refractive indices would be useful here for verification of single mode operation for the tested core size. This was never confirmed and should be considered as one of the key next steps.

## ii. Filling the chains

Filling the chains relied mainly on a capillary action process. An amalgamation of surface tension and intermolecular forces, capillary action moves the liquid up the narrow tube against other forces such as friction or gravity. One conversion factor to note is that  $0.001m^3$  equals 1 liter.

$$V_{tube} = \pi(r^2)l = \pi(2.5\mu m)^2(30cm) = 5.89 * 10^{-12}m^3 = 5.89 * 10^{-9}L \quad (4.14)$$

To increase the rate of filling, a programmable syringe pump, from New Era, plus a heater lowered the viscosity, thus speeding up the rate of filling. A fine motor stepper, slowly pushed the syringe pump in at a rate of  $0.73\mu L/hr$ , filling the volume of the fiber in  $\sim 30$  seconds if the system is properly sealed and the optical path is free of debris. To better view the filling, the liquid core was illuminated by a red LED coupled into a standard multimode cable for an inspection of the flow. Unfortunately, owing to high absorption it was difficult to inspect visually the filling along the full length of the hollow core.

## iii. Beam imaging

A  $\mu$ eye camera system from Thorlabs images the fiber face back through the collimator by way of a foldable mirror. Adjusting the image until it is in focus verifies the collimation and provides views of the quality of the fiber surface.

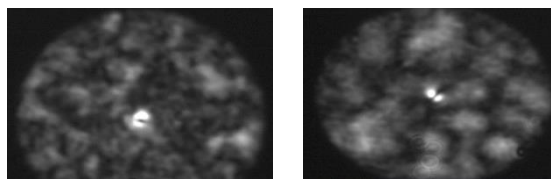


FIGURE 4.25 Beam images from the LCOF test setup

The output fiber utilized is a HI1060, a non-PM fiber, which is intended to capture the beam and leave it un-manipulated for accurate rotation information. Additionally, the fiber was cleaved post liquid filing to best protect the surface. From the image multimode

properties, shown in Figure 4.25, are two white lobes straddling a null in the center of the core.

These images show a lot of higher order light in the core and scattered at the end face. This variation in the intensity of light most likely was due to the interaction of the higher order modes coupled in from the material under test to the HI1060 fiber. Furthermore, with the testing environment was filled with air particulates, and the fiber face could have been contaminated. The fiber was cleaned but due to the fragility of the system couldn't be fully inspected under a microscope. With a limited number of samples only a few fiber images were taken/ improving the process and creating a more stable chain will allow easier inspection of the fiber end.

#### iv. Magnetic field within the solenoid

The measured parameters for the solenoid are given below. For the dimensions of the circumference, outer and inner diameter, the measured values were 42.8cm, 13.5cm, and 2cm, respectively. The magnetic field inside the solenoid was measured with a gaussmeter and the results are shown in Figure 4.26.

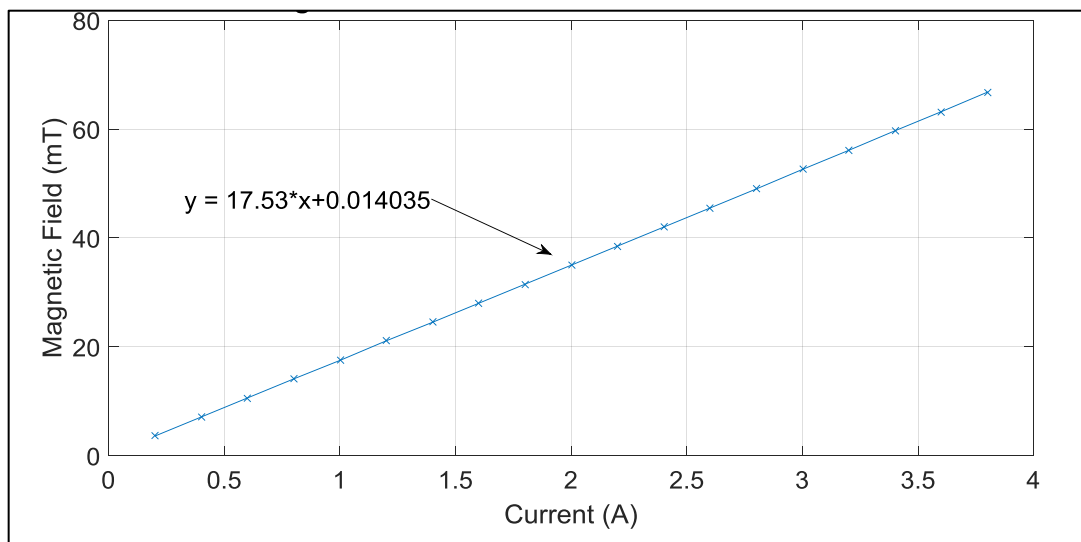


FIGURE 4.26 Magnetic field within the test setup solenoid

Comparing the measured solenoid results above with the expected calculated field value in the methodology section reveal similar values. The anticipated field dependence on current is given below from (3.49).

$$B = 16.764 * I_0 \text{ mT/A} \quad (3.49)$$

Extracting a liner slope fit from the measured results yielded a slope of 17.53 mT/A, a y offset of 0.014mT and a normalization of  $r= 0.34141$ . The results have a deviation of -0.766mT from the theoretical value and a percent deviation of -4.6% from the theoretical value; both of these values are calculated below in (4.15) and (4.16).

$$\text{Deviation} = \text{Theroetical} - \text{Experimental} = \frac{16.764\text{mT}}{A} - \frac{17.53\text{mT}}{A} = -\frac{0.766\text{mT}}{A} \quad (4.15)$$

$$\% \text{ Deviation} = \frac{\text{Theroetical} - \text{Experimental}}{\text{Theroetical}} * 100\% = \frac{-0.766}{16.764} * 100\% = -4.57\% \quad (4.16)$$

Some of this discrepancy can be attributed to errors in current measurements and errors in the counting of loops, but proves the measured field to be consistent with expectations and validates the field within the solenoid.

#### v. LCOF results

The power out of the diode through the paddles and out of the polarizer was measured to experience an insertion loss of 0.85 dB. The output power captured by the detector was recorded as a function of rotation angle. The LabVIEW code used to drive the rotating analyzers also output a text file of detector voltage versus rotation angle. Plotting the two yields a sinusoidal intensity for purely linearly polarized incident light. The test schematic from Figure 3. 11 below puts the data in context.

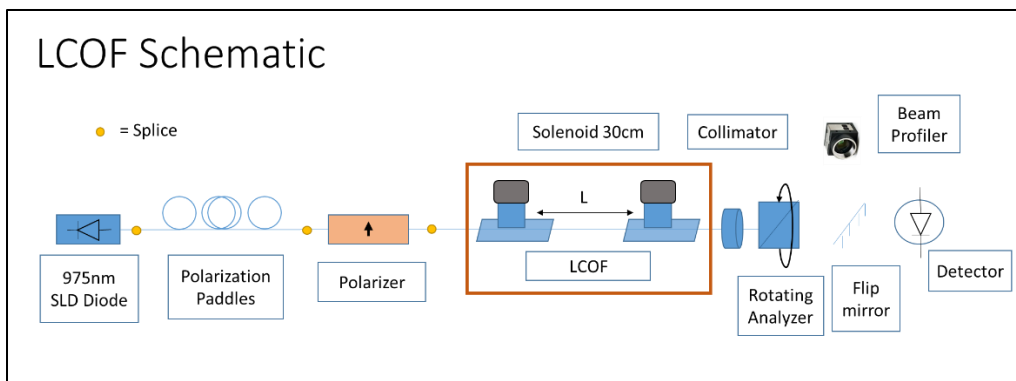


FIGURE 3.11 Liquid core optical fiber test schematic

The first tested chain length stretched 13.5 cm and was filled with  $[\text{BMIM}][\text{FeCl}_4]$ . The output HI1060 fiber is flat cleaved as close as possible to the hollow core using an angle cleaver in reverse. The left-hand plot in Figure 4.27 gives the measured detector voltage for light emerging from the LCOF as a function of rotation angle. The right hand plot correlated temperature in arbitrary units to rotation angle. Scans taken for a baseline of 0V plus scans at +5 amps and -5 amps yield a full dynamic range of 10A.

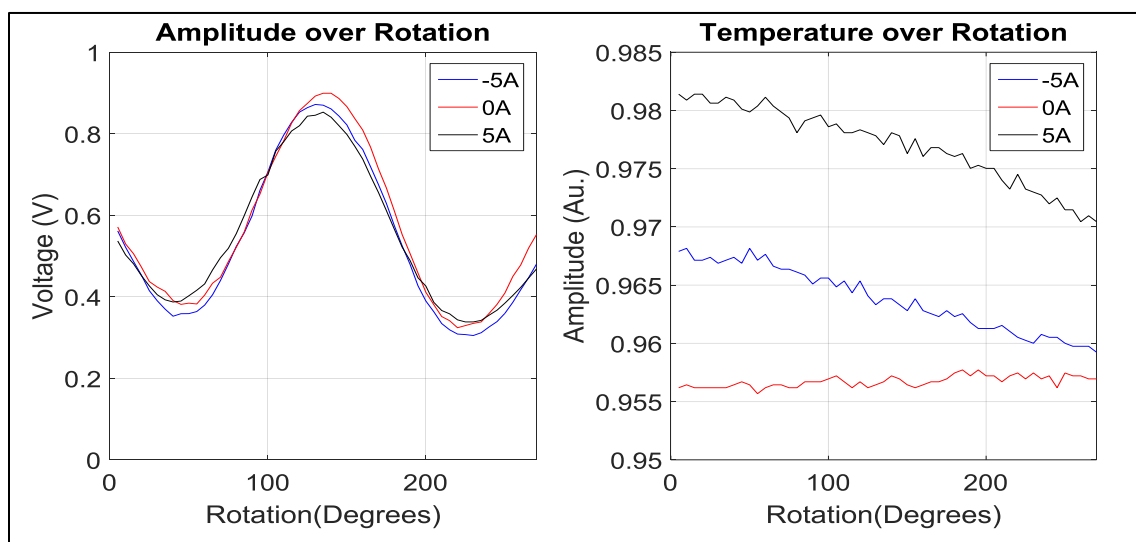


FIGURE 4.27 Chain sample 1: length 13cm, power and temperature as a function of rotation angle with 0, +/-5 amps through the solenoid

If there is Faraday rotation occurring within the material, then there is expected to be a phase shift in the intensity plot. When the active medium is excited it rotates the  $E_x$

and  $E_y$  orientation, and thus the polarization about the optical axis. A shift is noticeable in both the scans with magnetic field applied, compared to the baseline 0 amp run.

The temperature within the solenoid is recorded at every step along the scan for observation of general trends. With the 0A test, no heating is observed but with an applied current of +/-5A there was a change equating to a 2.93% variance.

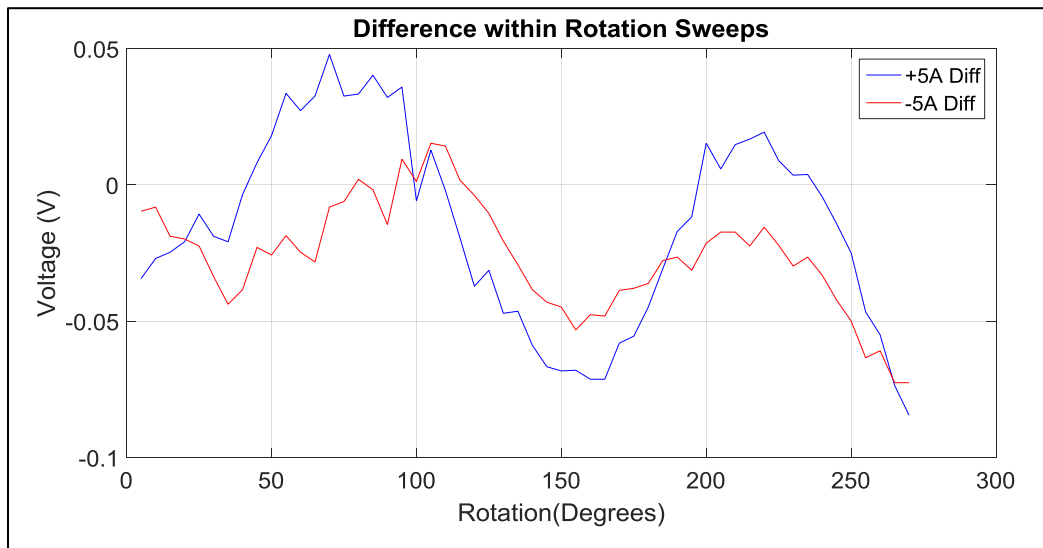


FIGURE 4.28 Chain sample 1 scan differences as a function of rotation angle

Figure 4.28 demonstrates the direct difference between the polarizer transfer function for magnetic fields applied in opposite directions. The sinusoidal shape is expected from Malus's law. A clear shift in the maximum is observed in the 50-100° range, although this does not appear to be the case at 225°

Taking the Fourier transform of each signal uses the sample set, taken over a sinusoidal period and transforms them into frequencies. The transforms of the scans are plotted below in Figure 4.29.

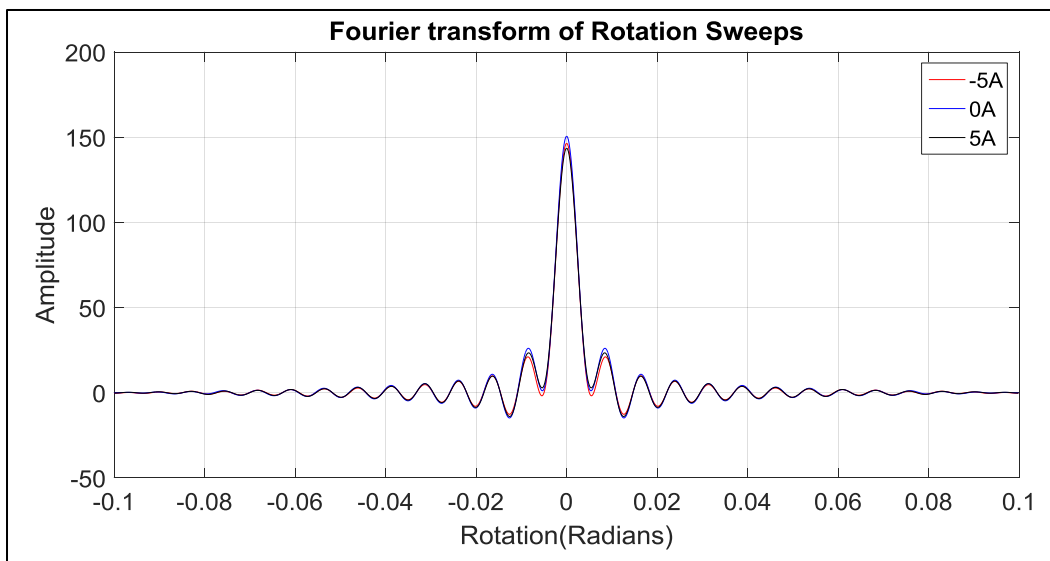


FIGURE 4.29 Chain sample 1 Fourier transform of rotation sweeps

All of the Fourier transforms have similar shapes which is ideal because the light should be oscillating in amplitude at the same frequency regardless of the current applied. This transform relates the periodicity of the analyzer in a form of a transfer function. The real differences between these graphs appears in the amplitude. The baseline scan has the largest intensity while for the scans with field applied the power is slightly more spread out.

To find the phase difference the angles of each of these transforms needs to be taken. The difference in the applied field scan angles and the baseline scan angle will then result in the phase difference between each scan. The direct amplitude difference between the Fourier transform scans are demonstrated in Figure 4.30 below.

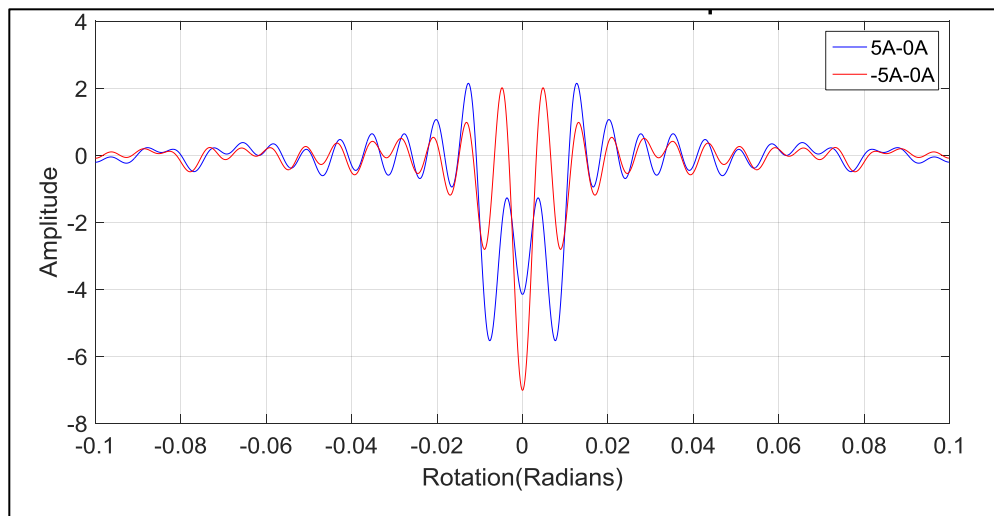


FIGURE 4.30 Chain sample 1 difference in Fourier transform of rotation sweeps

The second chain tested, Chain 2, was tested for a baseline 0 amps and two scans of increasing solenoid current of 3 amps and 5 amps. This now demonstrates the scaling increase in rotation in a single field rotation direction, meaning the current is only applied through the solenoid unidirectionally. Figure 4.31 below plots the voltage and temperature probe current as a function of rotation angle.

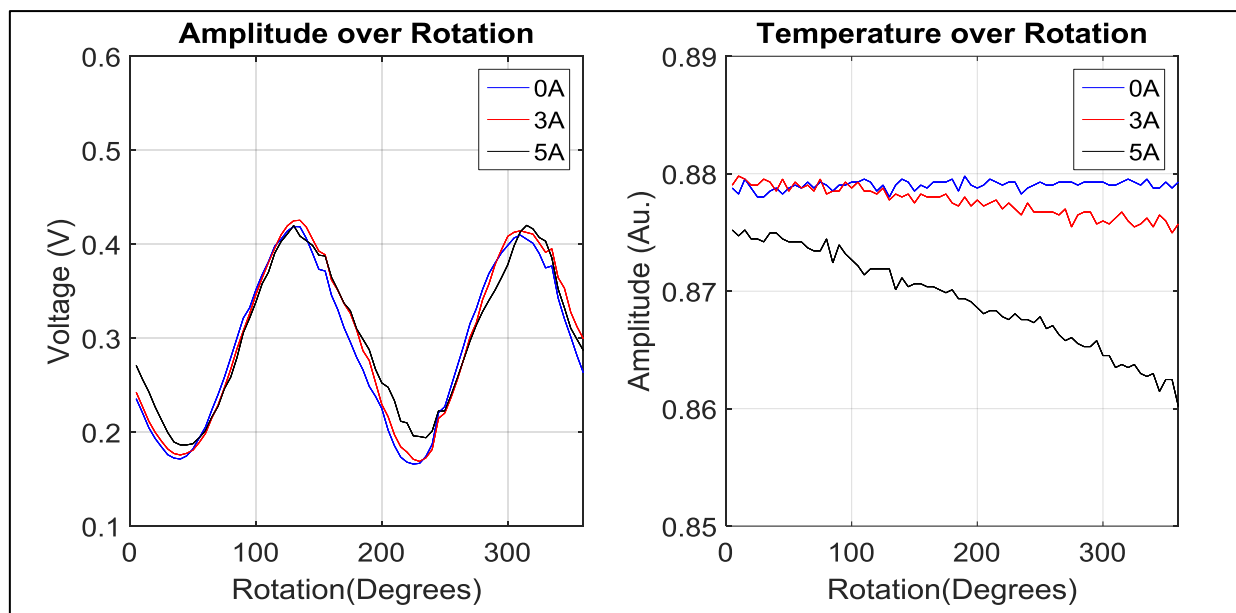


FIGURE 4.31 Chain sample 2: length 13.5cm, power and temperature as a function of rotation angle with 0, 3, and 5 amps through the solenoid

A more significant shift in curves appears in the 5 amps' curve as compared to the baseline. The temperature shift between scans decreased slightly at a 2.27% variation in temperature.

Again the difference between the two active graphs and the baseline is shown below in Figure 4.32. Note the slight shift in curves as the field strength increases.

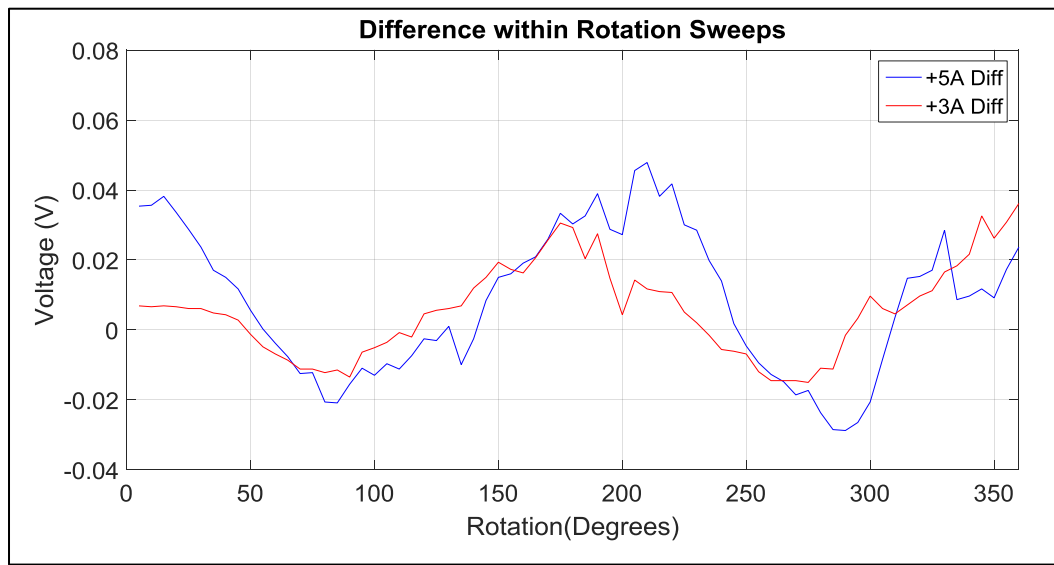


FIGURE 4.32 Chain sample 2 scan differences as a function of rotation angle

The three scans were padded with zeros, for increased sampling rate, and then transformed to yield the frequency information. Figure 4.33 closely resembles figure 4.C.5.3 although with slightly different amplitudes. The baseline running ~50% larger than the graph below.

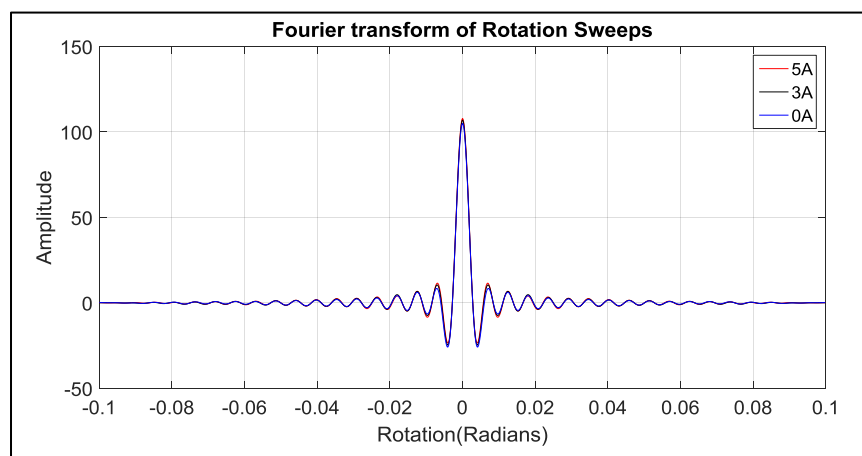


FIGURE 4.33 Chain sample 2 Fourier transform of rotation sweeps

The baseline has less power in the central peak than the active scans which is inverse to the other transforms. The relative power between the active scans and baseline again was taken and is plotted below in Figure 4.34.

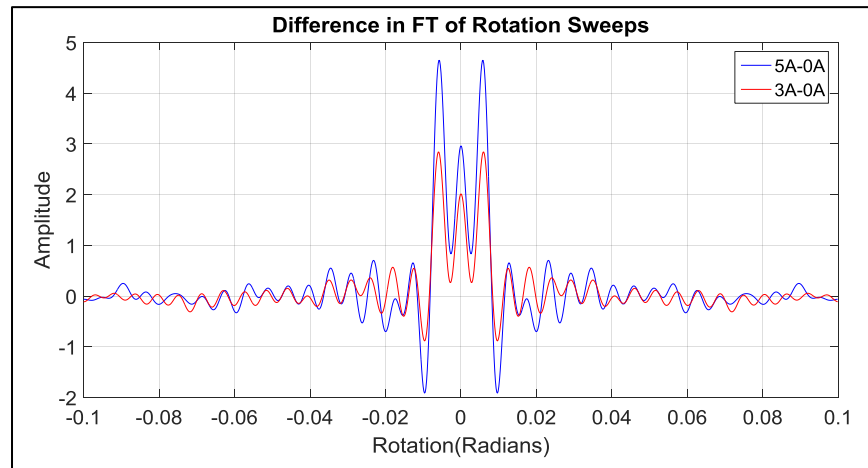


FIGURE 4.34 Chain sample 2 difference in Fourier transform of rotation sweeps

The relation between the two transforms is clearer than with the opposing current scans. A clear power increase is observed between the 5A scan as compared to the 3A scan. Again the angle of each scan should be taken and compared to each other.

Although no clear rotation was observed in the test set up a few key components can be changed to reduce the noise in the system. Additionally, more chains need to be created for a wider range of sampling.

## **V. Discussion of future work**

Paving the way for multiple ventures the tests outlined in this paper lay the framework for testing and verification of an in line LCOF isolator. With vast opportunities of avenues left to explore, the next points outline the key next steps in testing. Some of these topics were touched on earlier in this thesis but are discussed in more depth.

### **a. Faraday rotation**

The Faraday rotation set up was unsuccessful in completing a cold temperature sweep because of the inability to fully isolate the sample from the cryostation chamber. Additionally, the scribed glass cells struggled to maintain their integrity under the strong vacuum. However, a solution is to use a new liquid chamber designed to withstand the thermal and vacuum environments. This testing is important because it examines two types of cold cycling, applying a field before or after the liquid solidifies. This will expose how the rotation acts when the liquid freezes and demonstrate if the rotation is controllable at low temperatures.

One main benefit with using the cryostation chamber is the 2-3 hour cool down period after filling the cell and mounting and the warm up and testing period takes up to a day to perform. Thankfully, due to the closed loop system there are minimal facilities obligations or coolant waste from running this test.

Because this is the baseline measurement for Faraday rotation properties, other materials can be tested along the same fashion. Key ions to consider include the erbium liquid tested for its material properties in the line of this experimentation. The liquid options do not stop there: almost any ion can be suspended within the BMIM structure, element size permitting. Ideal ions to try are nickel and cobalt ions which have previously been fabricated in ionic solutions. They take the form of [BMIM][Ni(DMIT)<sub>2</sub>]<sub>3</sub> or BMIM nickel 1,3-dithiol-2-thione-4,5-dithiolate [Synthesis materials] and [BMIM][Co(CO)<sub>4</sub>] or BMIM cobalt tetra-carbonyl a catalytically active organometallic ionic liquid [Chemical Communications]. Another set of ions that produce interesting interactions in fiber and would provide key transitions are the combination of erbium and ytterbium. Integrating

these elements into a supported structure is the next step in opening up the options for filling liquids.

To fully characterize the material the number/list of tests required include: a baseline measurement, scan of the fused silica cell, a filled cell with the rotation on while cooling, and a filled cell with the rotation off while cooling. After each of these scans, the sample chamber needs to undergo a physical inspection to ensure the integrity of the cell is intact.

## **b. LCOF chains**

The next major testing considerations is completing an in line fiber isolator. This is easily possible through process improvements in chain construction and filling. The chain construction can be expedited through use of fiber strippers, such as microelectronics, that are a set fiber diameters to eliminate hollow core fiber waste. A splice optimization consisting of at least 12 trials for each splice parameter to form a statistically significant set will then enable use of an automatic program to create the special splice. Finally, a stable mechanical mount to transfer the splice from the electrodes to a mounted microscope slide will drastically improve yield of splices to final chain systems. This testing requires a large sample set so many samples of varying lengths need to be created for testing.

Additionally, one main set up problem was the visible attenuation in the ionic liquid was so high coupling in a low power LED to illuminate the filling was nearly impossible to see. A higher power visible laser fiber coupled and spliced into the chain during filling is needed to illuminate the liquid as it wicks down the fiber. A class 4 fiber coupled HeNe laser would suffice.

Once the construction is simplified, it will enable easier testing of different ionic materials. Testing the optical properties in addition to the Faraday rotation measurements means the best performing liquids can be selected for a given application and tailored to have ideal physical properties (viscosity, transition temperatures, transmission, ...).

A final set up variation includes other key telecommunication wavelengths such as the low dispersion wavelength of 1310nm. The components needing replacement include the FC in-line fiber polarizer for transmission at  $1310 \pm 50$  nm, a FC/PC PM/PM Pigtail [ILP1310PM] and the main seed source to a 1310nm diode [1310 diode] The basic schematic would remain the same as in Figure 3.11.

Additionally, by changing the wavelength the rotation measurement can be better controlled by introducing a 90/10 splitter. These splitters, typically based off evanescent wave coupling, sample the forward and reverse power. By splicing the LCOF end face to a retro-reflector the rotation of the material under test can be measured from the 10% return tap. Figure 5.1 demonstrates the 1310nm set up with a 90/10 splitter for diagnostics.

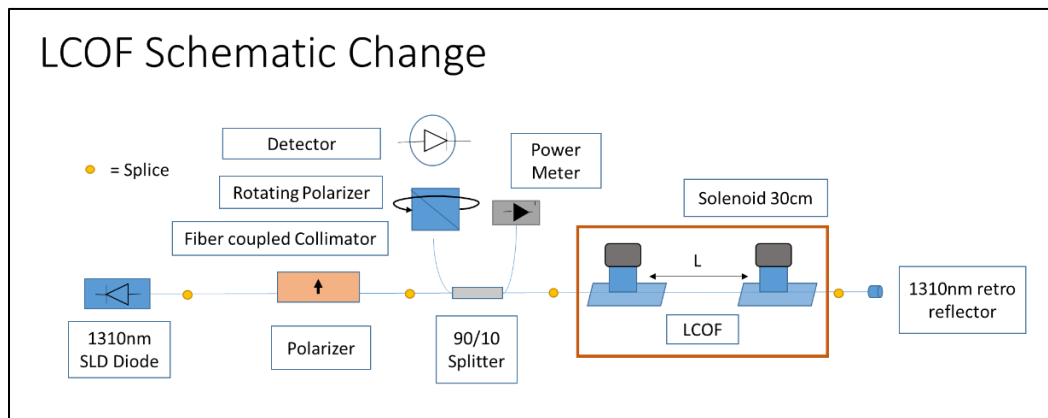


FIGURE 5.1 LCOF measurement schematic change

Instead of relying on aligning an extremely variable free space optics system every time for each new chain under test the light gets coupled down a diagnostics path once from an easy to cleave COTS fiber. This drastically reduces times between testing samples. This is considered for testing at 1310nm due to the parts on hand but this system can be converted to any wavelength, with a new seed, reflector and detector, as long as there is transmission through the rotating polarizer.

### c. Isolation measurement

Once an ideal length of material is verified to achieve 45° rotation, the isolator needs to be spliced in the reverse direction and then a measurement is performed of the amount of power that is transmitted in the same polarization. This measurement variation is simple. Once a sample of the correct length is created it needs to be tested in a specific order, due to the destructive procedures performed on the chain structure during testing. The testing is destructive because one sample needs to be cleaved at a short length to verify the rotation directly out of the chain. Therefore, testing full integration between two fiber polarizers must be done first, because a second fiber component requires enough length to reach a splicer and fuse the waveguides together.

Simply splicing in the isolator in the reverse direction and sending the output through a linear polarizer while applying the correct field should extinguish all the forward propagating light. The ratio of incoming light to throughput in a log scale gives isolation in dB from (2.6). This number is a key measurement for any isolator system.

$$Isolation[dB] = 10 * \log_{10} \left( \frac{Power\ In}{Power\ Out} \right) \quad (2.6)$$

To have a viable system that is realistically suited for commercial application, the isolation needs to show numbers in the high 20dB range. This includes some buffer for material and system standardization and refinement to reach the 30dB standard or the low SNR standard of 50dB which is typically used for RF applications.

#### **d. Other material exploration**

##### **i. NMR**

Other material verification that should be explored includes FTIR and NMR. These are easy enough tests to perform. Resources are available to perform both tests in the chemistry building on a pay per use basis. The nuclear magnetic resonance imaging, NMR, will reveal the magnetic properties of the electrons and nuclei at certain magnetic resonances. The spectrum helps reveal the chemical structure, which is known, but also the exact resonances of the molecule within each sample. Typically done to confirm purity

of a final sample in the synthesis process, this test takes less than 15 min to perform. The FTIR test or Fourier transform infrared spectroscopy utilizes an infrared source to extract the sample's absorption and emission spectra in infrared. This reveals a more detailed picture of how each material will react at given signal wavelength.

## ii. FTIR

A key property of any optical material is the refractive index. Typical refractive index measurements include using an Abbe refractometer, but are limited in the wavelengths available. One expensive but straightforward way to extract the refractive index is by having a termination on the fiber at a given angle, the end then can be submerged in oils of varying index. This requires many precision controlled oil samples and the accuracy is limited to the refractive index resolution between samples.

The next best option is to utilize Fresnel reflection loss parameters to extract the index, capturing the small amount of reflected power while monitoring forward power using a directional coupler. The ratio of forward and returned power coupled with Snell's law give the inputs to use the Fresnel reflection equation below to determine the material's index when submerging the fiber end in various oils with known refractive index. Also making the assumption that the electric field is parallel to the plane of incidence, the wave interaction down the fiber resembles Figure 5.2.

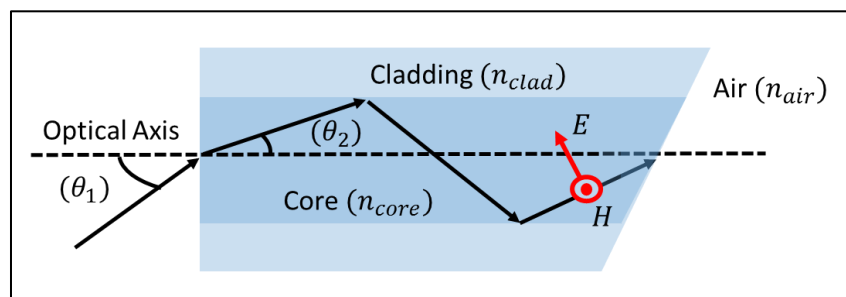


FIGURE 5.2 Fiber schematic for Fresnel reflection loss

Transmission in the form of  $T$  is measured out from the end of the fiber. There is a tap measuring forward and reverse power. Knowing this for a difference in controlled

reflection angle will yield information about the refractive index starting with the equation below [Hecht].

$$r_{\parallel} = \frac{\tan(\theta_i - \theta_t)}{\tan(\theta_i + \theta_t)} \therefore R_{\parallel} = \frac{\tan^2(\theta_i - \theta_t)}{\tan^2(\theta_i + \theta_t)} \quad (5.1)$$

$$t_{\parallel} = \frac{2 \sin(\theta_t) \cos(\theta_i)}{\sin(\theta_i - \theta_t) \cos(\theta_i - \theta_t)} \therefore T_{\parallel} = \frac{4 \sin^2(\theta_t) \cos^2(\theta_i)}{\sin^2(\theta_i - \theta_t) \cos^2(\theta_i - \theta_t)} \quad (5.2)$$

$$R_{\parallel} + T_{\parallel} = 1 \quad (5.3)$$

Now looking at the refractive indices of the setup when varying the termination of the fiber into known index oils Snell's law can be applied, (2.10). Setting the angles in (5.4) will then allow us to extract the fluid index.

$$n_1 \sin(\theta_1) = n_2 \sin(\theta_2) \quad (2.10)$$

$$\text{Where } \theta_1 = \theta_i \text{ and } \theta_2 = \theta_t \quad (5.4)$$

Although not explored in the current study, this measurement should be considered in the next steps. Figure 5.3 below demonstrates the schematic of the set up needed to perform this experiment at the signal wavelength of 1310nm.

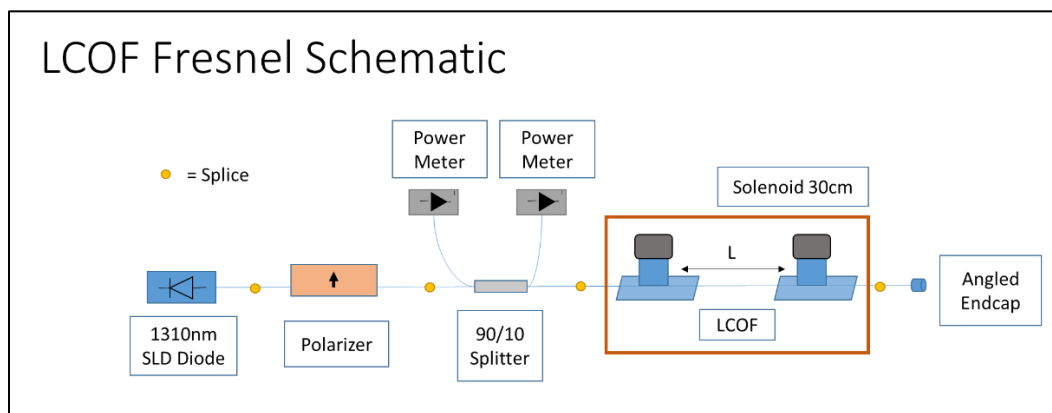


FIGURE 5.3 LCOF Fresnel reflection loss schematic

Verifying power after every component ensures high transmission to the endcap. A supply of refractive index oils will increase the accuracy of the index measurement. A

thermopile power meter and a low power detector, i.e. ILX, measures the power for the Fresnel total internal reflection parameters. Using the solenoid as a heat source enables measurement of the temperature dependence of the refractive index or guiding changes with temperature.

## **VI. Conclusion**

### **a. Significance of this work**

Focusing on a polarization maintaining isolator for the application of fiber systems, the goal of the experimentation was to demonstrate the foundation for a practical in-line fiber isolator. The main goals are Faraday rotation verification and proof of light rotation within a fiber chain. Although this just scratches the surface of the inline isolator capability, the experimentation verified the test set-ups and identified easy time saving solutions to allow for future completion of the isolator testing and further extensions of this work to devices such as circulators and modulators.

The problems with most fiber-based isolators is that they rely on construction consisting of an input waveguide coupled to potentially anti-reflection coated collimating optic and linear polarizer. The light then passes into the active Faraday crystal rotating the polarization the desired  $45^\circ$  and then out to a polarizer and coupler to send the light into the output fiber. Insertion losses as high as 3 dB and absorption of 0.0015/cm at 1064nm are measured in these devices, which reduce the efficiency of fiber lasers. [Northrup Grumman]. Minimizing losses within a fiber laser amplifier while maintaining low insertion loss is extremely beneficial to system performance. When multiple stages are used in laser amplification each stage needs an isolator to protect all the previous components from high back reflections or nonlinear effects which could cause damage.

An attractive solution for a low-loss and compact isolator is integrating a viscous ionic liquid solution with a medical grade hollow core fiber. Changing the active material from a bulky crystal to a small sub micro-liter liquid, stable over a wide range of temperatures with a favorable Verdet constant, the suspended ionic liquid achieves rotation over a shorter length and a smaller field than fused silica and has been demonstrated in photonic crystal fibers [Schmidt et al]. Less energy is therefore needed to create rotation within the ionic fluid minimizing the magnet required and thus total package size.

One other main reason for an in-line fiber isolator is low insertion loss, as this approach eliminates losses from free space optics, anti-reflection coatings, and coupling

into a bulky crystalline substrate. An in-line fiber solution also allows for easy linear polarizer integration through COTS fiber components and two additional low loss, <0.2dB splices. Another advantage to this approach is minimal heating due to the small liquid volumes thermal capacity. This all-fiber structure mixed with minimal heating may lead to in-line isolators that scale to much higher average power compared to commercially-available products.

The potential for an in-line fiber isolator is revolutionary in its tailorability for a variety of different applications. The two qualified set ups detailed in this paper explore how simple it is to test many material and optical properties from index to Faraday rotation and change over temperature. These experiments look to verify the performance of the test setups. One test setup proved to provide useful rotation results while the second needs some adjustments to help better identify rotation within an optical isolator. This can only be accomplished if more chain samples are created, hopefully in a more time efficient way.

With a robust process in synthesis of ionic liquids, there are a multitude of samples available for testing with applications over many wavelengths. With a few process refinements the potential for full material characterization has been shown in this paper. With a goal of a new family of in-line low loss isolators this paper has laid the frame work to accomplish the testing and verification.

## **b. Main results**

One key iron ionic material was run through all the aforementioned tests and provided useful process reformation and redlining information. Starting with material verification, which showed a propagation loss for [BMIM][FeCl<sub>4</sub>] of 0.0475dB/cm at 980nm, results also showed promise for transmission at 1310nm and 1550nm with propagation losses of 0.0315 dB/cm and 0.0471 dB/cm respectively.

The Faraday rotation testing yielded reasonable results for the fused silica baseline of  $0.1 \text{ rad}/m^{-1}T^{-1}$  at 975nm. The [BMIM][FeCl<sub>4</sub>] results required some post processing but demonstrated Faraday rotation exceeding the fused silica chamber by over double

over the rotation per magnetic field strength at  $0.04^\circ/\text{cm}$  at 600mT field. Low temperature results were not obtained but can easily be verified in future testing. High temperature results were promising in that they showed consistent rotation and minimal variation of  $0.007^\circ$  over the  $40^\circ\text{K}$  temperature range resulting in a temperature dependence of  $0.000175^\circ/\text{K}$ .

The results from the Faraday rotation tests indicate the length needed for the LCOF to achieve  $45^\circ$  of rotation would be on the order of 50.6 cm. For integration with a  $5\mu\text{m}$  hollow core fiber, the length needed to achieve  $45^\circ$ , results in a liquid volume of 40nL. With a fiber of this length, the total expected insertion loss from UV-VIS would be up to about 2.4dB. There would still be other losses to minimize from liquid integration, but requiring only a magnetic field of 500mT means a fiber-based solution could soon be available.

A key point that was not reached is verification of isolation within the ionic material. This property shows up in as amplitude variation in the Faraday rotation scans. However, since a full  $45^\circ$  rotation was not reached, no measurement of isolation was performed, although insertion loss was through the UV-Vis scan and verified in manufacturing through the LCOF test.

### **c. Lessons learned**

The Faraday rotation testing would not have been possible without a few key pieces of optical equipment. A critical component was the photo-elastic modulator, a compression-modulated device with manual force along one axis. This force changes the path length seen along one axis, creating a retardance between the two axes. By varying this force, the amount of path length change increases making the PEM a variable wave plate. Making sure the parameters of this modulator are set properly dramatically helps the polarization derivation of the test set up. The peak retardance also needs to be aligned with the optical setup so as to fully minimize the Bessel component for rotation extraction.

Taking the Jones matrix for the full system and operating on the incident electric field confirms the polarization analysis. This analysis applied to the raw data enables extraction of field intensity relating measured power received at the detector to polarization information.

The second key equipment piece belongs to the cryostation. Easily set up the cryostation can run a full low power test or magnetic field sweep in under a few hours. With the closed coolant loop, two coolant materials and extreme vacuum, the cryostation takes no time to reach operating environments and subsequently has minimal recharge time. Multiple samples can easily be tested in a span of a few days. The ease of testing a myriad of variables with magnetic field from +/- 700mT to sub cooled temperatures down to 2°K and up to 350°K and a range of pressures down to a full vacuum give much versatility to the testing.

The main issue with the Faraday rotation experiment was that the time put into sample cell creation was tedious and required time hand slicing and gluing the cells whereas purchasing of prefabricated cells would ensure liquid containment and operation at subcooled temperatures and vacuum pressures. This homemade cell affected vacuum pull time and the cryostation ability to perform the programmed tests.

Availability of a few different wavelengths setups including 980nm, 1310nm, and 1550nm would also ease testing and allow for a full range of materials and applications to be explored. For each wavelength, specific schematic components were needed including a seed, polarizer, 90/10 tap, retro reflector, and appropriately sized polarization paddles.

The advantage of using a solenoid is the generation of a controlled and uniform magnetic field source. This solenoid's applied field, verified with simple electromagnetic equations, produces a constant magnetic field along the length of the fiber sample.

The rotating polarizer is the next key piece, as without it, measuring the amount of rotation induced by the fiber would be a painstakingly long process by hand manually rotating a polarizer back and forth while recording power data. Synchronizing this up to the solenoid current applied, temperature, and detector voltage, LabVIEW output a file yielding all the data necessary to sweep the polarizer over a full 360°.

One issue in the LCOF process was the adjustability in the diagnostic path. This testing laid the experiential framework and identified some limitations that inhibited full verification of the Faraday material properties of the ionic liquid. From the beginning of the lab the power throughput through the fiber tended to be lower than expected. Transmission through the angle cleaved HI 1060 only reached 60% instead of the

expected 98% from pure absorption loss. The insertion loss expected by the in-situ testing reached 10dB explaining some of the loss to system coupling. This indicates other losses, issues coupling into the HI 1060 fiber, or a poor termination. A 3dB loss (or 50%) was reached after only a longitudinal integration of 13 cm of ionic liquid transverse a 0.4-micron core.

Splicing and packing the chains prior to filling with the ionic liquid proved time consuming from the fragility of the splice bond. Testing is currently limited by the number of chain samples available. Providing time and work into chain splice improvement will drastically expedite testing. Purchasing a few key splicing elements will improve yield of chains produced from the process and the time required to create each splice.

#### **d. Future work and closing remarks**

Splice optimization, resulting in a quicker chain creation will stock up the number of chains available for testing. Decreasing the timing required for LCOF testing, increasing yield and providing spares will greatly expedite testing. Additionally, this will solve the issue of manufacturing up front. The index for fused silica is the foundation for understanding how the change in index as a function of the change in wavelength can affect rotation. This would be the next key material property to measure whether by TIR or index matching oils. The next key material for exploration should be erbium because of its similar fabrication and excellent Faraday rotation properties. This liquid would be best to test at 1310nm. Expansion of the testing to a common wavelength will dictate substitution of the ionic base material.

The final take away is that liquids have multiple containment options and can be optimized for small volumes, and decreased insertion loss if coupled with a hollow core fiber reducing the volume and weight even further. This material proves ideal for a small active medium to create an in-line fiber isolator.

An in-line fiber, isolator is worth further investigation, as the promise of low insertion loss, bulky crystalline substrate elimination, easy linear polarizer integration, minimal package heating and size makes this solution attractive to the isolator industry.

With goals from low loss integration in telecommunications to power scaling applications in the laser field, there are a vast array of uses and demand for a new isolator system, as well as associated magneto-optic devices such as circulators and modulators.

## References

- Page 6 [Villora] Villora, Encarnación G., Pablo Molina, Masaru Nakamura, Kiyoshi Shimamura, Tsubasa Hatanaka, Akiharu Funaki, and Kunihiro Naoe. "Faraday Rotator Properties of  $\{\text{Tb}_3\}[\text{Sc}_{1.95}\text{Lu}_{0.05}](\text{Al}_3)\text{O}_{12}$ , a Highly Transparent Terbium-garnet for Visible-infrared Optical Isolators." *Appl. Phys. Lett. Applied Physics Letters* 99.1 (2011): 011111. Web.
- Page 6, 25-77 [Hecht] Hecht, Eugene. *Optics*. Harlow: Pearson Education Limited, 2008. Print.
- Page 9. [Endoscope]. Seibel, Eric J., Quinn Y. J. Smithwick, Chris M. Brown, and Per G. Reinhall. "Single-fiber Flexible Endoscope: General Design for Small Size, High Resolution, and Wide Field of View." *Biomonitoring and Endoscopy Technologies* (2001): n. pag. Web.
- Page 9, 72 [Photonics] Saleh, Bahaa E. A., and Malvin Carl. Teich. *Fundamentals of Photonics*. 2nd ed. Hoboken: Wiley, 2007. Print.
- Page 12-14 "Fiber Optic Fusion Splicers and How They Work." *Fiber Optic Fusion Splicers and How They Work*. Learning Center Web. 25 Nov. 2015.
- Page 12 [Fiber Guide] "Optical Fibers -." *Fiberguide*. N.p., n.d. Web. 12 June 2016. <http://www.fiberguide.com/products/optical-fibers/>
- Page 12 [Corning SMF 28] Corning SMF-28 ULL Optical Fiber Product Information." . Corning, 2011. Web. 25 Nov 2011. <https://www.corning.com/media/worldwide/coc/documents/Fiber/SMF-28%20ULL.pdf><<http://www.corning.com/WorkArea/showcontent.aspx?id=41243>>.
- Page 12 [Molex] "Polymicro Technologies™ Capillary Tubing." - Molex. N.p., n.d. Web. 13 March 2016. [http://www.molex.com/molex/products/family?key=polymicro\\_capillary\\_tubing&channel=products&chanName=family&pageTitle=Introduction&parentKey=polymicro#](http://www.molex.com/molex/products/family?key=polymicro_capillary_tubing&channel=products&chanName=family&pageTitle=Introduction&parentKey=polymicro#)
- Page 13 [Nufern] "Optical Fiber, Coil Winding, Lasers and Amplifiers." *PM980-XP*. N.p., n.d. Web. 13 March 2016. [http://www.nufern.com/pam/optical\\_fibers/964/PM980-XP/](http://www.nufern.com/pam/optical_fibers/964/PM980-XP/)
- Page 13 [Corning HI1060] "Corning ® HI 1060 & RC HI 1060 Specialty Optical Fibers." *Corning ®*. N.p., n.d. Web. 13 Mar. 2016. <https://www.corning.com/media/worldwide/csm/documents/HI%201060%20Specialty%20Fiber%20PDF.pdf>
- Page 14 [Hamaguchi] Hamaguchi, H. "Discovery of a New Magnetic Fluid: Bmim[FeCl<sub>4</sub>] Ionic Liquid." *INTERMAG Asia 2005. Digests of the IEEE International Magnetics Conference, 2005*. (2005). Web. 27 Sept. 2015.
- Page 14 [Hayashi] Hayashi, S., S. Saha, and H. Hamaguchi. "A New Class of Magnetic Fluids: Bmim[FeCl<sub>4</sub>] and Nbmim[FeCl<sub>4</sub>] Ionic Liquids." *IEEE Trans. Magn. IEEE Transactions on Magnetics* 42.1 (2006): 12-14. Web.
- Page 14-15, 80 [Schmidt et all] Schmidt, Markus A., Lothar Wondraczek, Ho W. Lee, Nicolai Granzow, Ning Da, and Philip St. J. Russell. "Complex Faraday Rotation in Microstructured Magneto-optical Fiber Waveguides." *Adv. Mater. Advanced Materials* 23.22-23 (2011): 2681-688. Web.

Page 18-20 [R.H. Gargstang]. Garstang, R. H. "Energy Levels and Transition Probabilities of Fe IV." *Monthly Notices of the Royal Astronomical Society* 118.6 (1958): 572-84. Web.

Page 20 [W.T. Carnall] Carnall, W. T. "Electronic Energy Levels in the Trivalent Lanthanide Aquo Ions. I. Pr<sub>3</sub>, Nd<sub>3</sub>, Pm<sub>3</sub>, Sm<sub>3</sub>, Dy<sub>3</sub>, Ho<sub>3</sub>, Er<sub>3</sub>, and Tm<sub>3</sub>." *The Journal of Chemical Physics* J. Chem. Phys. 49.10 (1968): 4424. Web.

Page 21, 34 [Nirvana] "Nirvana™ Auto-Balanced Photoreceivers." *Nirvana Auto-Balanced Photoreceivers*. Newport, n.d. Web. 23 July 2016.

Page 23 [Shurcliff] Shurcliff, William A. *Polarized Light: Production and Use*. Cambridge: Harvard UP, 1962. Print.

Page 24 [Gram] Gram matrix. *Encyclopedia of Mathematics*. URL:

[http://www.encyclopediaofmath.org/index.php?title=Gram\\_matrix&oldid=35177](http://www.encyclopediaofmath.org/index.php?title=Gram_matrix&oldid=35177)

Page 26 [Optical Resonators] Hodgson, Norman, and Horst Weber. *Optical Resonators: Fundamentals, Advanced Concepts, and Applications*. London: Springer, 1997. Print.

Page 27-33 Matrix math help: Anton, Howard, and Chris Rorres. *Elementary Linear Algebra*. 6th ed. New York: John Wiley, 1994. Print. Applications Version.

Page 32 Gradtejn, I. S., I. M. Ryik, and Alan Jeffrey. *Table of Integrals, Series, and Products*. New York, Academic Press: Elsevier, 1980. *Science Direct*. Web. Page 974

Page 33 [HINDS] Kemp, J. C. "Polarized Light and Its Interaction with Modulating Devices -a Methodology Review-." *HINDS Instruments* (1987): n. pag. *Technology for Polarization Measurement*. HINDS International Inc. Web.

Page 36 [980Polarizer] "Thorlabs - ILP980PM-FC In-Line Fiber Polarizer, 980 ± 10 Nm, PM/PM Pigtail, FC/PC." *Thorlabs - ILP980PM-FC In-Line Fiber Polarizer, 980 ± 10 Nm, PM/PM Pigtail, FC/PC*. ThorLabs, n.d. Web. 04 Sept. 2015.

Page 37 [LCOF Detector] "Silicon Photoreceiver, 300-1050 Nm, 200 KHz, Free Space, M4." *Newport Corporation*. N.p., n.d. Web. 04 Sept. 2015.

Page 38 [Newport Rotation] "Compact Rotation Stage, 360°, DC Servo Motor, PR Series." *PR50CC*. Newport, n.d. Web. 04 Sept. 2015. <https://www.newport.com/p/PR50CC>

Page 39 [Serway] Serway, Raymond A., and John W. Jewett. *Physics for Scientists and Engineers*. Belmont, CA: Thomson-Brooks/Cole, 2008. Print. Page849

Page 43, 51 [Norland 81] "Norland Optical Adhesive 81." *NOA81*. Norland Products, n.d. Web. 04 Sept. 2015. <https://www.norlandprod.com/adhesives/noa%2081.html>

Page 43 [New Era] "NE-1000 ProgrammableSingle Syringe Pump." *Syringe Pump*. New Era, n.d. Web. 04 Sept. 2015. <http://www.syringepump.com/NE-1000.php>

Page 72-73 [Griffiths] Griffiths, David J. *Introduction to Quantum Mechanics*. Upper Saddle River, NJ: Pearson Prentice Hall, 2005. Print.

Page 74 [Synthesis materials] Xu, Wei, Deqing Zhang, Chunhe Yang, Xianglin Jin, Yongfang Li, and Daoben Zhu. "Synthesis, Crystal Structure and Electrical Conductivity of [bmim][Ni(dmit)<sub>2</sub>]<sub>3</sub> (bmim = 1-butyl-3-methylimidazolium, Dmit = 1,3-dithiol-2-thione-4,5-dithiolate)." *Synthetic Metals* 122.2 (2001): 409-12. *Science Direct*. Web. 04 Sept. 2015. <http://www.sciencedirect.com/science/article/pii/S0379677900004057>

Page 74 Brown, Richard J. C., Thomas Welton, Paul J. Dyson, and David J. Ellis. "1-Butyl-3-methylimidazolium Cobalt Tetracarbonyl [bmim][Co(CO)<sub>4</sub>]: A Catalytically Active Organometallic Ionic Liquid." *Chemical Communications Chem. Commun.* 18

(2001): 1862-863. *Google Scholar*. Web.

<http://pubs.rsc.org/en/Content/ArticleLanding/2001/CC/b104601m#!divAbstract>

Page 76 [ILP1310PM] "Thorlabs - ILP1310PM-FC In-Line Fiber Polarizer, 1310  $\pm$  50 Nm, PM/PM Pigtail, FC/PC." *ILP1310PM-FC In-Line Fiber Polarizer, 1310  $\pm$  50 Nm, PM/PM Pigtail, FC/PC*. Thorlabs, n.d. Web. 04 Sept. 2015.

<http://www.thorlabs.us/thorproduct.cfm?partnumber=ILP1310PM-FC>

Page 76 [1310 Diode] "Thorlabs - FPL1053S 1310 Nm, 130 MW, Butterfly Laser Diode, SM Fiber, FC/APC." *FPL1053S 1310 Nm, 130 MW, Butterfly Laser Diode, SM Fiber, FC/APC*. Thorlabs, n.d. Web. 04 Sept. 2015.

Page 80 [Northrup Grumman] "TGG (Terbium Gallium Garnet)." *Northrop Grumman*. N.p., n.d. Web. 05 Sept. 2015.

<http://www.northropgrumman.com/BusinessVentures/SYNOPTICS/Products/SpecialtyCrystals/pages/TGG.aspx>